Refractory High-Entropy Alloys: Design, Fabrication, Characterization, and Nanoparticle Synthesis

A Thesis Presented for the
Master of Science
Degree
The University of Tennessee, Knoxville

John Hutson Whitlow
August 2023

Copyright © 2023 by John Hutson Whitlow
All rights reserved.

Dedication

I dedicate this publication to my wife, Kayleigh, and all the support I have received from our friends and family. Forever and Always, Sweetheart.

To God be the Glory.

Now concerning brotherly love, you have no need for anyone to write to you, for you yourselves have been taught by God to love one another, for that indeed is what you are doing to all the brothers throughout Macedonia. But we urge you, brothers, to do this more and more, and to aspire to live quietly, and to mind your own affairs, and to work with your hands, as we instructed you, so that you may walk properly before outsiders and be dependent on no one.

1 Thessalonians 4:9-12

Acknowledgements

I would like to acknowledge the help of the MSE department faculty and our team at UTK. Thank you to Doug Fielden for his continued work on equipment within our lab, as well as preparation of samples. Your expertise in machining is unmatched. A special thank you to Lia Amalia, my partner throughout my studies at UTK. Thank you to Dr. Zongyong Lyu and soon-to-be Dr. Xuesong Fan for being so patient in teaching me your tips and tricks in the labs. Thank you to Dr. Eric Lass for his expertise on the design of RHEAs, and for his support in their testing. Thank you to Dr. Hu Anming and David Feiser from the mechanical engineering department for your continued research into HEA and RHEA nanoparticles. Thank you for the warm welcome Hugh Shortt and thank you for the opportunity and continued support you have given me, Dr. Peter K. Liaw.

Abstract

High-Entropy Alloys have been a highly researched area of metals ever since their introduction in 2004 by Brian Cantor and Jien-Weh Yeh. In the continued research of High-Entropy Alloys (HEAs), a specific area concerning Refractory High-Entropy Alloys (RHEAs) has emerged for their high-temperature applications. Although RHEAs have maintained high strength and toughness at high temperatures, their low ductility still needs to be addressed. A dataset was created to find correlations between various characteristics of RHEAs and their composition. A set of seven compositions were selected and fabricated. Mechanical tests were run on the seven compositions, and a proposal was written for neutron diffraction tests at Oak Ridge National Lab. *In-situ* neutron diffraction was performed during mechanical testing on the seven compositions. X-ray diffraction was performed on as-cast samples and post-mortem samples of each composition. The microstructural analysis led to one out of the seven RHEAs being confirmed to contain Transformation Induced Plasticity (TRIP). The six remaining RHEAs were confirmed as a single-phase BCC. Nanoparticles were fabricated from three of the confirmed single-phase compositions and characterized using X-ray diffraction and Scanning Electron Microscope (SEM) Imaging. All three were found to be a single-phase FCC nanoparticle.

TABLE OF CONTENTS

CHAPTER ONE Introduction to High-Entropy Alloys 1
Introduction to the Thesis 2
Background 2
Properties 3
Refractory HEAs 4
CHAPTER TWO RHEA Dataset 6
Introduction 7
Disclosure 7
Reasoning for a RHEA Dataset 7
Microstructure and Properties 12
Density 12
D-Parameter 12
Valence Electron Count 12
Phase 13
Atomic-Size Mismatch 13
Configurational Entropy 14
Processing and Composition 14
Dataset Categories and Compilations 15
Reasoning for use of Specific Yield Strength 15
Overall Compilation 15
D-Parameter 15
Specific Yield Strength versus Atomic-Size Mismatch 21
Percent Plasticity versus Atomic-Size Mismatch 21
Atomic Size Mismatch versus D-Parameter 21
Specific Yield Strength versus Entropy of Mixing 31
Entropy of Mixing versus D-parameter 31
As-Cast, Annealed, and HIP Comparison 31
Aluminum Addition versus Specific Yield Strength 42
Silicon Addition versus Specific Yield Strength 42
Comparison of the Number of Components 42
Conclusion of RHEA Dataset 50
CHAPTER THREE RHEA Mechanical Testing 51

Introduction 52
Selection of RHEA compositions 52
Weighing of Elemental Compositions for Fabrication 53
Arc-Melting 53
Arc-Melting Standard Operating Procedures 54
Introduction 54
"Old" Arc-Melter Startup 54
"Old" Arc-Melter Shutdown 61
"New" Arc-Melter Startup 71
"New" Arc-Melter Shutdown 83
Compression Samples 94
Tension Samples 94
Difficulty in Casting and Fabrication 94
Compression Testing 97
Tension Testing 97
Results and Discussion 97
Conclusion 101
CHAPTER FOUR X-Ray Diffraction Results 102
Disclosure 103
Introduction 103
HfNbTiZr 103
HfNbTaTiZr 103
$HfTa_{0.5}TiZr$ 109
$HfNb_{0.5}Ta_{0.5}TiZr$ 109
$HfNbTa_{0.5}TiZr$ 109
$Hf_{0.5}NbTa_{0.5}TiZr$ 109
$NbTa_{0.5}TiZr$ 109
Conclusion 119
CHAPTER FIVE Proposal for Neutron Diffraction and Preliminary Results 120
Novelty of Research 121
Disclosure 121
Scientific Importance 121
Preliminary Work 122
Choice of Instrument 125

Data Analysis and Scientific Outcomes 126
Safety Considerations 126
Introduction to Preliminary Results 126
Work Hardening 127
D-Spacing and Lattice-Strain Measurements 127
HfNbTiZr 127
HfNbTaTiZr 127
$HfTa_{0.5}TiZr$ 127
$HfNb_{0.5}Ta_{0.5}TiZr$ 132
$HfNbTa_{0.5}TiZr$ 132
$Hf_{0.5}NbTa_{0.5}TiZr$ 132
$NbTa_{0.5}TiZr$ 132
Elastic Modulus 137
Kroner Bulk Modulus and Cauchy Pressure 137
Conclusion 137
Future Directions 142
CHAPTER SIX RHEA Nanoparticles 143
Disclosure 144
Introduction 144
RHEA Nanoparticle Results 145
$HfNb_{0.5}Ta_{0.5}TiZr$ 145
$HfNbTa_{0.5}TiZr$ 145
$Hf_{0.5}NbTa_{0.5}TiZr$ 145
Discussion 155
Conclusion 155
CHAPTER SEVEN Conclusions and Future Directions 156
Conclusions 157
RHEA Dataset 157
RHEA Fabrication, Mechanical Testing, and XRD Results 157
RHEA Neutron Diffraction Results 157
RHEA Nanoparticles 159
Future Directions 159
RHEA Dataset 159
RHEA Fabrication and Mechanical Testing 159

RHEA Nanoparticles 160
REFERENCES 161
VITA 169

List of Tables

Table 1: RHEA Dataset with Specific Yield Strength and Processing 8
Table 2: Specific Yield Strength versus D-Parameter 16
Table 3: Specific Yield Strength versus Atomic Size Mismatch 22
Table 4: Atomic Size Mismatch versus D-Parameter 28
Table 5: Specific Yield Strength versus Entropy of Mixing (ΔS_{mix}) 32
Table 6: Entropy of Mixing (ΔS_{mix}) versus D-Parameter 37
Table 7: Statistics on Specific Yield Strength of As-Cast RHEAs 40
Table 8: Statistics on Specific Yield Strength of Annealed RHEAs 40
Table 9: Statistics on Specific Yield Strength of HIP RHEAs 40
Table 10: Specific Yield Strength with Percent Al Addition 43
Table 11: Specific Yield Strength with Percent Si Addition 46
Table 12: Statistics on Specific Yield Strength of Four Component RHEAs 48
Table 13: Statistics on Specific Yield Strength of Five Component RHEAs 48
Table 14: Statistics on Specific Yield Strength of Six Component RHEAs 48
Table 15: Properties and Yield of Reported RHEAs 98
Table 16: Compression Elastic Modulus Values 138
Table 17: Tension Elastic Modulus Values 139
Table 18: Calculated Single Crystal Elastic Constants 140
Table 19: Strength, Ductility, and Plasticity Values 141

List of Figures

Figure 1: D-Parameter Comparison of Mo and Ta Containing RHEAs 18
Figure 2: D-Parameter Comparison of V and Zr Containing RHEAs 19
Figure 3: D-Parameter versus Percent Plasticity 20
Figure 4: Atomic Size Mismatch of Studied RHEAs 26
Figure 5: Atomic-Size Mismatch versus Percent Plasticity 27
Figure 6: Atomic-Size Mismatch versus D-Parameter 30
Figure 7: Entropy of Mixing (ΔS_{mix}) Comparison 36
Figure 8: Entropy of Mixing (ΔS_{mix}) versus D-Parameter 39
Figure 9: Chart Comparison of Processing of RHEAs 41
Figure 10: Al Addition [%] versus Specific Yield Strength 45
Figure 11: Si Addition [%] versus Specific Yield Strength 47
Figure 12: The Comparison of the Number of Components for RHEAs 49
Figure 13: Argon Tanks 55
Figure 14: Furnace Breaker 56
Figure 15: Water Valves 57
Figure 16: Pressure Dial 58
Figure 17: Copper Mold 59
Figure 18: Casting Setup 60
Figure 19: Mechanical Vacuum Switch 62
Figure 20: Valve Switches 63
Figure 21: Varian Dial 64
Figure 22: Pressure Display 65
Figure 23: Argon Valve 66
Figure 24: Auxiliary Power Switch 67
Figure 25: Lamp Switch 68
Figure 26: Amperage Dial 69
Figure 27: Oxidized Titanium 70
Figure 28: Chamber Valve 72
Figure 29: Chamber Lift 73

Figure 30: Mold or Crucible Lift Handle 74
Figure 31: Rotary Vane Pump Switch 75
Figure 32: Vacuum Valve 76
Figure 33: Casting Vacuum Valve 77
Figure 34: Casting Vacuum Valve 2 78
Figure 35: Main Switch 79
Figure 36: Diffusion Pump Switch 80
Figure 37: “New” Arc-melter Breaker 81
Figure 38: Water Valves for Filtration 82
Figure 39: Water Valves 84
Figure 40: Argon Tank 85
Figure 41: Diffusion Pump Valve 86
Figure 42: Turbo-Pump Button 87
Figure 43: Argon Valve 88
Figure 44: Auxiliary Power Switch 89
Figure 45: Generator Knob 90
Figure 46: Reset Button 91
Figure 47: Tungsten Electrode 92
Figure 48: Arc Shield 93
Figure 49: Compression Rod 95
Figure 50: Tension Plate 96
Figure 51: Compression Stress-Strain Curve 99
Figure 52: Tension Stress-Strain Curve 100
Figure 53: As-Cast HfNbTiZr XRD 104
Figure 54: Post-Mortem HfNbTiZr XRD 105
Figure 55: As-Cast HfNbTaTiZr XRD 106
Figure 56: Post-Mortem HfNbTaTiZr XRD 107
Figure 57: As-Cast $HfTa_{0.5}TiZr$ XRD 108
Figure 58: Post-Mortem $HfTa_{0.5}TiZr$ XRD 110
Figure 59: As-Cast $HfNb_{0.5}Ta_{0.5}TiZr$ XRD 111

Figure 60: Post-Mortem $HfNb_{0.5}Ta_{0.5}TiZr$ XRD 112
Figure 61: As-Cast $HfNbTa_{0.5}TiZr$ XRD 113
Figure 62: Post-Mortem $HfNbTa_{0.5}TiZr$ XRD 114
Figure 63: As-Cast $Hf_{0.5}NbTa_{0.5}TiZr$ XRD 115
Figure 64: Post-Mortem $Hf_{0.5}NbTa_{0.5}TiZr$ XRD 116
Figure 65: As-Cast $NbTa_{0.5}TiZr$ XRD 117
Figure 66: Post-Mortem $NbTa_{0.5}TiZr$ XRD 118
Figure 67: Stress-Strain Diagram 123
Figure 68: Deformation Mechanisms Illustration 124
Figure 69: Work Hardening of Successful Tension Tests 128
Figure 70: D-Spacing and Lattice Strain of HfNbTiZr 129
Figure 71: D-Spacing and Lattice Strain for HfNbTaTiZr 130
Figure 72: D-Spacing and Lattice Strain of $HfTa_{0.5}TiZr$ 131
Figure 73: D-Spacing and Lattice Strain of $HfNb_{0.5}Ta_{0.5}TiZr$ 133
Figure 74: D-Spacing and Lattice Strain of $HfNbTa_{0.5}TiZr$ 134
Figure 75: D-Spacing and Lattice Strain of $Hf_{0.5}NbTa_{0.5}TiZr$ 135
Figure 76: D-Spacing and Lattice Strain of $NbTa_{0.5}TiZr$ 136
Figure 77: Nanoparticle $HfNb_{0.5}Ta_{0.5}TiZr$ XRD 146
Figure 78: $HfNb_{0.5}Ta_{0.5}TiZr$ Phase Confirmation 147
Figure 79: Nanoparticle $HfNbTa_{0.5}TiZr$ XRD 148
Figure 80: $HfNbTa_{0.5}TiZr$ Phase Confirmation 149
Figure 81: Nanoparticle $Hf_{0.5}NbTa_{0.5}TiZr$ XRD 150
Figure 82: $Hf_{0.5}NbTa_{0.5}TiZr$ Phase Confirmation 151
Figure 83: $Hf_{0.5}NbTa_{0.5}TiZr$ Nanoparticles Comparison 152
Figure 84: $Hf_{0.5}NbTa_{0.5}TiZr$ Nanoparticle Fabricated in Water 153
Figure 85: $Hf_{0.5}NbTa_{0.5}TiZr$ Nanoparticle Fabricated in Toluene 154
Figure 86: Common Material Comparison 158

CHAPTER ONE
Introduction to High-Entropy Alloys

Introduction to the Thesis

This thesis is a representation of the work and research conducted at the University of Tennessee Knoxville on Refractory High Entropy Alloys (RHEAs) by John Whitlow. Chapter One is an introduction the topic as well as a discussion on the reasons for this research area. Chapter Two is a discussion of a dataset created by John Whitlow and Lia Amalia to strengthen the design and selection of alloys studied. Chapter Three is on the mechanical testing of RHEAs, and includes the selection and design conducted by Dr. Eric Lass, fabrication, and mechanical testing of the alloys studied. Chapter Four discusses the X-Ray Diffraction (XRD) patterns obtained by Dr. Eric Lass and Melanie Moczadlo on the set of RHEAs. Chapter Five discusses the proposal written after the completion of compression testing for *in-situ* Neutron Diffraction at Oak Ridge National Lab (ORNL), and the preliminary results are reported from the received beamtime. Chapter Six contains an introduction to RHEA nanoparticles and the novelty of the research, as well as some results from the nanoparticles fabricated by Dr. Anming Hu and David Fieser. Chapter Seven concludes the thesis with overall conclusions and future directions for the topics presented.

Background

Alloying has been used for many years to improve the qualities of everyday items. Most commonly thought of are steel and aluminum alloys, but there are many others that have since been studied for their mechanical properties. The research on alloying eventually led to the research on multicomponent alloys. Typically, an alloy consists of multiple elements with one being considered the primary component, or solvent, and the others being an additive, or solute, to improve the overall properties of the alloy. The Gibbs Phase Rule dictates that the number of elements in the alloy should be kept as low as possible to prevent the formation of intermetallic compounds that cause deterioration in the alloy [1]. This rule is oftentimes used and generally defined as the number of equilibrium phases, p, is greater than the number of components, c, plus one, or $p > c + 1$.

In 2004, Cantor and Yeh published their work on multicomponent alloys that went against the normal definition of an alloy. Cantor originally began his work in 1981 and published his findings on his samples in 2004. He fabricated alloys with 16 and 20 elements in equimolar amounts and explored the central region of the multi-component alloy phase diagram instead of

apexes or edges in of the phase diagram. In his conclusion, he states that the number of phases for the multicomponent alloys was always below the maximum number of phases allowed using Gibbs Phase Rule [2].

In the same year, Yeh published his work on multi-principal-element alloys. He was the first to explain the concept of High-Entropy Alloys (HEAs) and began his work with the belief that the multiple elements would create a high mixing entropy that would lead to better mixing. In his work, the multi-principal-element alloys showed great wear resistance and oxidation resistance, leading to a further interest in these alloys [1, 3].

Properties

The design of HEAs is very different from that of traditional alloys. For instance, an HEA contains at least 5 elements, which are equimolar or near equimolar [5 – 35 atomic percent (at. %)] [1]. Because of the multiple elements present, HEAs are known to exhibit the four core effects: a high mixing entropy (ΔS), severe lattice distortion, sluggish diffusion, and cocktail effect [1, 4].

The high ΔS arises from the correlation between the mixture enthalpy and entropy according to Gibbs Free Energy theory. At higher temperatures, the mixing entropy plays a large role in reducing the Gibbs Free Energy and in short produces a simple solid-state solution [4].

The largely equimolar amount of elements in HEAs allows each element to be considered both a solvent and a solute, meaning that each element has a likelihood to occupy the same site which results in severe lattice distortion [1]. The multiple elements also introduce many different atomic sizes, bond lengths, and lattice energies adding to the degree of lattice distortion. This distortion is correlated to chemical bonding and electron density among the elements, changing key physical and mechanical properties of HEAs [5].

The lattice structures of elements occupying different sites cause a fluctuation in the diffusion path for an element or a vacancy to migrate, resulting in a higher activation energy and sluggish diffusion rate [6]. The packing density, because of the many elements, also causes a lower diffusion rate. A lower growth and nucleation can yield amorphous phases during solidification and the formation of ultrafine crystallites [5, 7].

It should also be noted that HEAs are regarded as atomic-scale composites, and because they are multicomponent, their interactions on the micro-scale create the multi-component

composite effect, also known as the ‘cocktail effect’ [1]. The cocktail effect, in short, is a combination of the three previous core effects, and is often used for the design of HEAs [5].

With the continued research on HEAs, theoretical phase diagram calculations have been created and are commonly used for design. One of the most common is CALculation of PHAse Diagrams (CALPHAD) through Thermo-Calc. The abilities of CALPHAD are explained further in the design chapter. From Cantor’s original publication in 2004, manufacturing HEAs have expanded beyond casting and melt spinning, with most traditional methods in fabricating alloys being used [6]. One of the most common methods for the fabrication and casting of HEAs is Arc-melting, which allows for the components to be mixed and cast in the presence of an inert gas to prevent oxidation.

After fabrication, samples are either subjected to characterization or mechanical testing. Much of the use of HEAs is seen in high-temperature applications, especially for Refractory HEAs (RHEAs) [8]. The elastic and plastic deformation range can be explored by tension and compression testing of RHEA samples, which can then be applied back into the design process using Machine Learning (ML). Post-mortem samples are commonly characterized to further understand the activated mechanisms during the deformation process. *In-Situ* Neutron Diffraction allows for the study of real-time deformation micro-mechanisms such as Transformation Induced Plasticity (TRIP) and/or twinning deformation.

Refractory HEAs

RHEAs are a subsection within HEAs designated for the multicomponent system with Refractory elements, such as niobium, molybdenum, tantalum, and tungsten. The benefit to RHEAs is their ability for high temperature applications while retaining their great strength. The issue lies within the lack of ductility for RHEAs, limiting their ability for applications, as well as a difficulty in fabrication.

RHEAs have recently been studied for their applications at high temperatures and have great room temperature strength as well. Although there are many benefits of RHEAs, the fabrication and machining process is very difficult, limiting their possible uses. This difficulty of machining and processing RHEAs is from their lack of ductility, and while some processes have been used to refine their ductility, little progress has been made in a solution to this issue.

Our hypothesis is that there are multiple compositions that will accomplish the desired qualities for strength, ductility, and fatigue resistance to be applied in high-temperature applications. Our overall objectives are to provide a fundamental study to design and discover at least 4 compositions for ductile, high-strength RHEAs, then fabricate and investigate the compositions designed to fundamentally understand their mechanical behavior and analyze their possible use in the industrial field.

CHAPTER TWO

RHEA Dataset

Introduction

To begin the research of RHEAs, a dataset to draw correlations in the design of likely compositions can be very beneficial. This chapter discusses the data comparisons of the created dataset for RHEAs. This dataset can be transferred into possible ML applications or be used to draw more accurate conclusions on certain RHEA characteristics. All citations for each composition are shown in the overall dataset, Table 1.

Disclosure

Parts of Chapter 1 combined with the following chapter will be submitted for publication with the authors of the paper expected to be John Whitlow, Lia Amalia, and Peter K. Liaw. The chapter as it is in this thesis is the original work of John Whitlow. Further edits may be made to the chapter as it is seen here, prior to the publication of the journal article. The entirety of the dataset is not presented in this thesis due to size limitations, but it is planned to be an open source file published alongside the publication of this chapter.

Reasoning for a RHEA Dataset

Microstructure, processing, and compositions have all been tuned to enhance ductility, and to analyze the trends seen from these changes, a dataset has been made. Within this dataset different microstructural properties, namely the ratio of surface energy and unstable stacking fault energy (D-parameter), Valence Electron Count (VEC), Phases, Atomic Size Mismatch (δ), and Configurational Energy (ΔS_{mix}), will be analyzed to find correlations of parameters controlling the ductility of RHEAs.

The different processes used in fabricating the RHEA samples will be compared to establish standard processes for producing the desired qualities of RHEAs. These comparisons will be of as-cast, annealed (with comparisons of different annealing temperatures), and Hot Isostatic Pressed (HIP) processes.

Table 1: RHEA Dataset with Specific Yield Strength and Processing

Composition	Specific Yield Strength (RT) [MPa/(g/cm^3)]	Processing	Reference
$Al_{0.25}HfNbTiZr$	46.085	As-Cast	[16]
$Al_{0.50}HfNbTiZr$	84.626	As-Cast	[16]
$Al_{0.75}HfNbTiZr$	102.124	As-Cast	[16]
$Al_{0.25}MoNbTiV$	158.088	As-Cast	[43]
$Al_{0.25}NbTaTiV$	115.894	As-Cast	[44]
$Al_{0.2}MoTaTiV$	85.690	As-Cast	[45]
$Al_{0.3}HfNbTaTiZr$	101.512	As-Cast	[46]
$Al_{0.3}NbTa_{0.8}Ti_{1.4}V_{0.2}Zr_{1.3}$	198.786	HIP+annealed	[47]
$Al_{0.3}NbTaTi_{1.4}Zr_{1.3}$	187.303	HIP+annealed	[47]
$Al_{0.4}Hf_{0.6}NbTaTiZr$	160.913	Heat Treatment	[48]
$Al_{0.4}Hf_{0.6}NbTaTiZr$	160.913	HIP+annealed	[47]
$Al_{0.5}CrNbTi_2V_{0.5}$	208.885	annealed	[49]
$Al_{0.5}CrNbTi_2V_{0.5}$	193.297	As-Cast	[49]
$Al_{0.5}HfNbTaTiZr$	112.019	As-Cast	[46]
$Al_{0.5}MoNbTiV$	208.601	As-Cast	[43]
$Al_{0.5}NbTa_{0.8}Ti_{1.5}V_{0.2}Zr$	204.502	HIP+annealed	[47]
$Al_{0.5}NbTaTiV$	89.376	As-Cast	[44]
$Al_{0.6}MoTaTiV$	82.497	As-Cast	[45]
$Al_{0.75}HfNbTaTiZr$	122.787	As-Cast	[16]
$Al_{0.75}MoNbTiV$	164.105	As-Cast	[43]
$Al_{1.5}MoNbTiV$	67.833	As-Cast	[43]
$AlCr_{0.5}NbTiV$	200.958	As-Cast	[50]
$AlCr_{1.5}NbTiV$	253.883	As-Cast	[50]
AlCrMoNbTi	-	annealed	[51]
AlCrNbTiV	237.076	As-Cast	[50]
AlHfNbTaTiZr	130.283	As-Cast	[46]
AlHfNbTiZr	134.319	As-Cast	[16]
$AlMo_{0.5}NbTa_{0.5}TiZr$	216.169	Heat Treatment	[48]
$AlMo_{0.5}NbTa_{0.5}TiZr$	216.169	HIP+annealed	[47]
$AlMo_{0.5}NbTa_{0.5}TiZr$	216.169	HIP+annealed	[52]
AlMoNbTi	-	annealed	[53]
AlMoNbTiV	181.614	As-Cast	[43]
$AlNb_{1.5}Ta_{0.5}Ti_{1.5}Zr_{0.5}$	141.125	HIP+annealed	[47]

Table 1 Continued

Composition	Specific Yield Strength (RT) [MPa/(g/cm^3)]	Processing	Reference
AlNbTaTi	97.949	As-Cast	[54]
AlNbTaTiV	87.684	As-Cast	[44]
AlNbTiV	156.667	As-Cast	[50]
AlNbTiVZr	233.608	annealed	[55]
$AlNbTiVZr_{0.1}$	201.910	annealed	[55]
$AlNbTiVZr_{0.25}$	212.500	annealed	[55]
$AlNbTiVZr_{0.5}$	231.850	annealed	[55]
$AlNbTiVZr_{1.5}$	238.613	annealed	[55]
$C_{0.1}Hf_{0.5}Mo_{0.5}NbTiZr$	133.206	As-cast	[56]
$C_{0.3}Hf_{0.5}Mo_{0.5}NbTiZr$	135.890	As-cast	[56]
CoCrMoNb	158.783	As-cast	[57]
CoCrMoNbTi	131.661	As-cast	[57]
$CoCrMoNbTi_{0.2}$	216.330	As-cast	[57]
$CoCrMoNbTi_{0.4}$	204.103	As-cast	[57]
$CoCrMoNbTi_{0.5}$	186.767	As-cast	[57]
CrHfNbTiZr	141.007	annealed	[58]
$CrMo_{0.5}NbTa_{0.5}TiZr$	169.321	HIP	[59]
CrMoNbTi	198.515	Heat Treatment	[54]
CrMoTaTi	147.421	Heat Treatment	[54]
CrNbTiVZr	189.766	HIP	[60]
CrNbTiZr	180.749	HIP	[60]
$CrTaTi_{0.04}VW$	131.838	sintered	[61]
$CrTaTi_{0.07}VW$	133.169	sintered	[61]
CrTaVW	144.584	sintered	[61]
$Hf_{0.5}Mo_{0.5}NbSi_{0.1}TiZr$	152.491	As-cast	[62]
$Hf_{0.5}Mo_{0.5}NbSi_{0.3}TiZr$	156.464	As-cast	[62]
$Hf_{0.5}Mo_{0.5}NbSi_{0.5}TiZr$	184.715	As-cast	[62]
$Hf_{0.5}Mo_{0.5}NbSi_{0.7}TiZr$	180.863	As-cast	[62]
$Hf_{0.5}Mo_{0.5}NbSi_{0.9}TiZr$	194.553	As-cast	[62]
$Hf_{0.5}Mo_{0.5}NbTiZr$	129.184	As-cast	[62]
$HfMo_{0.25}NbTaTiZr$	94.510	As-cast	[23]
$HfMo_{0.5}NbTaTiZr$	112.468	As-cast	[23]
$HfMo_{0.75}NbTaTiZr$	117.773	As-cast	[23]
HfMoNbTaTiWZr	123.809	As-Cast	[63]
HfMoNbTaTiZr	130.233	As-Cast	[64]

Table 1 Continued

Composition	Specific Yield Strength (RT) [MPa/(g/cm^3)]	Processing	Reference
HfMoNbTaTiZr	130.233	As-cast	[64]
HfMoNbTiZr	160.550	annealed	[65]
HfMoScTaZr	148.080	As-Cast	[66]
HfMoTaTiZr	132.385	As-Cast	[64]
HfNbSi$_{0.5}$TiV	144.034	As-Cast	[67]
HfNbSi$_{0.5}$TiVZr	163.003	annealed	[68]
HfNbSi$_{0.5}$TiVZr	169.268	As-Cast	[68]
HfNbTaTi	65.177	Heat Treatment	[54]
HfNbTaTiWZr	114.113	As-Cast	[63]
HfNbTaTiZr	85.828	As-cast	[23]
HfNbTaTiZr	78.556	HIP+annealed	[19]
HfNbTiVZr	124.368	Annealed	[58]
HfNbTiZr	31.959	As-Cast	[16]
Mo$_{0.1}$NbTiV$_{0.3}$Zr	133.162	As-Cast	[69]
Mo$_{0.3}$NbTiV$_{0.3}$Zr	181.541	As-Cast	[69]
Mo$_{0.3}$NbTiVZr	181.575	As-Cast	[69]
Mo$_{0.5}$NbTiV$_{0.3}$Zr	175.195	As-Cast	[69]
Mo$_{0.5}$NbTiVZr	202.224	As-Cast	[69]
Mo$_{0.7}$NbTiV$_{0.3}$Zr	188.947	As-Cast	[69]
Mo$_{0.7}$NbTiVZr	229.055	As-Cast	[69]
Mo$_{1.3}$NbTiV$_{0.3}$Zr	200.000	As-Cast	[69]
Mo$_{1.3}$NbTiVZr	190.622	As-Cast	[69]
Mo$_{1.5}$NbTiV$_{0.3}$Zr	193.945	As-Cast	[69]
Mo$_{1.5}$NbTiVZr	201.458	As-Cast	[69]
Mo$_{1.7}$NbTiVZr	204.170	As-Cast	[69]
Mo$_2$NbTiVZr	215.454	As-Cast	[69]
MoNbTaTi	100.933	Heat Treatment	[54]
MoNbTaTi$_{0.25}$W	74.781	As-Cast	[70]
MoNbTaTi$_{0.5}$W	82.849	As-Cast	[70]
MoNbTaTi$_{0.75}$W	90.486	As-Cast	[70]
MoNbTaTiVW	111.545	As-Cast	[71]
MoNbTaTiW	94.484	As-Cast	[70]
MoNbTaTiW	102.364	As-Cast	[71]
MoNbTaTiZr	126.203	As-Cast	[72]
MoNbTaVW	87.133	As-Cast	[71]

Table 1 Continued

Composition	Specific Yield Strength (RT) [MPa/(g/cm^3)]	Processing	Reference
MoNbTaW	64.603	As-Cast	[71]
MoNbTaW	60.817	As-Cast	[70]
MoNbTaWZr	114.771	As-Cast	[73]
MoNbTaWZr$_{0.1}$	90.781	As-Cast	[73]
MoNbTaWZr$_{0.5}$	101.437	As-Cast	[73]
MoNbTiV$_{0.3}$Zr	126.401	As-Cast	[69]
MoNbTiVZr	232.155	As-Cast	[69]
MoTaTiV	101.353	As-Cast	[45]
NbTaTi	45.803	CR+Heat Treat	[54]
NbTaTiV	102.793	As-Cast	[74]
NbTaTiV	106.489	Heat Treatment	[74]
NbTaTiVZr	127.211	As-Cast	[74]
NbTaTiVZr	142.830	Heat Treatment	[74]
NbTaTiW	70.584	Heat Treatment	[54]
NbTiV$_{0.3}$Zr	126.019	As-Cast	[69]
NbTiV2Zr	137.549	HIP	[60]
NbTiVZr	162.928	As-Cast	[69]
NbTiVZr	163.076	HIP	[60]

Microstructure and Properties

Density

Alloy density is often used to calculate the specific yield strength in comparison to overall yield strength. This can be useful when looking into applications where weight savings are highly sought after. The formula for calculating the density of an alloy is:

$$\rho_{T=}\frac{(\rho_a \cdot M_a \cdot c_a + \rho_b \cdot M_b \cdot c_b + \rho_c \cdot M_c \cdot c_c)}{(M_a \cdot c_a + M_b \cdot c_b + M_c \cdot c_c)}$$

where ρ_a is the density of element a, M_a is the molar mass of element a, and c_a is the number of moles of element a in the overall alloy. This can be used to calculate equimolar and non-equimolar alloys and is not limited to the number of elements present in the alloy.

D-Parameter

The typical evaluation of ductility for solid solution models are first-principle calculations using Pugh's modulus, lattice instability mechanisms, and the Rice criterion. Instead of using these calculations that may not be as accurate in predicting intrinsic ductility, the D-parameter is used. The D-parameter can be used to predict intrinsic ductility for the alloys containing transition metals, specifically refractory metals. The difficulty in predicting ductility and other properties of these alloys is due to their unfilled d-orbital. As the ratio for calculating the D-parameter increases, so does the potency for intrinsic ductility. The D-parameter is the ratio of the surface energy (γ_{surf}) and unstable stacking fault energy (γ_{usf}) commonly presented as $D = \frac{\gamma_{surf}}{\gamma_{usf}}$. Where shown, the D-parameter is calculated from a surrogate model using an open-access code, available at https://doi.org/10.13011/m3-rkg0-zh65. [9]

Valence Electron Count

The VEC has been commonly used to predict the phases and phase stability of HEAs. The phase stability is necessary to understand the mechanism involved when HEAs are placed under strain. The VEC has been used to find correlations relating the value of VEC to certain phases[10]. This idea was first introduced for multi-component alloys, stating that a VEC ≥ 8 predicts a stable FCC phase, a VEC ≤ 6.87 predicts a stable BCC phase, and a VEC between 8 and 6.87 results in a mixture of the phases [11, 12]. VEC is calculated as the overall sum of the VEC of each component multiplied by the mole percent of the component.

$$VEC = \sum_{i=1}^{n} c_i (VEC)_i$$

Phase

RHEAs are most commonly seen as multiphase, with a select few being single-phase BCC. The importance of phase comes with the prediction of mechanical properties and intrinsic ductility [13]. While the D-parameter does allow some prediction for ductility, many compositions require much more extensive DFT calculations, and often times are limited to pre and post-mortem characterization of phases [14]. Many RHEAs have been studied in hopes of finding transformation-induced plasticity (TRIP) [15]. TRIP RHEAs have the possibility of being ductile while retaining high strength past the yield strength. For some RHEAs, a single phase is desired, and having a correlation to composition or another characteristic of RHEAs will have the ability to predict a desired phase. When coupling the VEC with the reported phase, more accurate predictions can be made for future fabrication of RHEAs.

Atomic-Size Mismatch

Atomic Size Mismatch (δ) can be thought of as the measure of differences between atomic radii. It is calculated as:

$$\delta = \sqrt{\sum_{i=1}^{n} c_i (1 - \frac{r_i}{\bar{r}})^2}$$

where c is the atomic percent of the component, r is the atomic radius, and $\bar{r}$ is the average atomic radius of the alloy [16]. It is associated with the lattice distortion and sluggish diffusion, two of the four core effects of HEAs. Lattice distortion is often used to predict microstructural properties, thermodynamic stabilities, deformation mechanisms, and phase changes of HEAs. The atomic size mismatch has been adopted as a substitute for the lattice distortion to predict different properties [17]. To ensure the accuracy of the comparisons of this dataset, the metallic atomic radii from Wolsey et al. has been used for each composition [18] . The actual value of δ is only for comparisons in this collection, but all calculations must use the same scale of atomic radii for the comparison to have any significance of correlations.

Configurational Entropy

The configurational entropy is often time substituted by the Entropy of Mixing (ΔS_{mix}) to lower the difficulty of calculations. This entropy can be thought of as the chaos of the system, and as shown by the equation below, the higher the number of components, the higher or more chaotic the system will be. When considering equimolar HEAs, the value of

$$\Delta S = R \ln (5)$$

is often used to describe the lowest entropy needed to overcome the strong bonds between atoms at high temperatures. Using the Gibbs Free Energy Equation:

$$\Delta G = \Delta H - T\Delta S$$

It is shown that the higher the entropy of mixing (especially at high temperatures), the lower Gibbs Free energy will be. To achieve the most stability, Gibbs Free energy should be a minimum, which forms a simple solid solution [1]. For a non-equimolar HEAs:

$$\Delta S_{mix} = -R \sum_{i=1}^{n} c_i \ln (c_i)$$

where c is the mole percent of the component and the gas constant R=8.3145 J/mol. For equimolar HEAs:

$$\Delta S_{mix} = Rln(n)$$

where n is the number of components [1].

Processing and Composition

In this dataset, an overall compilation is shown, along with a separation by the processing methods of the RHEAs. These sections will be As-Cast, Heat Treatment, and Hot-Isostatically-Pressed materials. These separations are helpful in furthering the knowledge of the fabrication of RHEAs, to allow for researchers to fabricate their materials based on the desired qualities. To accompany the separations by processing parameters, the RHEA dataset will be separated by the number of components, and the addition of non-refractory elements.

Dataset Categories and Compilations

Reasoning for use of Specific Yield Strength

For the comparisons in the RHEA dataset, the specific yield strength was used instead of the overall yield strength for a better comparison of the quality of the alloys. The specific yield strength is simply the yield strength divided by the density of the alloy.

Overall Compilation

For the overall dataset, a trend is not seen, but the chart shows the wide range of values possible with RHEAs. The potential for high-strength materials outside of high temperature uses is high for RHEAs, and when comparing the specific yield strength to other modern high-strength alloys, the merit of studying the design of RHEAs can be seen. The overall dataset is shown in Table 1.

D-Parameter

Information on the RHEAs with calculated D-parameters are shown in Table 2. Figure 1 shows the comparison of the D-parameter versus specific yield strength separated by RHEAs containing Mo and Ta. The Mo containing RHEAs are seen residing in the central portion of the graph, with an overall trend of as specific yield strength increases, the d-parameter decreases. This is not unexpected, as alloys that are more ductile are typically lower in yield than more brittle ones. Figure 2 shows the RHEAs separated by V and Zr containing alloys, similar to the separation of Mo and Ta, V containing RHEAs are seen throughout the graph, but primarily in the central portion. For both separations, there is not an overall grouping or trend based on composition.

To verify the accuracy of the D-Parameter as an intrinsic ductility gauge, a comparison was made with the percent plasticity of the RHEAs in the dataset. Unfortunately, there is not a correlation seen in Figure 3. It would be easy to conclude that the lack of correlation means that the D-Parameter is not an accurate gauge for ductility, but it is more likely due to the small number of alloys with which a D-Parameter has been calculated. Along with the small sample size, using solely compression tests for percent plasticity will not yield the most conclusive results. Without complete failures in the samples, the percent plasticity will not be as accurate elongation to failure from tensile tests.

Table 2: Specific Yield Strength versus D-Parameter

Composition	Specific Yield Strength [MPa/(g/cm^3)]	D-Parameter
MoNbTaW	64.603	2.113
MoNbTaW	60.817	2.113
$MoNbTaWZr_{0.1}$	90.781	2.152
$MoNbTaTi_{0.25}W$	74.781	2.233
$MoNbTaWZr_{0.5}$	101.437	2.276
MoNbTaVW	87.133	2.278
$MoNbTaTi_{0.5}W$	82.849	2.335
MoNbTaWZr	114.771	2.376
$MoNbTaTi_{0.75}W$	90.486	2.424
MoNbTaTiW	94.484	2.498
MoNbTaTiW	102.364	2.498
MoNbTaTiVW	111.545	2.575
$Mo_2NbTiVZr$	215.454	2.619
$Mo_{1.7}NbTiVZr$	204.170	2.687
$Mo_{1.5}NbTiV_{0.3}Zr$	193.945	2.731
$Mo_{1.5}NbTiVZr$	201.458	2.738
MoNbTaTi	100.933	2.770
$Mo_{0.7}NbTiV_{0.3}Zr$	188.947	2.793
$Mo_{1.3}NbTiV_{0.3}Zr$	200.000	2.793
$Mo_{1.3}NbTiVZr$	190.622	2.795
MoTaTiV	101.353	2.805
HfMoNbTaTiWZr	123.809	2.824
MoNbTiVZr	232.155	2.890
$Mo_{0.1}NbTiV_{0.3}Zr$	133.162	2.894
$MoNbTiV_{0.3}Zr$	126.401	2.894
NbTaTiW	70.584	2.898
MoNbTaTiZr	126.203	2.907
$Mo_{0.7}NbTiVZr$	229.055	3.000
HfMoNbTaTiZr	130.233	3.073
$Mo_{0.5}NbTiVZr$	202.224	3.085
HfMoNbTiZr	160.550	3.088

Table 2 Continued

Composition	Specific Yield Strength [MPa/(g/cm^3)]	D-Parameter
$Mo_{0.5}NbTiV_{0.3}Zr$	175.195	3.106
HfMoTaTiZr	132.385	3.121
$HfMo_{0.75}NbTaTiZr$	117.773	3.158
$Mo_{0.3}NbTiVZr$	181.575	3.185
$Mo_{0.3}NbTiV_{0.3}Zr$	181.541	3.226
$NbTiV_2Zr$	137.549	3.230
$Hf_{0.5}Mo_{0.5}NbTiZr$	129.184	3.237
NbTaTiV	102.793	3.253
NbTaTiV	106.489	3.253
$HfMo_{0.5}NbTaTiZr$	112.468	3.260
NbTaTiVZr	127.211	3.309
NbTaTiVZr	142.830	3.309
NbTaTi	45.803	3.365
NbTiVZr	162.928	3.370
NbTiVZr	163.076	3.370
$HfMo_{0.25}NbTaTiZr$	94.510	3.388
$NbTiV_{0.3}Zr$	126.019	3.485
HfNbTaTi	65.177	3.492
HfNbTaTiWZr	114.113	3.552
HfNbTaTiZr	85.828	3.552
HfNbTaTiZr	78.556	3.552
HfNbTiVZr	124.368	3.569
HfNbTiZr	31.959	3.821

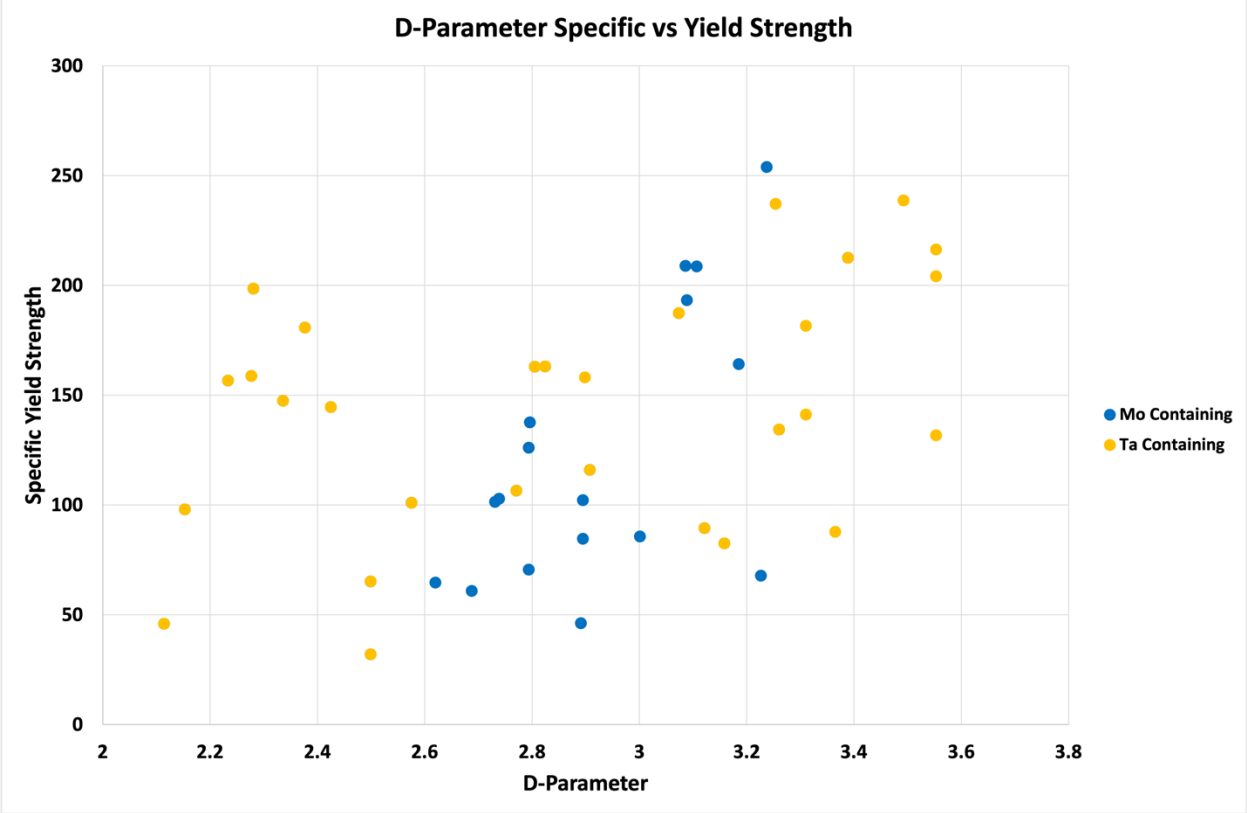


Figure 1: D-Parameter Comparison of Mo and Ta Containing RHEAs

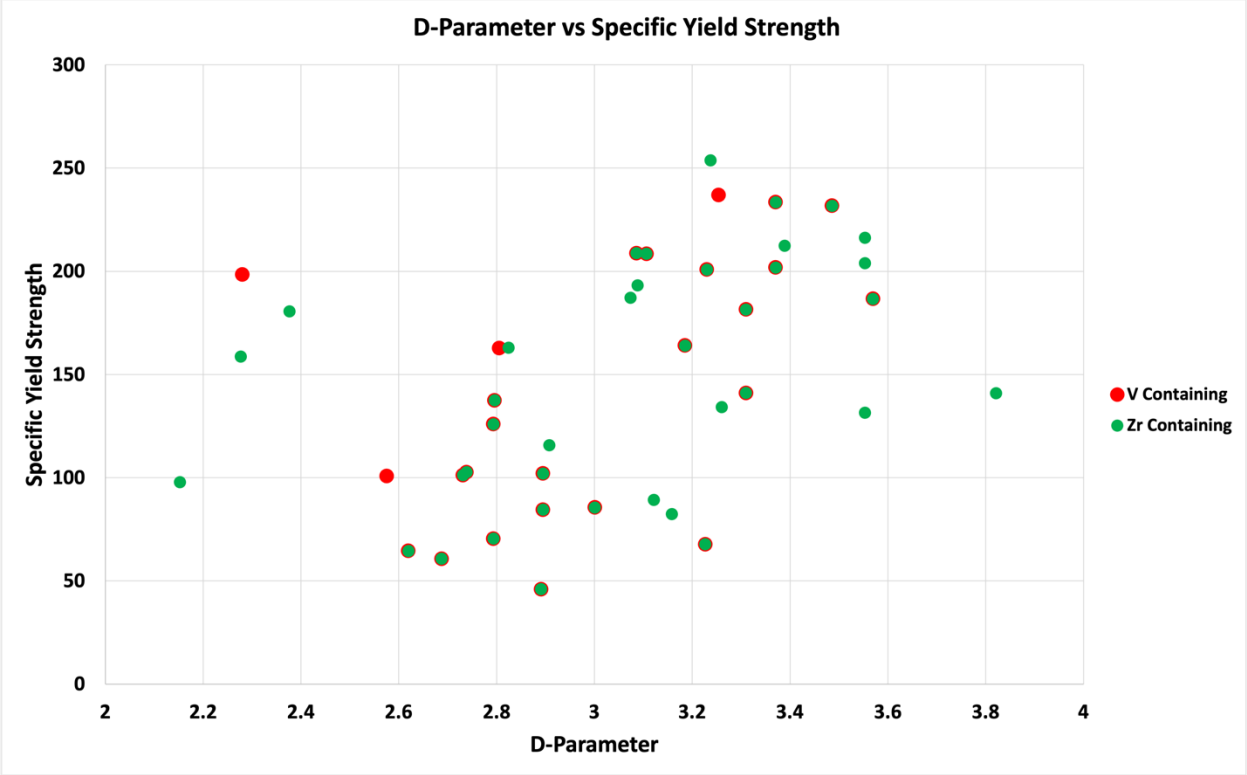


Figure 2: D-Parameter Comparison of V and Zr Containing RHEAs

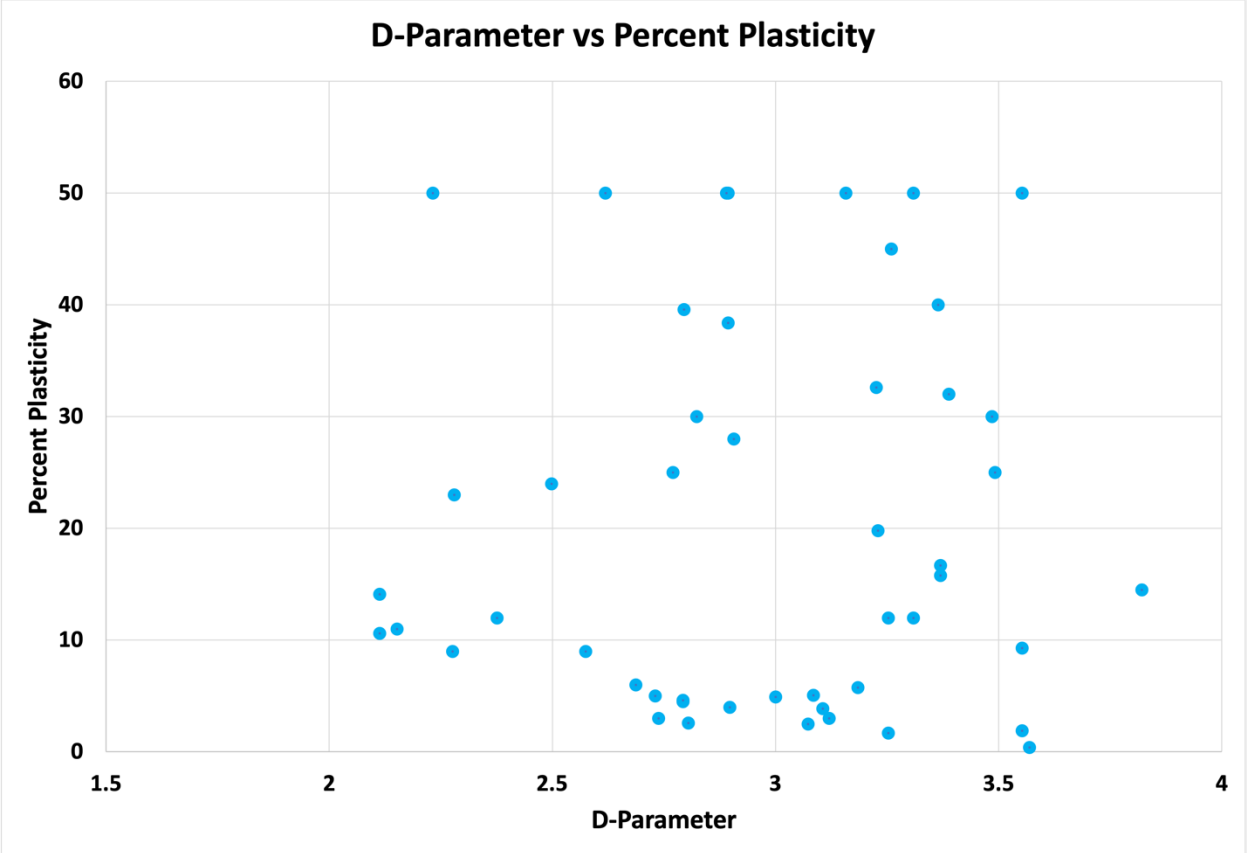


Figure 3: D-Parameter versus Percent Plasticity

Table 3 shows the values for the specific yield strength alongside the atomic-size mismatch (δ) of the RHEAs. For alloys with a precipitate, such as aluminum, there is a large atomic size mismatch, which leads to having some outliers. There is a slight upward trend shown in Figure 4, but with the overall great strength of RHEAs, the ductility criteria are more important for comparison. The RHEAs are separated by W and Mo containing and non-refractory containing alloys. There is a grouping of W and Mo containing RHEAs in the lower, left-hand side of the graph corresponding to a lowering δ and specific yield strength. This is due to the higher density of W and Mo, along with less difference in atomic radii from RHEAs with no non-refractory additions.

Percent Plasticity versus Atomic-Size Mismatch

Figure 5 shows a comparison of atomic-size mismatch and percent plasticity. There are no strong correlations, but it can be seen that most of the higher percent of plasticity are in the lower region of atomic-size mismatch. This could mean that too high of an atomic-size mismatch in RHEAs leads to a more brittle alloy. This cannot be proven with the small dataset shown here but would become more accurate with a larger dataset and specifically tension testing data.

Atomic Size Mismatch versus D-Parameter

Table 4 shows the values for the D-Parameters of select RHEAs. Using the program from https://doi.org/10.13011/m3-rkg0-zh65, only certain compositions are included due to the limits of what RHEAs can have the D-Parameter calculated. The chart shown in Figure 6 appears to have an upward “banana curve”, highlighting that a sharp increase in ductility may occur with an increase of atomic size mismatch.

Table 3: Specific Yield Strength versus Atomic Size Mismatch

Composition	Specific Yield Strength [MPa/(g/cm^3)]	δ [%] Atomic Size Mismatch
$Al_{0.25}HfNbTiZr$	46.085	4.564
$Al_{0.50}HfNbTiZr$	84.626	4.586
$Al_{0.75}HfNbTiZr$	102.124	4.653
$Al_{0.25}MoNbTiV$	158.088	3.646
$Al_{0.25}NbTaTiV$	115.894	3.627
$Al_{0.2}MoTaTiV$	85.690	3.668
$Al_{0.3}HfNbTaTiZr$	101.512	4.438
$Al_{0.3}NbTa_{0.8}Ti_{1.4}V_{0.2}Zr_{1.3}$	198.786	5.196
$Al_{0.3}NbTaTi_{1.4}Zr_{1.3}$	187.303	4.240
$Al_{0.4}Hf_{0.6}NbTaTiZr$	160.913	4.303
$Al_{0.4}Hf_{0.6}NbTaTiZr$	160.913	4.303
$Al_{0.5}CrNbTi_2V_{0.5}$	208.885	5.608
$Al_{0.5}CrNbTi_2V_{0.5}$	193.297	5.608
$Al_{0.5}HfNbTaTiZr$	112.019	4.448
$Al_{0.5}MoNbTiV$	208.601	3.533
$Al_{0.5}NbTa_{0.8}Ti_{1.5}V_{0.2}Zr$	204.502	4.654
$Al_{0.5}NbTaTiV$	89.376	3.509
$Al_{0.6}MoTaTiV$	82.497	2.937
$Al_{0.75}HfNbTaTiZr$	122.787	4.460
$Al_{0.75}MoNbTiV$	164.105	3.465
$Al_{1.5}MoNbTiV$	67.833	3.234
$AlCr_{0.5}NbTiV$	200.958	4.821
$AlCr_{1.5}NbTiV$	253.883	5.639
$AlCrNbTiV$	237.076	5.295
$AlHfNbTaTiZr$	130.283	4.465
$AlHfNbTiZr$	134.319	4.683
$AlMo_{0.5}NbTa_{0.5}TiZr$	216.169	4.516
$AlMo_{0.5}NbTa_{0.5}TiZr$	216.169	4.516
$AlMo_{0.5}NbTa_{0.5}TiZr$	216.169	4.516
$AlMoNbTiV$	181.614	3.379
$AlNb_{1.5}Ta_{0.5}Ti_{1.5}Zr_{0.5}$	141.125	3.174
$AlNbTaTi$	97.949	1.031
$AlNbTaTiV$	87.684	3.346
$AlNbTiV$	156.666	3.595
$AlNbTiVZr$	233.608	5.731

Table 3 Continued

Composition	Specific Yield Strength [MPa/(g/cm^3)]	δ [%] Atomic Size Mismatch
$AlNbTiVZr_{0.1}$	201.910	4.454
$AlNbTiVZr_{0.25}$	212.500	4.731
$AlNbTiVZr_{0.5}$	231.850	5.100
$AlNbTiVZr_{1.5}$	238.613	6.185
$C_{0.1}Hf_{0.5}Mo_{0.5}NbTiZr$	133.206	14.072
$C_{0.3}Hf_{0.5}Mo_{0.5}NbTiZr$	135.890	17.599
CoCrMoNb	158.783	6.276
CoCrMoNbTi	131.661	6.610
$CoCrMoNbTi_{0.2}$	216.330	6.469
$CoCrMoNbTi_{0.4}$	204.103	6.507
$CoCrMoNbTi_{0.5}$	186.767	6.525
CrHfNbTiZr	141.007	7.822
$CrMo_{0.5}NbTa_{0.5}TiZr$	169.321	7.185
CrMoNbTi	198.515	5.416
CrMoTaTi	147.421	5.416
CrNbTiVZr	189.766	7.787
CrNbTiZr	180.749	7.840
$CrTaTi_{0.04}VW$	131.838	5.001
$CrTaTi_{0.07}VW$	133.169	5.005
CrTaVW	144.584	4.833
$Hf_{0.5}Mo_{0.5}NbSi_{0.1}TiZr$	152.491	7.829
$Hf_{0.5}Mo_{0.5}NbSi_{0.3}TiZr$	156.464	9.082
$Hf_{0.5}Mo_{0.5}NbSi_{0.5}TiZr$	184.715	10.084
$Hf_{0.5}Mo_{0.5}NbSi_{0.7}TiZr$	180.863	10.930
$Hf_{0.5}Mo_{0.5}NbSi_{0.9}TiZr$	194.553	4.997
$Hf_{0.5}Mo_{0.5}NbTiZr$	129.184	11.655
$HfMo_{0.25}NbTaTiZr$	94.510	4.704
$HfMo_{0.5}NbTaTiZr$	112.4678	4.829
$HfMo_{0.75}NbTaTiZr$	117.773	4.941
HfMoNbTaTiWZr	123.809	5.381

Table 3 Continued

Composition	Specific Yield Strength [MPa/(g/cm^3)]	δ [%] Atomic Size Mismatch
HfMoNbTaTiZr	130.233	5.047
HfMoNbTaTiZr	130.233	5.047
HfMoNbTiZr	160.550	5.383
HfMoScTaZr	148.080	5.917
HfMoTaTiZr	132.385	5.383
$HfNbSi_{0.5}TiV$	144.034	10.240
$HfNbSi_{0.5}TiVZr$	163.003	10.208
$HfNbSi_{0.5}TiVZr$	169.268	10.208
HfNbTaTi	65.177	3.679
HfNbTaTiWZr	114.113	4.658
HfNbTaTiZr	85.828	4.267
HfNbTaTiZr	78.556	4.267
HfNbTiVZr	124.368	6.420
HfNbTiZr	31.959	4.261
$Mo_{0.1}NbTiV_{0.3}Zr$	133.162	6.036
$Mo_{0.3}NbTiV_{0.3}Zr$	181.541	5.987
$Mo_{0.3}NbTiVZr$	181.575	6.307
$Mo_{0.5}NbTiV_{0.3}Zr$	175.195	5.918
$Mo_{0.5}NbTiVZr$	202.224	6.221
$Mo_{0.7}NbTiV_{0.3}Zr$	188.947	5.838
$Mo_{0.7}NbTiVZr$	229.055	6.157
$Mo_{1.3}NbTiV_{0.3}Zr$	200.000	5.654
$Mo_{1.3}NbTiVZr$	190.622	5.975
$Mo_{1.5}NbTiV_{0.3}Zr$	193.945	5.608
$Mo_{1.5}NbTiVZr$	201.458	5.920
$Mo_{1.7}NbTiVZr$	204.170	5.861
$Mo_2NbTiVZr$	215.454	5.082
MoNbTaTi	100.933	2.216
$MoNbTaTi_{0.25}W$	74.781	2.518
$MoNbTaTi_{0.5}W$	82.849	2.518
$MoNbTaTi_{0.75}W$	90.486	2.521
MoNbTaTiVW	111.545	3.392
MoNbTaTiW	94.484	2.518
MoNbTaTiW	102.364	2.518
MoNbTaTiZr	126.203	4.627

Table 3 Continued

Composition	Specific Yield Strength [MPa/(g/cm^3)]	δ [%] Atomic Size Mismatch
MoNbTaVW	87.133	3.282
MoNbTaW	64.603	2.456
MoNbTaW	60.817	2.456
MoNbTaWZr	114.771	5.252
$MoNbTaWZr_{0.1}$	90.781	3.664
$MoNbTaWZr_{0.5}$	101.437	4.405
$MoNbTiV_{0.3}Zr$	126.400	5.749
MoNbTiVZr	232.155	6.057
MoTaTiV	101.353	3.756
NbTaTi	45.803	0.322
NbTaTiV	102.793	3.739
NbTaTiV	106.489	3.739
NbTaTiVZr	127.211	5.618
NbTaTiVZr	142.830	5.618
NbTaTiW	70.584	2.216
$NbTiV_{0.3}Zr$	126.019	5.627
$NbTiV_2Zr$	137.549	6.823
NbTiVZr	162.928	6.271
NbTiVZr	163.076	6.271

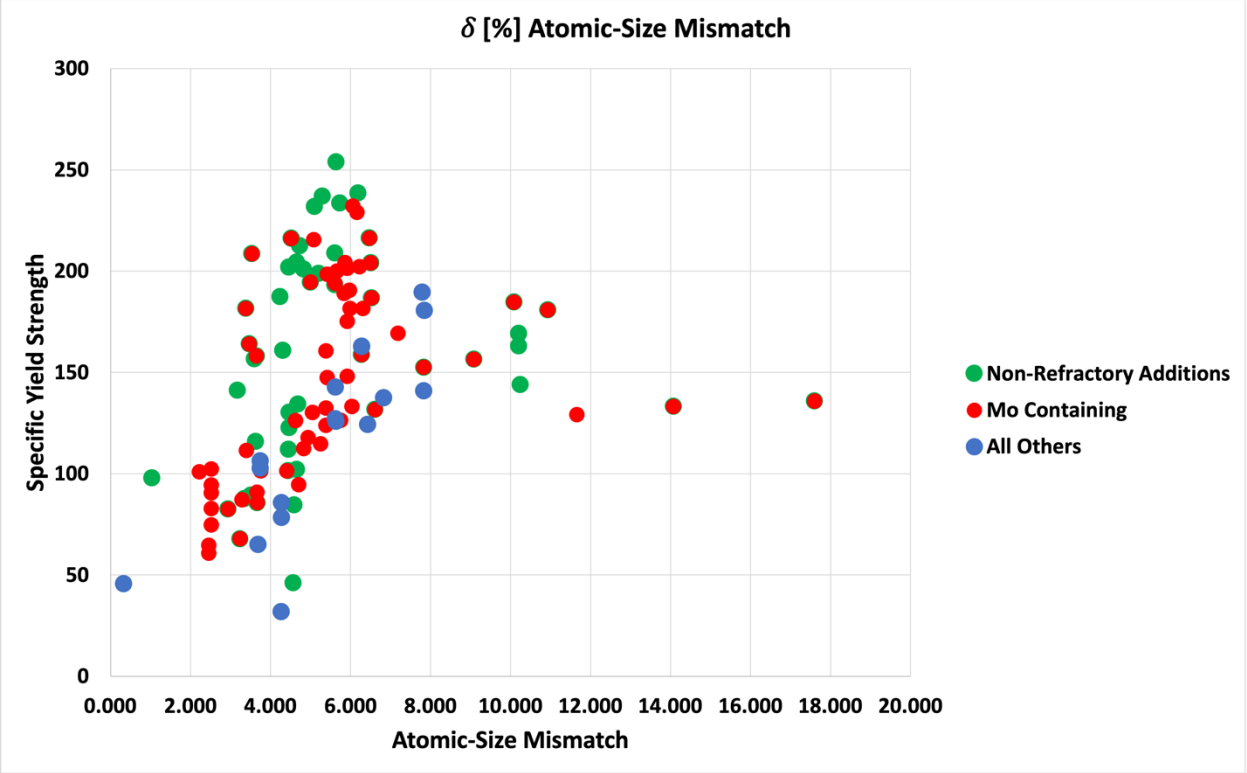


Figure 4: Atomic Size Mismatch of Studied RHEAs

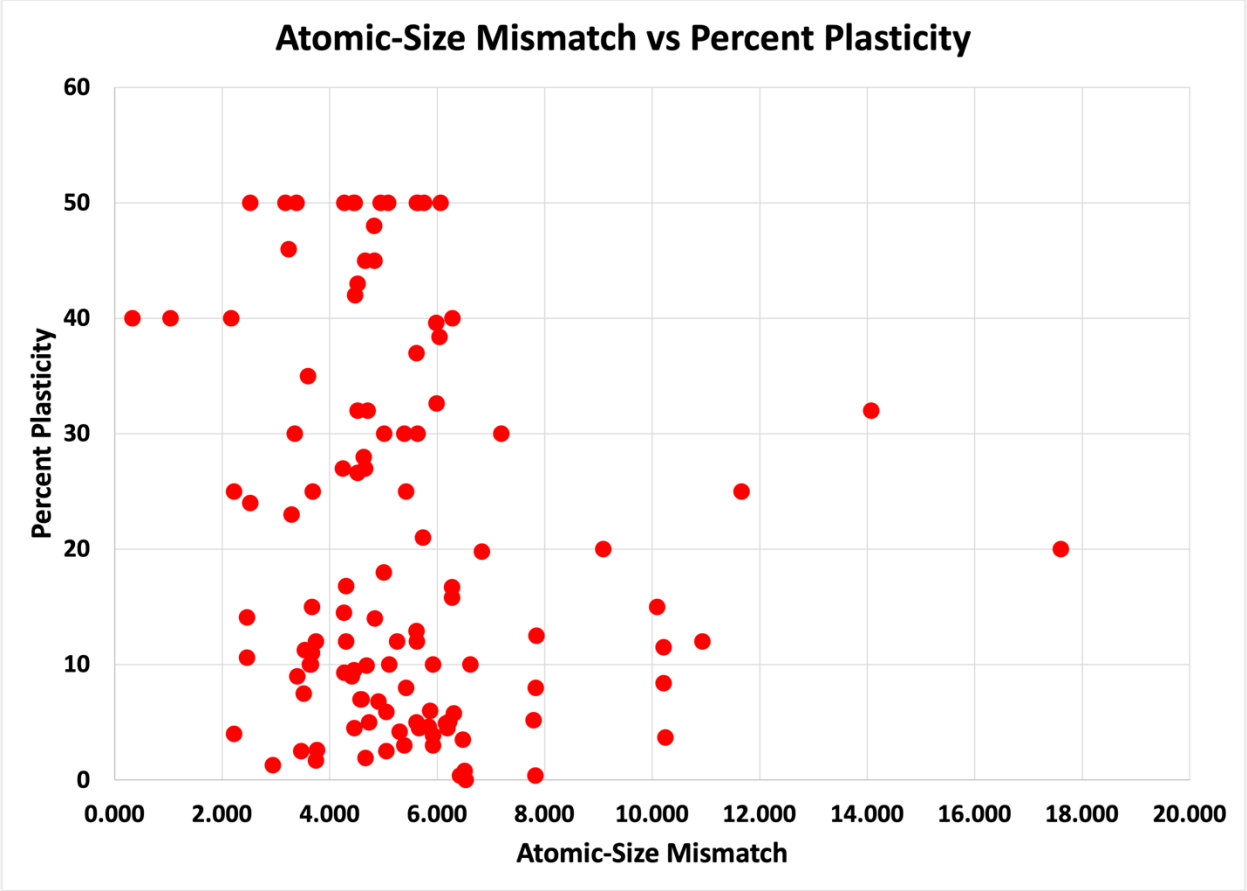


Figure 5: Atomic-Size Mismatch versus Percent Plasticity

Table 4: Atomic Size Mismatch versus D-Parameter

Composition	δ [%] Atomic Size Mismatch	D-Parameter
MoNbTaW	2.456	2.113
MoNbTaW	2.456	2.113
$MoNbTaWZr_{0.1}$	3.664	2.152
$MoNbTaTi_{0.25}W$	2.518	2.233
$MoNbTaWZr_{0.5}$	4.405	2.276
MoNbTaVW	3.282	2.280
$MoNbTaTi_{0.5}W$	2.518	2.335
MoNbTaWZr	5.252	2.376
$MoNbTaTi_{0.75}W$	2.521	2.424
MoNbTaTiW	2.518	2.498
MoNbTaTiW	2.518	2.498
MoNbTaTiVW	3.392	2.575
$Mo_2NbTiVZr$	5.082	2.619
$Mo_{1.7}NbTiVZr$	5.861	2.687
$Mo_{1.5}NbTiV_{0.3}Zr$	5.608	2.731
$Mo_{1.5}NbTiVZr$	5.920	2.738
MoNbTaTi	2.216	2.770
$Mo_{0.7}NbTiV_{0.3}Zr$	5.838	2.793
$Mo_{1.3}NbTiV_{0.3}Zr$	5.654	2.793
$Mo_{1.3}NbTiVZr$	5.975	2.795
MoTaTiV	3.756	2.805
HfMoNbTaTiWZr	5.381	2.824
MoNbTiVZr	6.057	2.890
$Mo_{0.1}NbTiV_{0.3}Zr$	6.036	2.894
$MoNbTiV_{0.3}Zr$	5.749	2.894
NbTaTiW	2.216	2.898
MoNbTaTiZr	4.627	2.907
$Mo_{0.7}NbTiVZr$	6.157	3.000
HfMoNbTaTiZr	5.047	3.072
$Mo_{0.5}NbTiVZr$	6.221	3.085
HfMoNbTiZr	5.383	3.088
$Mo_{0.5}NbTiV_{0.3}Zr$	5.918	3.106
HfMoTaTiZr	5.383	3.121
$HfMo_{0.75}NbTaTiZr$	4.941	3.158
$Mo_{0.3}NbTiVZr$	6.307	3.184

Table 4 Continued

Composition	δ [%] Atomic Size Mismatch	D-Parameter
$Mo_{0.3}NbTiV_{0.3}Zr$	5.987	3.226
NbTiV2Zr	6.823	3.230
$Hf_{0.5}Mo_{0.5}NbTiZr$	4.997	3.237
NbTaTiV	3.739	3.253
NbTaTiV	3.739	3.253
$HfMo_{0.5}NbTaTiZr$	4.829	3.260
NbTaTiVZr	5.618	3.309
NbTaTiVZr	5.618	3.309
NbTaTi	0.322	3.365
NbTiVZr	6.271	3.370
NbTiVZr	6.271	3.370
$HfMo_{0.25}NbTaTiZr$	4.704	3.388
$NbTiV_{0.3}Zr$	5.627	3.485
HfNbTaTi	3.679	3.492
HfNbTaTiWZr	4.658	3.552
HfNbTaTiZr	4.267	3.552
HfNbTaTiZr	4.267	3.552
HfNbTiVZr	6.420	3.569
HfNbTiZr	4.261	3.821

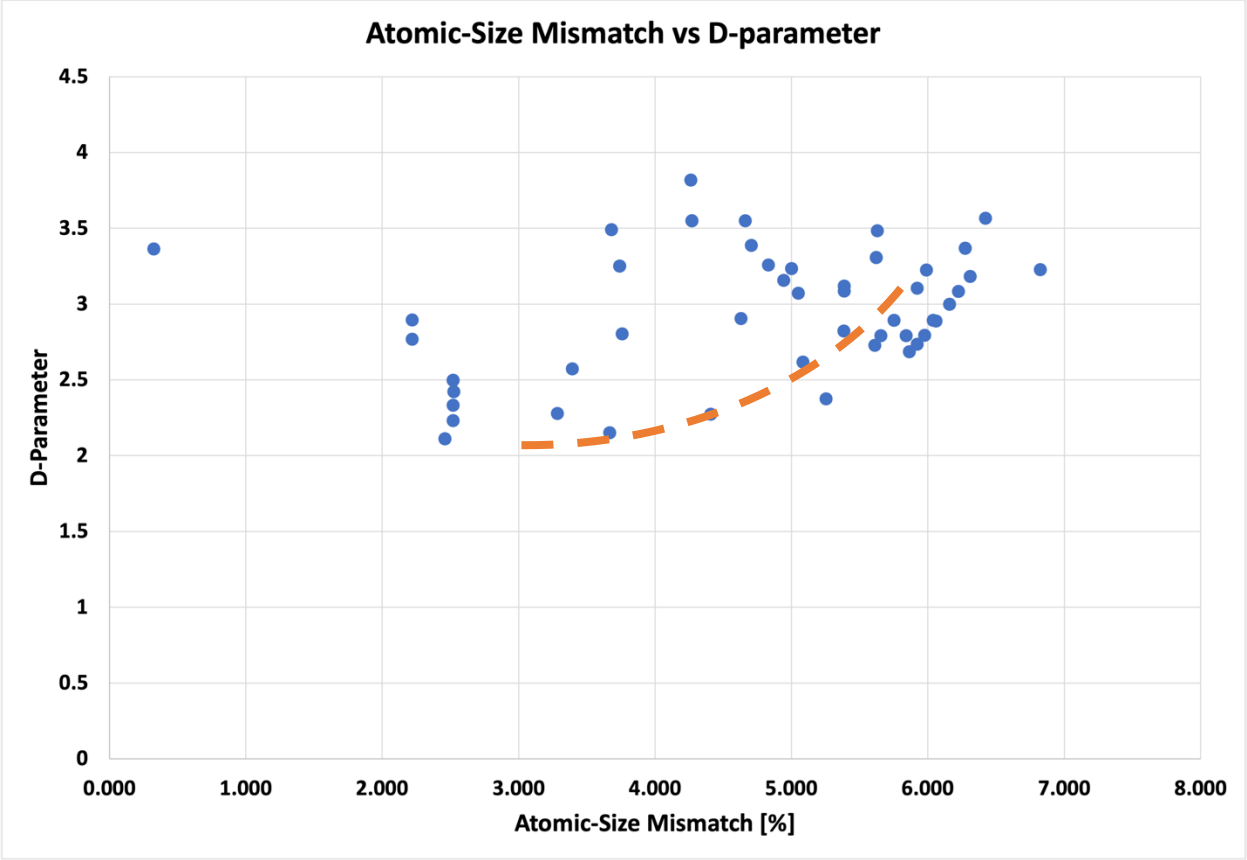


Figure 6: Atomic-Size Mismatch versus D-Parameter

Specific Yield Strength versus Entropy of Mixing

Table 5 shows the values of the Entropy of Mixing or ΔS_{mix} versus the specific yield strength. For this comparison there are no apparent correlations, but rather a range of acceptable values for the RHEAs. Figure 7 shows this comparison with almost all compositions falling at $11 < \Delta S_{mix} > 15 \frac{J}{mol \cdot K}$. The alloys have been separated by Mo and V containing non-refractory additions, and all other RHEAs with no overall groupings or correlations by composition.

Entropy of Mixing versus D-parameter

Table 6 shows the values of ΔS_{mix} versus the D-Parameter. Similar to Figure 7, there is not a correlation seen in Figure 8. There are a few separate areas of the graph where a slight correlation can be made for a certain grouping of compositions (i.e., Titanium containing RHEAs or something similar), but nothing that can be drawn to the overall category of RHEAs.

As-Cast, Annealed, and HIP Comparison

Table 7 shows the average value, standard deviation, minimum and maximum values, and range of the specific yield strength for as-cast RHEAs. Table 8 presents the average value, standard deviation, minimum and maximum values, and range of the specific yield strength for annealed RHEAs. Finally, Table 9 exhibits the average value, standard deviation, minimum and maximum values, and range of the specific yield strength for the HIP RHEAs.

Figure 9 shows the chart comparing the three processes described above. Alloys that are lighter and stronger will be in the upper left of the chart. Both annealed and HIP alloys are seen mainly in this area, which is expected, but not one process is seen as exclusively better than the others without considering differences in compositions.

Table 5: Specific Yield Strength versus Entropy of Mixing (ΔS_{mix})

Composition	Specific Yield Strength (RT) [MPa/(g/cm^3)]	ΔS
$Al_{0.25}HfNbTiZr$	64.603	12.71
$Al_{0.50}HfNbTiZr$	60.817	13.15
$Al_{0.75}HfNbTiZr$	90.781	13.33
$Al_{0.25}MoNbTiV$	74.781	12.71
$Al_{0.25}NbTaTiV$	101.437	12.71
$Al_{0.2}MoTaTiV$	87.133	12.57
$Al_{0.3}HfNbTaTiZr$	82.849	14.43
$Al_{0.3}NbTa_{0.8}Ti_{1.4}V_{0.2}Zr_{1.3}$	114.771	13.46
$Al_{0.3}NbTaTi_{1.4}Zr_{1.3}$	90.486	12.63
$Al_{0.4}Hf_{0.6}NbTaTiZr$	94.484	11.82
$Al_{0.4}Hf_{0.6}NbTaTiZr$	102.364	11.68
$Al_{0.5}CrNbTi_2V_{0.5}$	111.545	12.23
$Al_{0.5}CrNbTi_2V_{0.5}$	215.454	12.23
$Al_{0.5}HfNbTaTiZr$	204.170	14.70
$Al_{0.5}MoNbTiV$	193.945	13.15
$Al_{0.5}NbTa_{0.8}Ti_{1.5}V_{0.2}Zr$	201.458	13.78
$Al_{0.5}NbTaTiV$	100.933	13.15
$Al_{0.6}MoTaTiV$	188.947	13.24
$Al_{0.75}HfNbTaTiZr$	200.000	14.86
$Al_{0.75}MoNbTiV$	190.622	13.33
$Al_{1.5}MoNbTiV$	101.353	13.25
$AlCr_{0.5}NbTiV$	123.809	13.15
$AlCr_{1.5}NbTiV$	232.155	13.25
AlCrNbTiV	133.162	13.38
AlHfNbTaTiZr	126.401	14.90
AlHfNbTiZr	70.584	13.38
$AlMo_{0.5}NbTa_{0.5}TiZr$	126.203	11.86
$AlMo_{0.5}NbTa_{0.5}TiZr$	229.055	14.53
$AlMo_{0.5}NbTa_{0.5}TiZr$	130.233	14.53
AlMoNbTiV	202.224	13.38
$AlNb_{1.5}Ta_{0.5}Ti_{1.5}Zr_{0.5}$	160.550	12.51
AlNbTaTi	175.195	11.53
AlNbTaTiV	132.385	13.38
AlNbTiV	117.773	11.53
AlNbTiVZr	181.575	13.38

Table 5 Continued

Composition	Specific Yield Strength (RT) [MPa/(g/cm^3)]	ΔS
$AlNbTiVZr_{0.1}$	181.541	12.20
$AlNbTiVZr_{0.25}$	137.549	12.71
$AlNbTiVZr_{0.5}$	129.184	13.15
$AlNbTiVZr_{1.5}$	102.793	13.25
$C_{0.1}Hf_{0.5}Mo_{0.5}NbTiZr$	106.489	10.74
$C_{0.3}Hf_{0.5}Mo_{0.5}NbTiZr$	112.468	11.96
CoCrMoNb	127.211	11.53
CoCrMoNbTi	142.830	13.38
$CoCrMoNbTi_{0.2}$	45.803	12.57
$CoCrMoNbTi_{0.4}$	162.928	13.01
$CoCrMoNbTi_{0.5}$	163.076	13.15
CrHfNbTiZr	94.510	13.38
$CrMo_{0.5}NbTa_{0.5}TiZr$	126.019	14.53
CrMoNbTi	65.177	11.53
CrMoTaTi	114.113	11.53
CrNbTiVZr	85.828	13.38
CrNbTiZr	78.556	11.53
$CrTaTi_{0.04}VW$	124.368	11.87
$CrTaTi_{0.07}VW$	31.959	12.05
CrTaVW	46.0848	11.53
$Hf_{0.5}Mo_{0.5}NbSi_{0.1}TiZr$	84.626	13.60
$Hf_{0.5}Mo_{0.5}NbSi_{0.3}TiZr$	102.124	14.17
$Hf_{0.5}Mo_{0.5}NbSi_{0.5}TiZr$	158.088	14.43
$Hf_{0.5}Mo_{0.5}NbSi_{0.7}TiZr$	115.894	14.54
$Hf_{0.5}Mo_{0.5}NbTiZr$	85.690	12.97
$Hf_{0.5}Mo_{0.5}NbZrTiSi_{0.9}$	101.512	14.55
$HfMo_{0.25}NbTaTiZr$	198.786	14.34
$HfMo_{0.5}NbTaTiZr$	187.303	14.70
$HfMo_{0.75}NbTaTiZr$	160.913	14.86
HfMoNbTaTiWZr	160.913	16.18
HfMoNbTaTiZr	208.885	14.90
HfMoNbTaTiZr	193.297	14.90
HfMoNbTiZr	112.019	13.38
HfMoScTaZr	208.601	13.38
HfMoTaTiZr	204.502	13.38

Table 5 Continued

Composition	Specific Yield Strength (RT) [MPa/(g/cm^3)]	ΔS
$HfNbSi_{0.5}TiV$	89.376	13.15
$HfNbSi_{0.5}TiVZr$	82.497	14.70
$HfNbSi_{0.5}TiVZr$	122.787	14.70
HfNbTaTi	164.105	11.53
HfNbTaTiWZr	67.833	14.90
HfNbTaTiZr	200.958	13.38
HfNbTaTiZr	253.883	13.38
HfNbTiVZr	237.076	13.38
HfNbTiZr	130.283	11.53
$Mo_{0.1}NbTiV_{0.3}Zr$	134.319	11.62
$Mo_{0.3}NbTiV_{0.3}Zr$	216.169	12.32
$Mo_{0.3}NbTiVZr$	216.169	12.83
$Mo_{0.5}NbTiV_{0.3}Zr$	216.169	12.65
$Mo_{0.5}NbTiVZr$	181.614	13.15
$Mo_{0.7}NbTiV_{0.3}Zr$	141.125	12.80
$Mo_{0.7}NbTiVZr$	97.949	13.31
$Mo_{1.3}NbTiV_{0.3}Zr$	87.684	12.72
$Mo_{1.3}NbTiVZr$	156.667	13.33
$Mo_{1.5}NbTiV_{0.3}Zr$	233.608	12.61
$Mo_{1.5}NbTiVZr$	201.910	13.25
$Mo_{1.7}NbTiVZr$	212.500	13.15
$Mo_2NbTiVZr$	231.850	12.98
MoNbTaTi	238.613	11.53
$MoNbTaTi_{0.25}W$	133.206	12.71
$MoNbTaTi_{0.5}W$	135.890	13.15
$MoNbTaTi_{0.75}W$	158.783	13.33
MoNbTaTiVW	131.661	14.90
MoNbTaTiW	216.330	13.38
MoNbTaTiW	204.103	13.38
MoNbTaTiZr	186.767	13.38
MoNbTaVW	141.007	13.38
MoNbTaW	169.321	11.53
MoNbTaW	198.515	11.53
MoNbTaWZr	147.421	13.38
$MoNbTaWZr_{0.1}$	189.766	12.20

Table 5 Continued

Composition	Specific Yield Strength (RT) [MPa/(g/cm^3)]	ΔS
$MoNbTaWZr_{0.5}$	180.749	13.15
$MoNbTiV_{0.3}Zr$	131.838	12.83
MoNbTiVZr	133.169	13.38
MoTaTiV	144.584	11.53
NbTaTi	152.491	9.13
NbTaTiV	156.464	11.53
NbTaTiV	184.715	11.53
NbTaTiVZr	180.863	13.38
NbTaTiVZr	194.553	13.38
NbTaTiW	130.233	11.53
$NbTiV_{0.3}Zr$	148.080	10.83
NbTiV2Zr	144.034	11.08
NbTiVZr	163.003	11.53
NbTiVZr	169.268	11.53

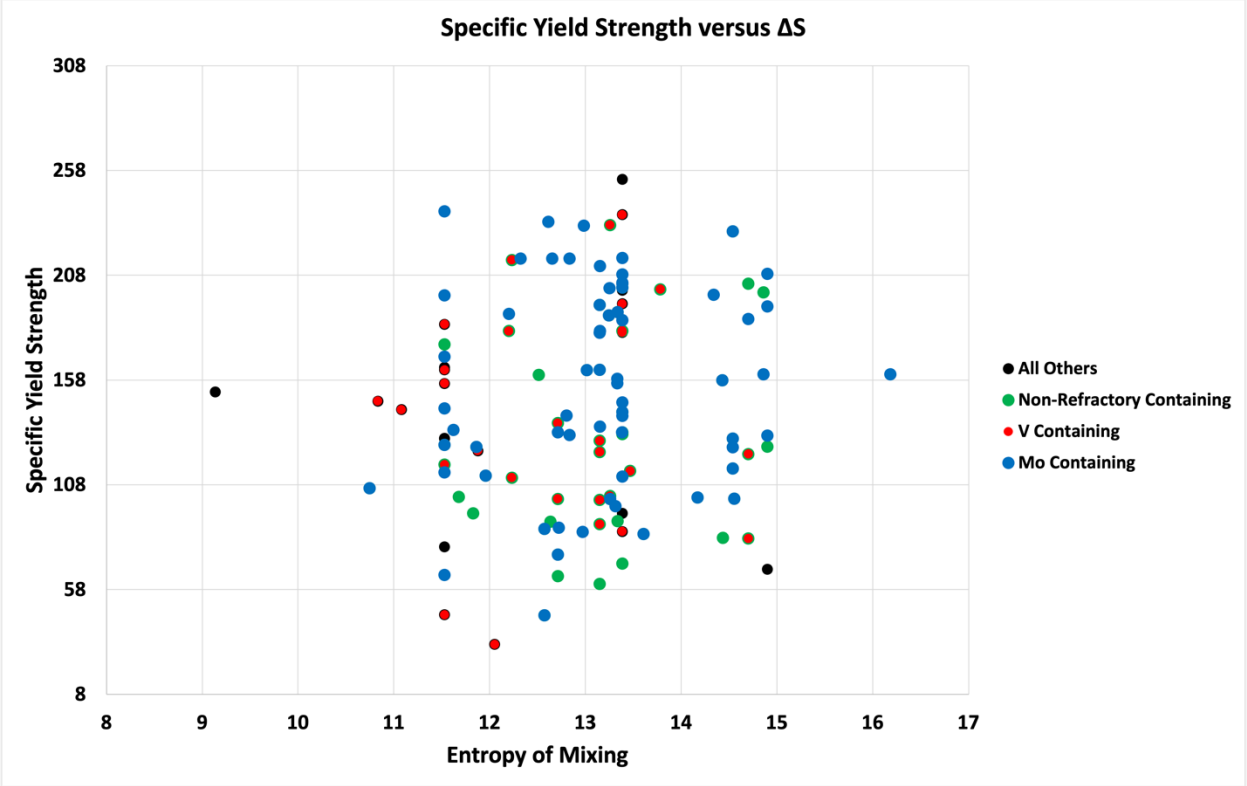


Figure 7: Entropy of Mixing (ΔS_{mix}) Comparison

Table 6: Entropy of Mixing (ΔS_{mix}) versus D-Parameter

Composition	ΔS	D-Parameter
MoNbTaW	11.526	2.113
MoNbTaW	11.526	2.113
$MoNbTaWZr_{0.1}$	12.199	2.152
$MoNbTaTi_{0.25}W$	12.710	2.233
$MoNbTaWZr_{0.5}$	13.146	2.276
MoNbTaVW	13.382	2.280
$MoNbTaTi_{0.5}W$	13.150	2.335
MoNbTaWZr	13.382	2.376
$MoNbTaTi_{0.75}W$	13.330	2.424
MoNbTaTiW	13.382	2.498
MoNbTaTiW	13.382	2.498
MoNbTaTiVW	14.898	2.575
$Mo_2NbTiVZr$	12.980	2.619
$Mo_{1.7}NbTiVZr$	13.150	2.687
$Mo_{1.5}NbTiV_{0.3}Zr$	12.610	2.731
$Mo_{1.5}NbTiVZr$	13.250	2.738
MoNbTaTi	11.526	2.770
$Mo_{0.7}NbTiV_{0.3}Zr$	12.800	2.793
$Mo_{1.3}NbTiV_{0.3}Zr$	12.720	2.793
$Mo_{1.3}NbTiVZr$	13.330	2.795
MoTaTiV	11.526	2.805
HfMoNbTaTiWZr	16.179	2.824
MoNbTiVZr	13.380	2.890
$Mo_{0.1}NbTiV_{0.3}Zr$	11.620	2.894
MoNbTiV0.3Zr	12.830	2.894
NbTaTiW	11.526	2.898
MoNbTaTiZr	13.382	2.907
$Mo_{0.7}NbTiVZr$	13.310	3.000
HfMoNbTaTiZr	14.898	3.073
$Mo_{0.5}NbTiVZr$	13.150	3.085
HfMoNbTiZr	13.382	3.088
$Mo_{0.5}NbTiV_{0.3}Zr$	12.650	3.106
HfMoTaTiZr	13.382	3.121
$HfMo_{0.75}NbTaTiZr$	14.856	3.158
$Mo_{0.3}NbTiVZr$	12.830	3.185

Table 6 Continued

Composition	ΔS	D-Parameter
$Mo_{0.3}NbTiV_{0.3}Zr$	12.320	3.226
$NbTiV_2Zr$	11.076	3.230
$Hf_{0.5}Mo_{0.5}NbTiZr$	12.967	3.237
NbTaTiV	11.526	3.253
NbTaTiV	11.526	3.253
$HfMo_{0.5}NbTaTiZr$	14.698	3.260
NbTaTiVZr	13.382	3.309
NbTaTiVZr	13.382	3.309
NbTaTi	9.134	3.365
NbTiVZr	11.526	3.370
NbTiVZr	11.526	3.370
$HfMo_{0.25}NbTaTiZr$	14.336	3.388
$NbTiV_{0.3}Zr$	10.830	3.485
HfNbTaTi	11.526	3.491
HfNbTaTiWZr	14.898	3.552
HfNbTaTiZr	13.382	3.552
HfNbTaTiZr	13.382	3.552
HfNbTiVZr	13.382	3.569
HfNbTiZr	11.526	3.821

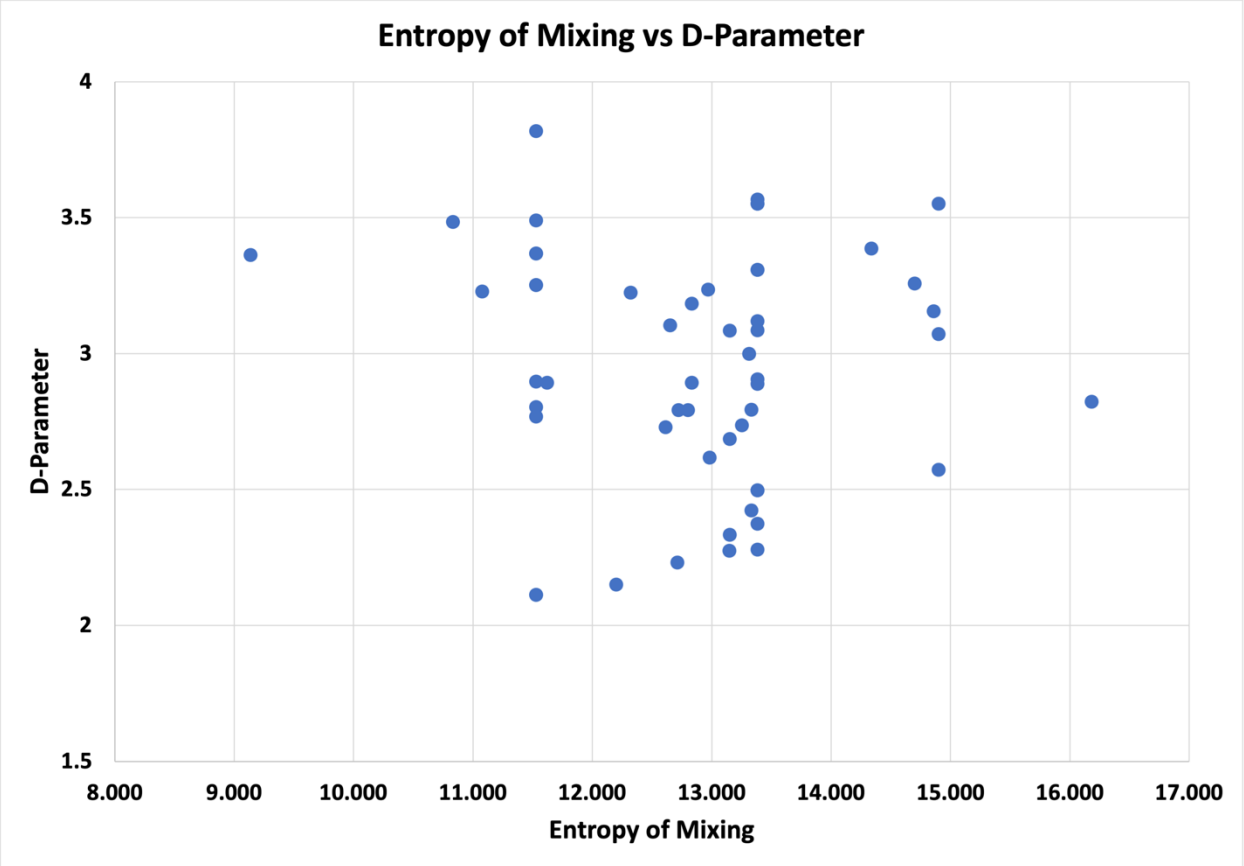


Figure 8: Entropy of Mixing (ΔS_{mix}) versus D-Parameter

Table 7: Statistics on Specific Yield Strength of As-Cast RHEAs

Average Yield [MPa/(g/cm^3)]:	139.68
Standard Deviation [MPa/(g/cm^3)]:	49.30
Minimum Yield [MPa/(g/cm^3)]:	31.96
Maximum Yield [MPa/(g/cm^3)]:	253.88
Range [MPa/(g/cm^3)]:	221.92

Table 8: Statistics on Specific Yield Strength of Annealed RHEAs

Average Yield [MPa/(g/cm^3)]:	201.54
Standard Deviation [MPa/(g/cm^3)]:	39.88
Maximum Yield [MPa/(g/cm^3)]:	238.61
Minimum Yield [MPa/(g/cm^3)]:	124.37
Range [MPa/(g/cm^3)]:	114.25

Table 9: Statistics on Specific Yield Strength of HIP RHEAs

Average Yield [MPa/(g/cm^3)]:	172.61
Standard Deviation [MPa/(g/cm^3)]:	38.06
Maximum Yield [MPa/(g/cm^3)]:	216.17
Minimum Yield [MPa/(g/cm^3)]:	78.56
Range [MPa/(g/cm^3)]:	137.61

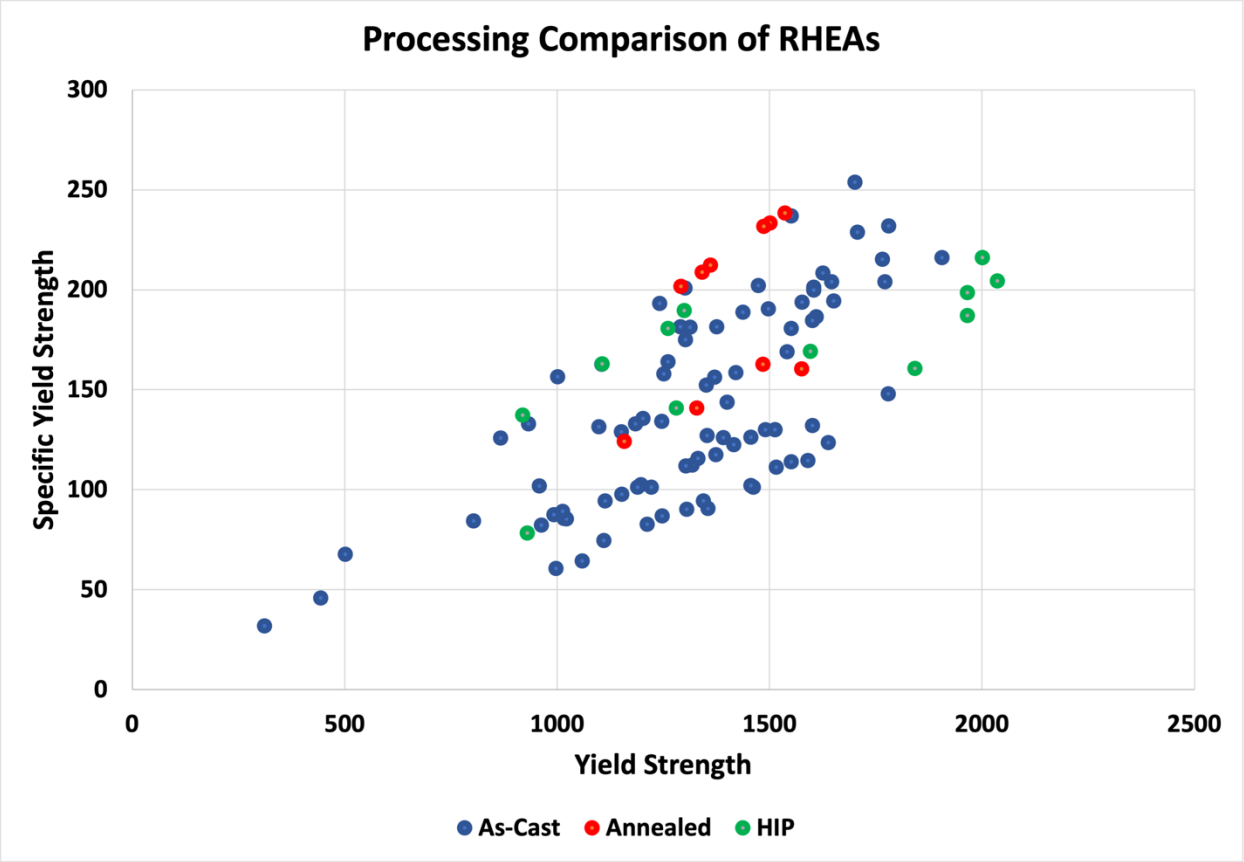


Figure 9: Chart Comparison of Processing of RHEAs

Aluminum Addition versus Specific Yield Strength

Table 10 shows the specific yield strength of RHEAs with aluminum addition along with the percent aluminum in each RHEA by mol percent. Figure 10 shows the comparison of aluminum addition versus the percent aluminum. For the trend of overall yield strength, a decrease in yield is expected with an increase in aluminum addition, but because of aluminum's low atomic weight, a trend showing a decrease in specific yield strength with an increase of aluminum addition is not seen.

Silicon Addition versus Specific Yield Strength

Table 11 shows the specific yield strength of RHEAs with silicon addition along with the percent silicon in each RHEA by mol percent. Figure 11 shows the comparison of silicon addition versus the specific yield strength. There are few data points. Hence, no real trend can be drawn from the chart, but similar to the aluminum addition, a decrease in yield strength is expected to be seen from silicon addition. The specific yield strength may have a similar trend to aluminum addition, where a decrease in specific yield strength with an increase in silicon, because of silicon's low atomic weight.

Comparison of the Number of Components

Table 12 shows the average value, standard deviation, minimum and maximum values, and range of the specific yield strength for four component RHEAs. Table 13 shows the average value, standard deviation, minimum and maximum values, and range of the specific yield strength for five component RHEAs. Finally, Table 14 presents the average value, standard deviation, minimum and maximum values, and range of the specific yield strength for the 6 component RHEAs.

Figure 12 exhibits the chart comparing the four, five, and six component RHEAs. Alloys that are lighter and stronger will be in the upper left of the chart. All three of the categories are seen across the chart, with 5 component alloys being the most numerous. The five component alloys are also the main category seen in the upper half of the chart.

Table 10: Specific Yield Strength with Percent Al Addition

Composition	Specific Yield Strength [MPa/(g/cm^3)]	Amount of Al in Mol%
$Al_{0.25}HfNbTiZr$	46.1	0.06
$Al_{0.50}HfNbTiZr$	84.6	0.11
$Al_{0.75}HfNbTiZr$	102.1	0.16
$Al_{0.25}MoNbTiV$	158.1	0.06
$Al_{0.25}NbTaTiV$	115.9	0.06
$Al_{0.2}MoTaTiV$	85.7	0.05
$Al_{0.3}HfNbTaTiZr$	101.5	0.06
$Al_{0.3}NbTa_{0.8}Ti_{1.4}V_{0.2}Zr_{1.3}$	198.8	0.06
$Al_{0.3}NbTaTi_{1.4}Zr_{1.3}$	187.3	0.06
$Al_{0.4}Hf_{0.6}NbTaTiZr$	160.9	0.08
$Al_{0.4}Hf_{0.6}NbTaTiZr$	160.9	0.10
$Al_{0.5}CrNbTi_2V_{0.5}$	208.9	0.09
$Al_{0.5}CrNbTi_2V_{0.5}$	193.3	0.11
$Al_{0.5}HfNbTaTiZr$	112.0	0.10
$Al_{0.5}MoNbTiV$	208.6	0.11
$Al_{0.5}NbTa_{0.8}Ti_{1.5}V_{0.2}Zr$	204.5	0.13
$Al_{0.5}NbTaTiV$	89.4	0.13
$Al_{0.6}MoTaTiV$	82.5	0.16
$Al_{0.75}HfNbTaTiZr$	122.8	0.27
$Al_{0.75}MoNbTiV$	164.1	0.22
$Al_{1.5}MoNbTiV$	67.8	0.18
$AlCr_{0.5}NbTiV$	201.0	0.20
$AlCr_{1.5}NbTiV$	253.9	0.17
$AlCrNbTiV$	237.1	0.20
$AlHfNbTaTiZr$	130.3	0.20
$AlHfNbTiZr$	134.3	0.20
$AlMo_{0.5}NbTa_{0.5}TiZr$	216.2	0.20
$AlMo_{0.5}NbTa_{0.5}TiZr$	216.2	0.25
$AlMo_{0.5}NbTa_{0.5}TiZr$	216.2	0.20
$AlMoNbTiV$	181.6	0.25
$AlNb_{1.5}Ta_{0.5}Ti_{1.5}Zr_{0.5}$	141.1	0.20
$AlNbTaTi$	97.9	0.24
$AlNbTaTiV$	87.7	0.24
$AlNbTiV$	156.7	0.22
$AlNbTiVZr$	233.6	0.18

Table 10 Continued

Composition	Specific Yield Strength [MPa/(g/cm^3)]	Amount of Al in Mol%
AlNbTiVZr$_{0.1}$	201.9	0.24
AlNbTiVZr$_{0.25}$	212.5	0.24
AlNbTiVZr$_{0.5}$	231.9	0.22
AlNbTiVZr$_{1.5}$	238.6	0.18

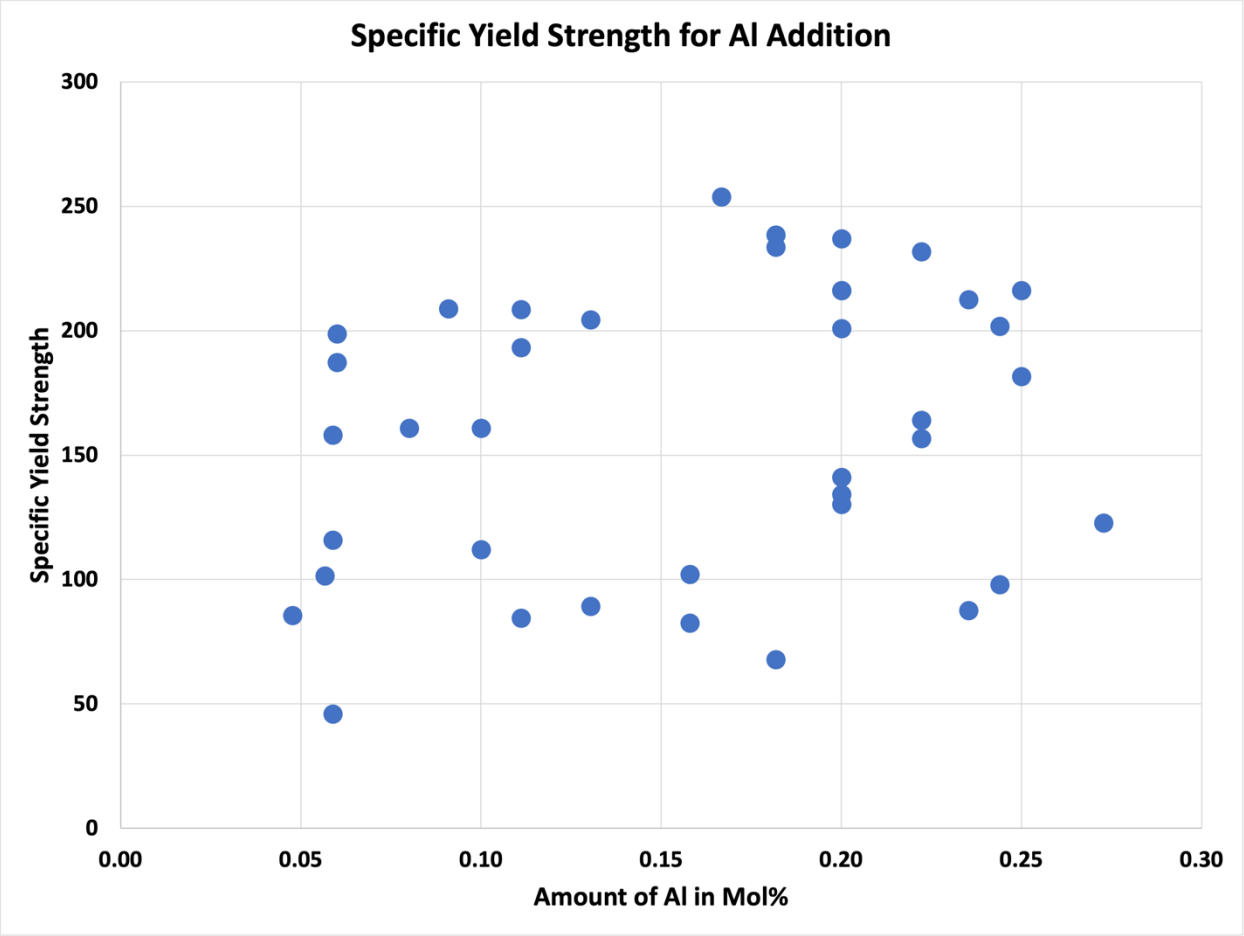


Figure 10: Al Addition [%] versus Specific Yield Strength

Table 11: Specific Yield Strength with Percent Si Addition

Composition	Specific Yield Strength (RT) [MPa/(g/cm^3)]	Percent Si in Mol %
$HfNbSi_{0.5}TiV$	152.5	0.11
$Hf_{0.5}Mo_{0.5}NbSi_{0.1}TiZr$	156.5	0.02
$Hf_{0.5}Mo_{0.5}NbSi_{0.3}TiZr$	184.7	0.07
$Hf_{0.5}Mo_{0.5}NbSi_{0.5}TiZr$	180.9	0.11
$Hf_{0.5}Mo_{0.5}NbSi_{0.7}TiZr$	194.6	0.15
$Hf_{0.5}Mo_{0.5}NbSi_{0.9}TiZr$	144.0	0.18
$HfNbSi_{0.5}TiVZr$	163.0	0.11

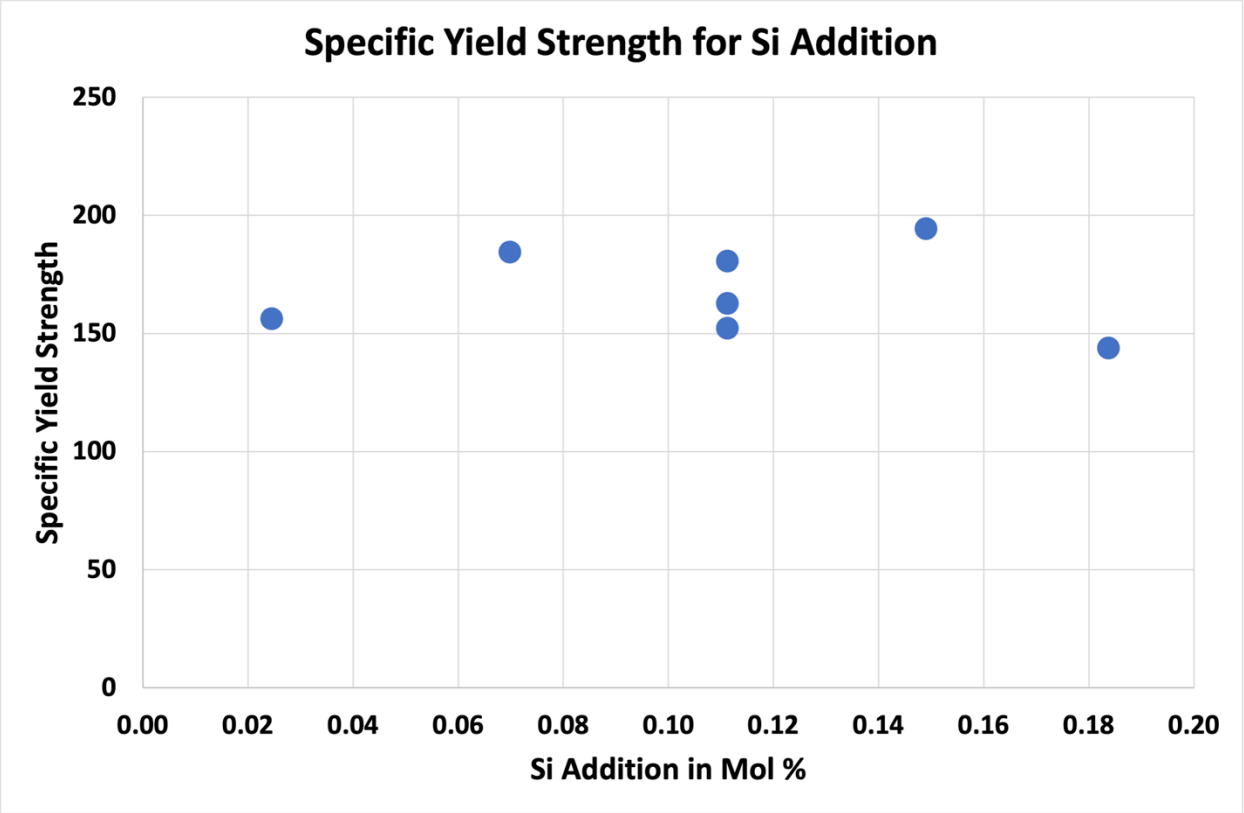


Figure 11: Si Addition [%] versus Specific Yield Strength

Table 12: Statistics on Specific Yield Strength of Four Component RHEAs

Average Yield [MPa/(g/cm^3)]:	1180.4
Standard Deviation [MPa/(g/cm^3)]:	392.15
Maximum Yield [MPa/(g/cm^3)]:	2237
Minimum Yield [MPa/(g/cm^3)]:	310
Range [MPa/(g/cm^3)]:	1927

Table 13: Statistics on Specific Yield Strength of Five Component RHEAs

Average Yield [MPa/(g/cm^3)]:	1372.68
Standard Deviation [MPa/(g/cm^3)]:	312.55
Maximum Yield [MPa/(g/cm^3)]:	2050
Minimum Yield [MPa/(g/cm^3)]:	442
Range [MPa/(g/cm^3)]:	1608

Table 14: Statistics on Specific Yield Strength of Six Component RHEAs

Average Yield [MPa/(g/cm^3)]:	1553.18
Standard Deviation [MPa/(g/cm^3)]:	274.07
Maximum Yield [MPa/(g/cm^3)]:	2035
Minimum Yield [MPa/(g/cm^3)]:	1112
Range [MPa/(g/cm^3)]:	923

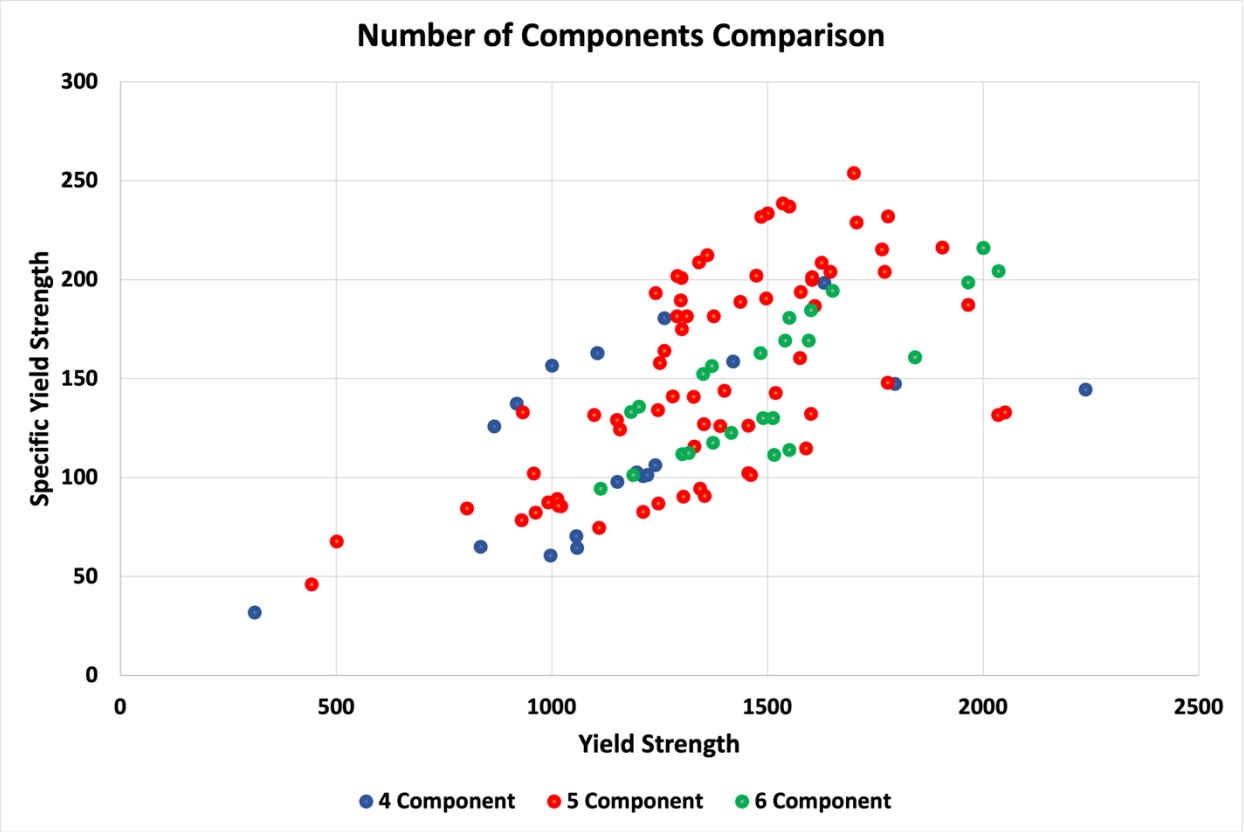


Figure 12: The Comparison of the Number of Components for RHEAs

Conclusion of RHEA Dataset

A dataset containing 115 separate compositions and 121 room temperature compression yield strengths were created from the open sources listed in references [18, 21-54]. Included in the data set are:

- Yield Strengths at Various Reported Temperatures
- Specific Yield Strength
- Percent Plasticity
- Density
- Processing
- Atomic-Size Mismatch (δ)
- Entropy of Mixing (ΔS_{mix})
- Phase
- Valence Electron Count (VEC)
- D-Parameter

These entries can be used in the design of RHEAs for further research on room and high temperature mechanical properties.

CHAPTER THREE

RHEA Mechanical Testing

Introduction

The goal of the research in the following chapters is to address the poor ductility of many RHEAs. The reason for choosing RHEAs is they have sought after mechanical properties that, if refined, can increase the capability and efficiency of modern-day materials. To select the compositions, a thorough background of mechanical properties of RHEAs was created, along with certain parameters that the specified compositions would likely be within.

Typical fabrication of HEAs follows the traditional methods of fabrication for alloys; most often including liquid melting and mechanical alloying [6]. For most scenarios requiring smaller amounts of HEAs (mechanical testing and characterization within labs) an Arc-Melter provides an efficient way to fabricate HEAs. Most notably, the melting, mixing, and casting process can be done in the same environment, without the need to change machines or exchange the sample.

Once samples were cut and machined to the specified standards, with the help of Doug Fielden on the cutting of the tension samples, the following mechanical tests were performed. Due to the difficulty in casting of the RHEAs, only one successful run was performed for each composition. A successful run was considered as a mechanical test in which the sample did not fail due to casting defections.

Selection of RHEA compositions

In the design of RHEAs, there is an area in the phase diagram of RHEAs where BCC-structured RHEAs could have strength and ductility [14]. Calculating the Gibbs Free Energy (ΔG) shows for certain compositions that a phase other than Body-Centered Cubic (BCC) is more stable at lower temperatures and introduces the possibility of the Transformation Induced Plasticity (TRIP) effect at low temperatures.

A collaborator on the project, Prof. Eric Lass from the University of Tennessee, Knoxville (UTK), has calculated some of the Gibbs free energy of transformation from the body-centered cubic (BCC) to the hexagonal close-packed (HCP) crystal structure, where $HfTa_{0.5}TiZr$ and $HfNb_{0.5}Ta_{0.5}TiZr$ have $\Delta G^{BCC\text{-}HCP}$ of – 2150 J/mol and – 353 J/mol at 0 K, respectively. Although these energies are shown at 0 K, they show a likelihood of phase transformations occurring at room temperature.

The complete set of alloys was chosen as HfNbTiZr, HfNbTaTiZr, $HfTa_{0.5}TiZr$, $HfNb_{0.5}Ta_{0.5}TiZr$, $HfNbTa_{0.5}TiZr$, $Hf_{0.5}NbTa_{0.5}TiZr$, and $NbTa_{0.5}TiZr$. The equimolar HfNbTaTiZr alloy, also known as the Senkov alloy, has been thoroughly studied, and is a known single-phase BCC alloy that is included as a comparison to the other compositions [19, 20].

Although some work has been done to enhance the ductility of RHEAs through solid solution strengthening, composition tuning, and/or grain refinement [21-27], this research was focused on the mechanical properties of the as-cast compositions to provide a foundational study on the deformation mechanisms of RHEAs.

Weighing of Elemental Compositions for Fabrication

For each composition a purity of the metals of 99.98% or higher was used. To find the amount of each element needed the equations shown below were used where c_i is the number of moles and mw is the molar weight of the element.

$$Mass\ Required = Mass\ of\ Cast \times Mass\ Percent$$

$$Mass\ Percent = \frac{c_i \times mw}{Total\ Mass\ of\ Alloy}$$

Since the size of the cast varies depending on the sample needed, to save material, the amount of mass required was calculated using the density of the alloy and the volume of the cast. Shown below is the calculation for the density of the alloy.

$$\rho_{alloy} = \sum_{i=1}^{n} \frac{c_i \times \rho_i}{Total\ Mass}$$

An additional mass of roughly 10% of the mass required for the cast is added to make sure the final cast has more than enough material for a successful cast.

Arc-Melting

The arc-melters used for the fabrication of the RHEAs tested all use a vacuum vessel to remove any atmosphere, and then replace the vacuum with a small amount of Argon to prevent any oxidation from trace amounts of gas left in the chamber. A titanium button is melted prior to the melting, mixing, and casting of any samples to act as an oxygen sink, removing any amount of oxygen in the chamber.

Within the chamber, the mold and base of the molds are made of water-cooled copper, to prevent the melting of the base and the mold. The arc is generated by a current traveling through a tungsten electrode within the chamber. The arc-melting process can be thought of as a Tungsten Inert Gas (TIG) welding process. Instead of joining two or more large pieces of metal together, the arc generated by the tungsten electrode is used to melt and mix two or more elements.

The HEA button created can then be placed above the mold to be cast. The arc-melters use a vacuum below the mold to pull the melted HEA into the mold. The user of the arc-melters will open a valve below the mold allowing the vacuum to occur once the HEA button is thoroughly melted. The vacuum is used because the quick cooling of the HEAs makes the force of gravity alone too weak to cast the samples before they are re-solidified.

Arc-Melting Standard Operating Procedures

Introduction

Before the compositions were cast, a written standard operating procedure (SOP) had not been established for safe lab practices. To ensure the safety of the lab and team members, an SOP was written for both arc-melters named "'Old' Arc-melter" and "'New' Arc-melter".

"Old" Arc-Melter Startup

1. Open both Argon tanks that are connected to the equipment as shown in Figure 13.
2. Turn on the breaker labeled "MRF ARC FURNACE" as shown in Figure 14.
3. Turn on the water starting at the bottom forward handle and working up and out in the same motion for all 6 handles as shown in Figure 15.
4. Check the second (back) pressure gauge shown in Figure 16. To open the chamber, it needs to be at 0. If not at 0, back fill with Argon to open the chamber.
5. Raise the chamber.
6. Take out the mold using screws, shown in Figure 17 that can be found on the red toolbox, to ensure it is clean.
7. If clean, lower the correct mold into the holder using the screws.
8. Place sample slightly covering mold, but not over screw holes as shown in Figure 18.
9. Close the chamber and push the lid towards the left for a better seal.



Figure 13: Argon Tanks



Figure 14: Furnace Breaker

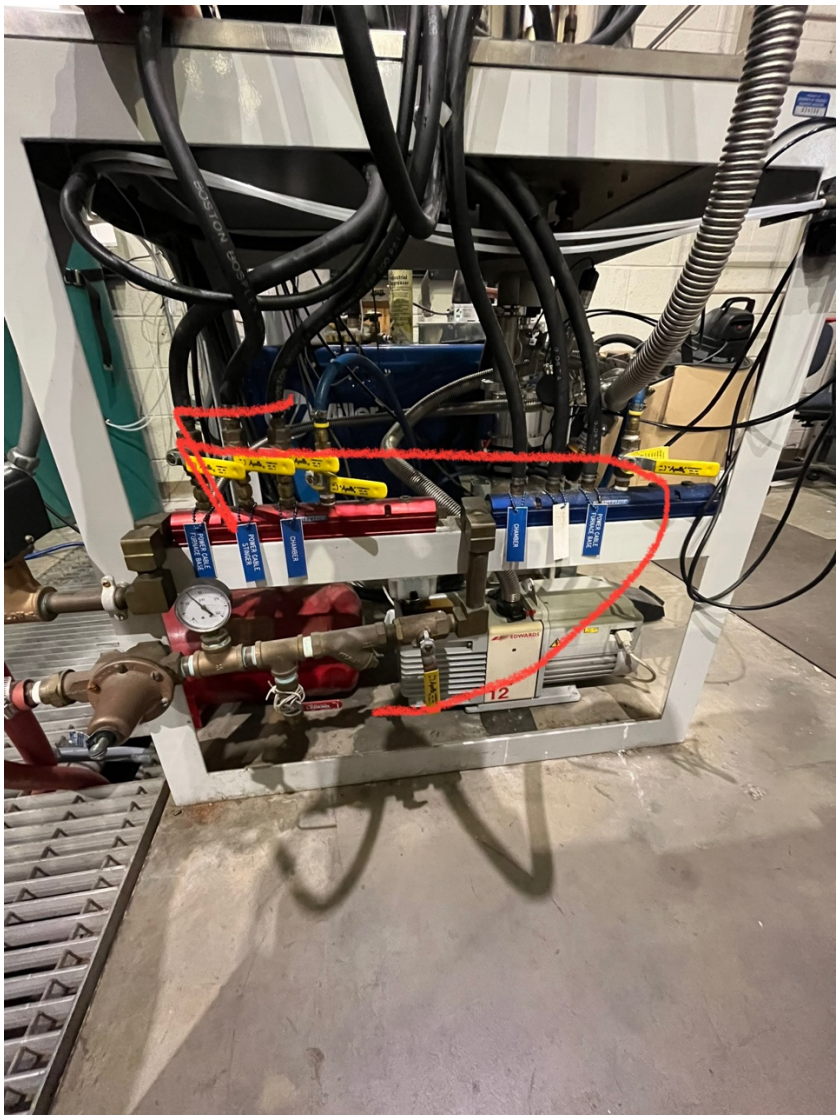


Figure 15: Water Valves

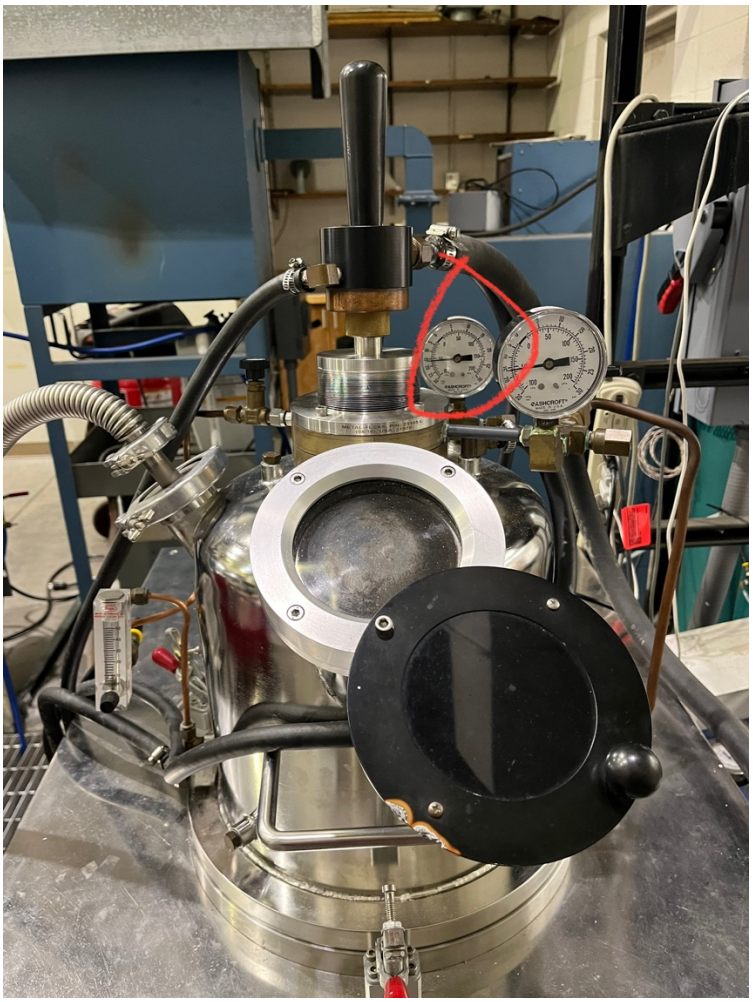


Figure 16: Pressure Dial



Figure 17: Copper Mold



Figure 18: Casting Setup

10. Turn on the mechanic pump (lower left switch with cover) shown in Figure 19.
11. Open the left light switch followed by the right in Figure 20.
12. Open the "Varian Dial" below the chamber shown in Figure 21 (Should see negative values on the gauge).
13. Wait for the electronic display to show 50-150 torr shown in Figure 22.
14. Quickly close the right light switch, close the "Varian Dial", and open the Argon using the left knob shown in Figure 23 until -50 KPa is reached.
15. Close the Argon and close the left switch.
16. Turn on the Auxiliary power for the generator using the switch shown in Figure 24.
17. Turn on the lamp at the back of chamber shown in Figure 25.
18. Set the generator to ~400 Amps using the knob shown in Figure 26 to melt the titanium button as an oxygen sponge.
19. Melt the titanium sponge.
20. Check the titanium button for oxidation, if little to no oxidation, then continue. An example of heavy oxidation is shown in Figure 27.
21. Set generator to the desired amperage. For refractory metals a higher amperage may be needed. Ask the lab supervisor for a likely starting amperage.
22. Cast/Melt sample. If casting, open the right light switch simultaneously to melt the sample.
23. Close the right light switch after casting the sample.
24. Turn off Auxiliary power and wait ~10 minutes to cool.
25. Backfill with Argon to reach atmospheric pressure and open chamber.

"Old" Arc-Melter Shutdown

1. Take out the mold as before and clean it using the emulsifier. Rinse the mold with ethanol and wipe it down.
2. Place the mold back in the chamber.
3. Close the chamber.
4. Open the light switches, left then right.
5. Open the Varian Dial.
6. Make the chamber a vacuum around -50 KPa.

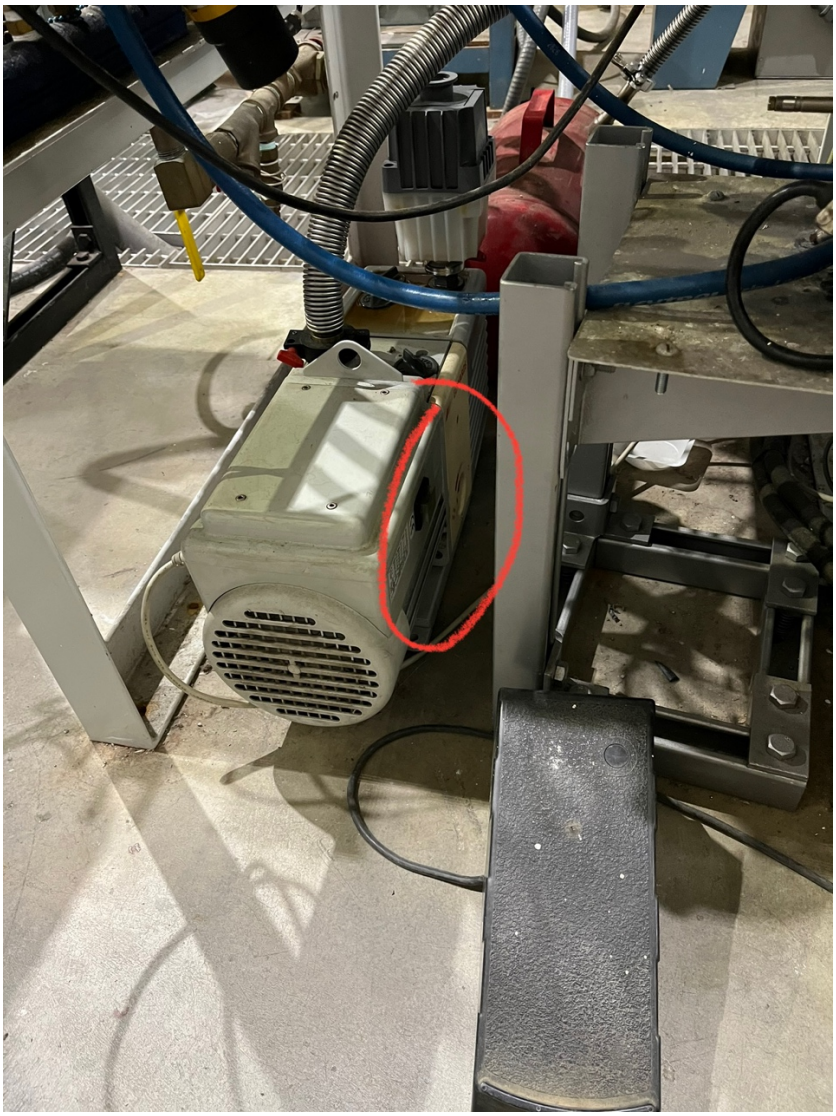


Figure 19: Mechanical Vacuum Switch

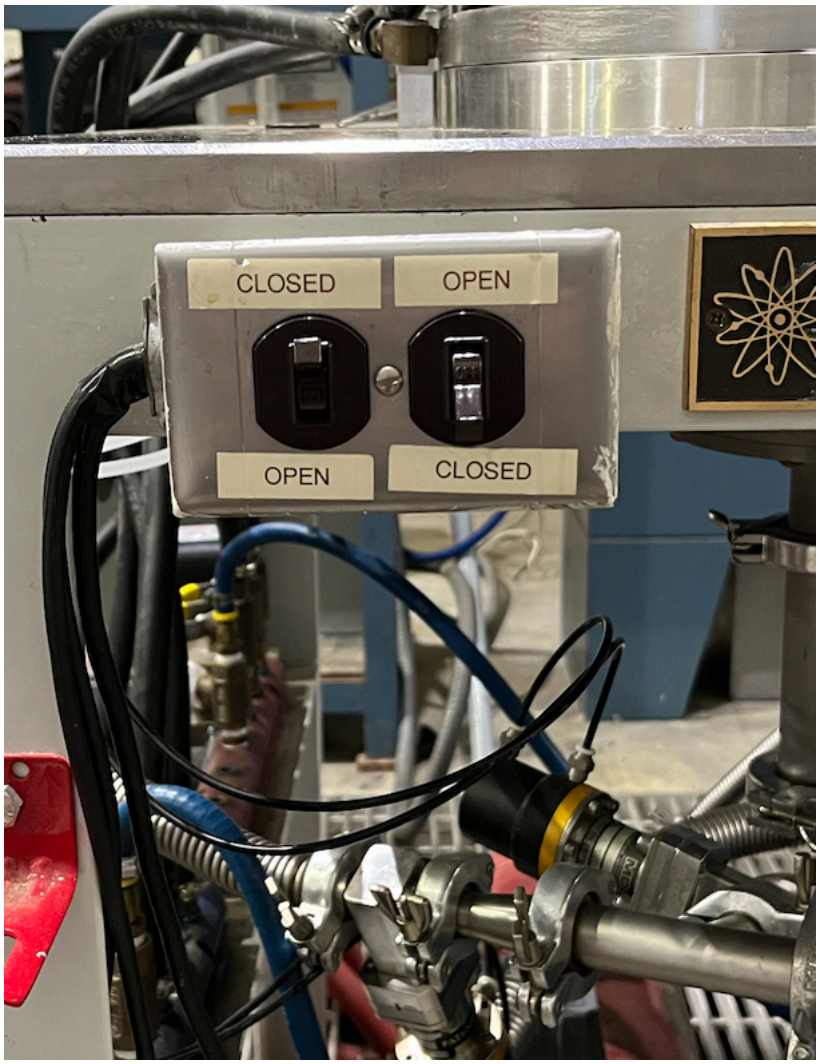


Figure 20: Valve Switches

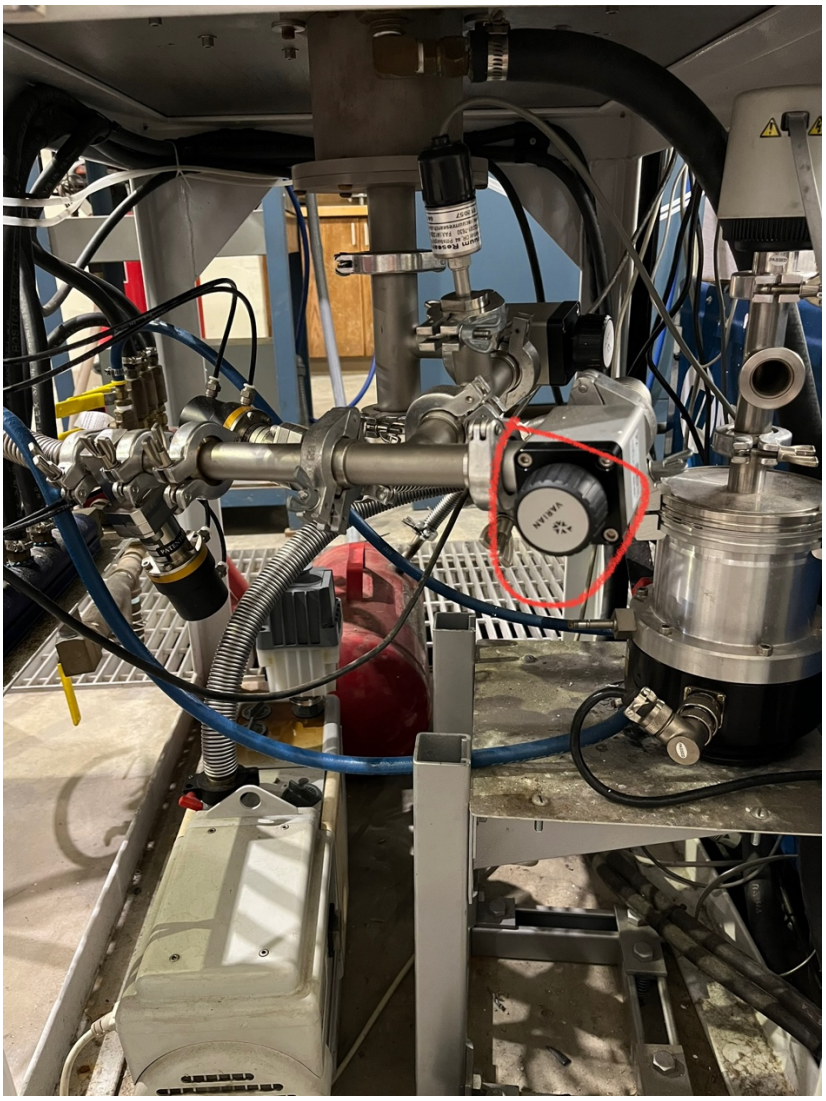


Figure 21: Varian Dial



Figure 22: Pressure Display



Figure 23: Argon Valve

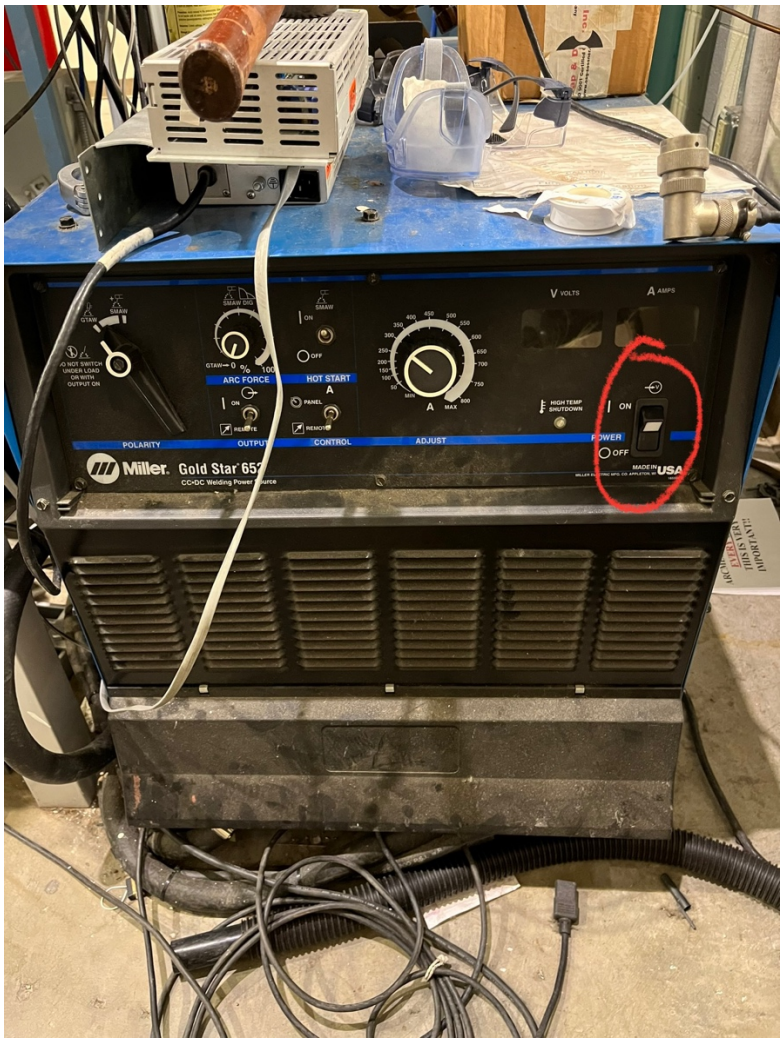


Figure 24: Auxiliary Power Switch

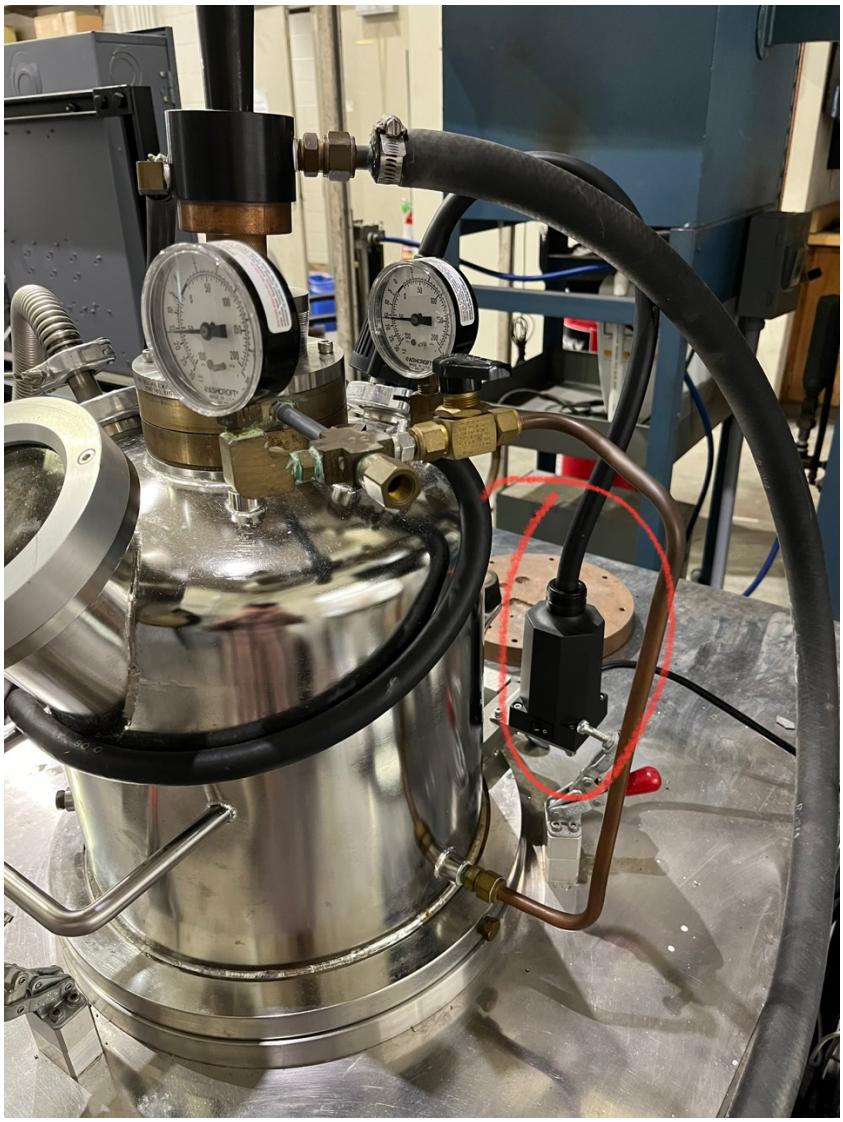


Figure 25: Lamp Switch

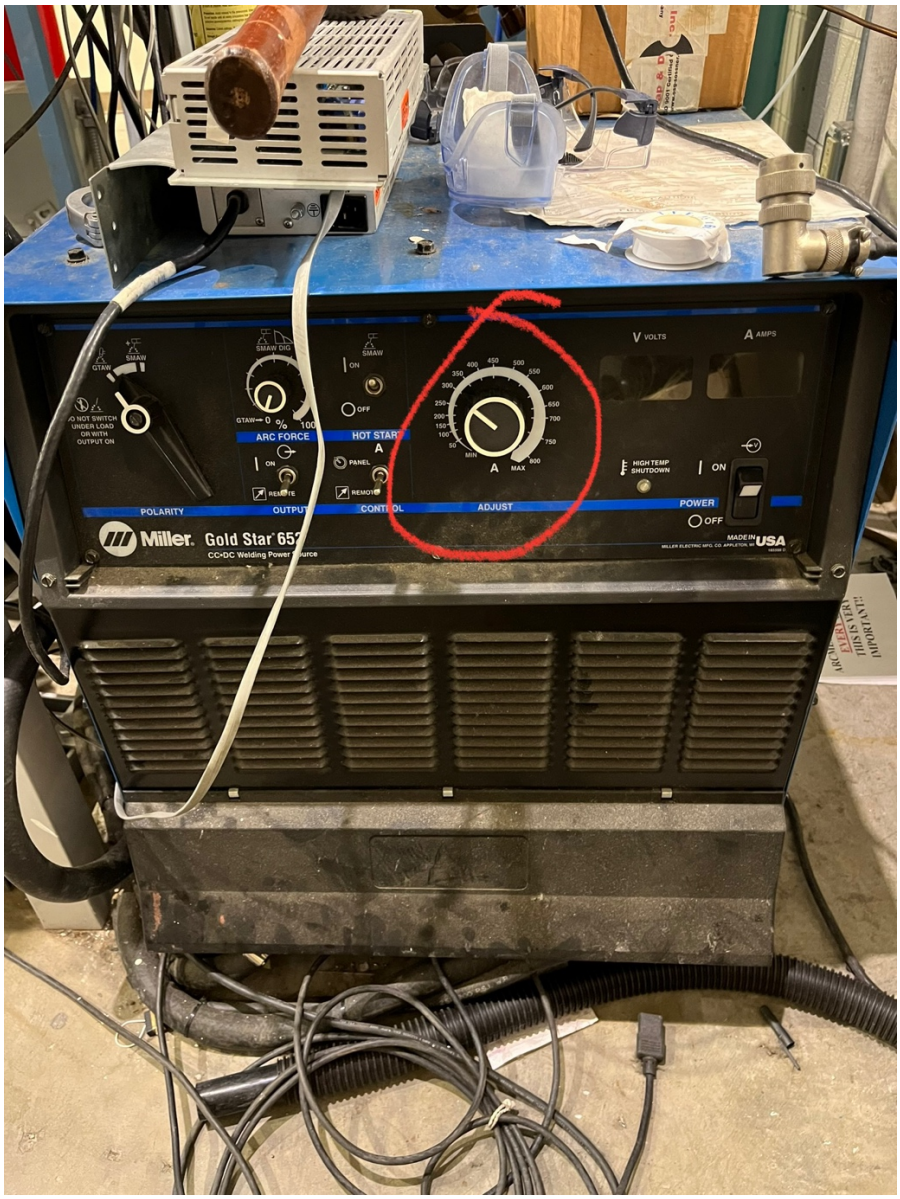


Figure 26: Amperage Dial

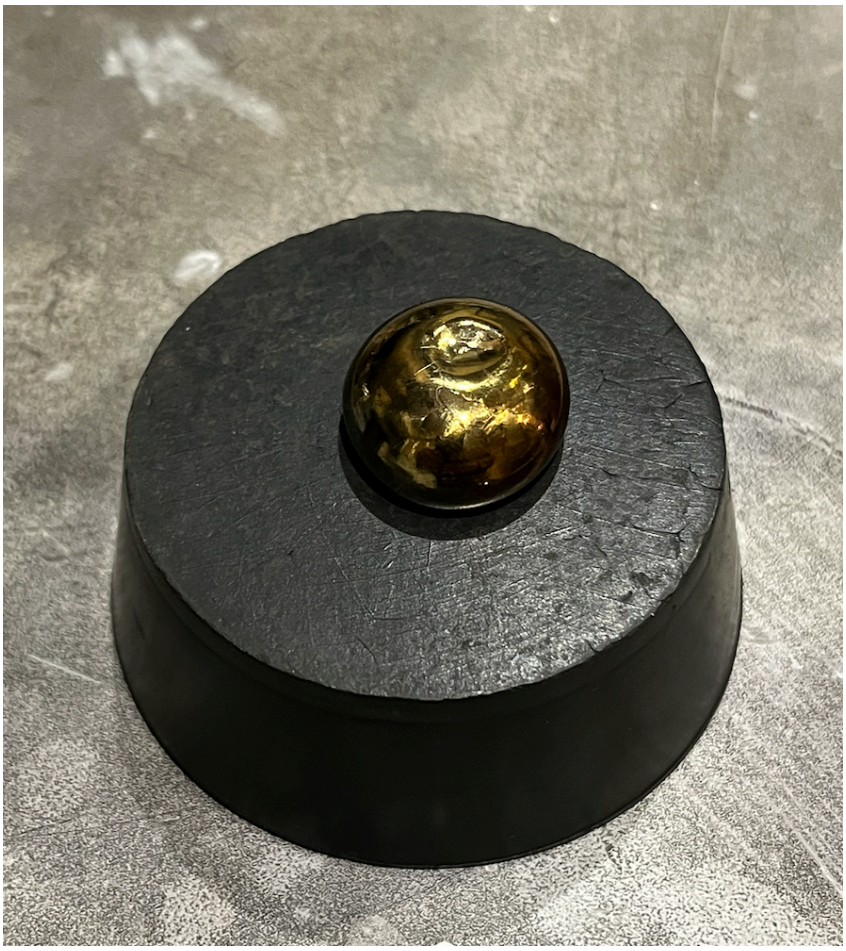


Figure 27: Oxidized Titanium

7. Once the vacuum has reached -50 KPa, close the light switches, right then left, and close the Varian Dial.
8. Turn off mechanical vacuum pump.
9. Turn off the water in the opposite order of turning it on.

"New" Arc-Melter Startup

1. Open V3 to release pressure shown in Figure 28. Watch the gauge above the valve V3 to see it return to atmospheric pressure.
2. Once pressure is stable, close V3.
3. Lift chamber by turning knob to up position and pumping the lever to lift the chamber as shown in Figure 29.
4. Insert mold or crucible in chamber if needed, and make sure mold is flush when inserted.
5. Below the chamber, rotate the bottom handle shown in Figure 30 to the full down position.
6. Insert the mold or crucible and rotate bottom handle slightly up until resistance is felt to remove air.
7. Pour weighed alloy composition into the crucible or place button on mold.
8. Lower the chamber by turning the knob to the "down" position and gently pulling on lever.
9. Turn "Rotary Vane Pump" to on position as shown in Figure 31.
10. Rotate V2 CCW till handle is straight down as shown in Figure 32. Vacuum should begin and pressure should decrease.
11. Open V22 and V23 (red handle) Counter-Clockwise shown in Figure 33 and Figure 34 (If only melting samples and not casting, omit this step along with closing the valves in step 17.)
12. Turn main switch (Hauptschelter) to on as shown in Figure 35.
13. Turn "Diffusions/Turbopump" to on position as shown in Figure 36.
14. Wait for pressure to read below 5.5×10^{-2} Barr.
    a. While waiting, turn on main circuit breaker behind arc-melter as shown in Figure 37.
    b. Turn on the water system, in flow to out flow.
        i. In red, out green as shown in Figure 38.

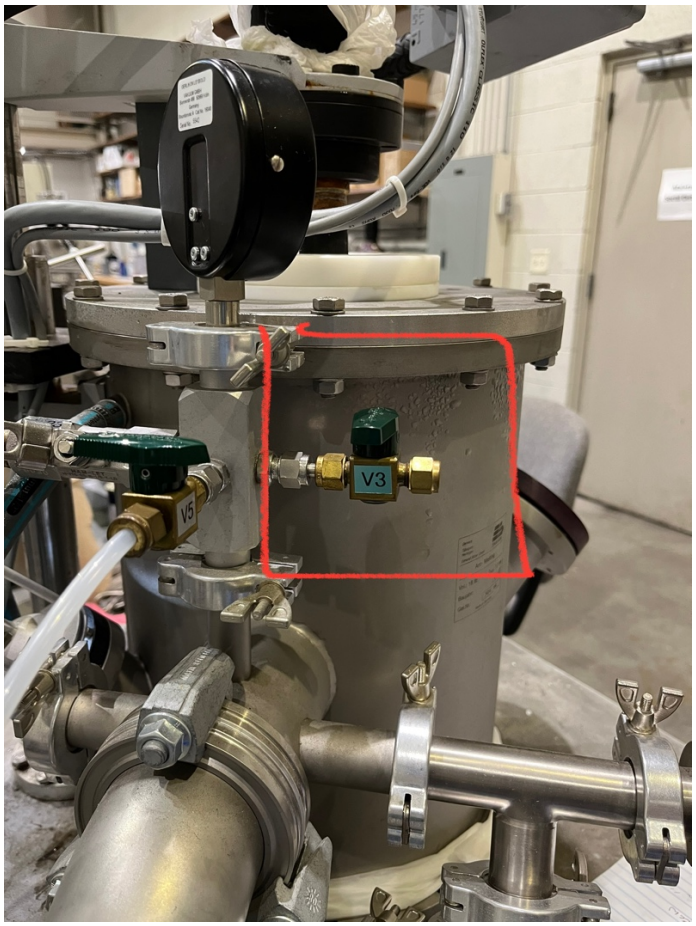


Figure 28: Chamber Valve



Figure 29: Chamber Lift

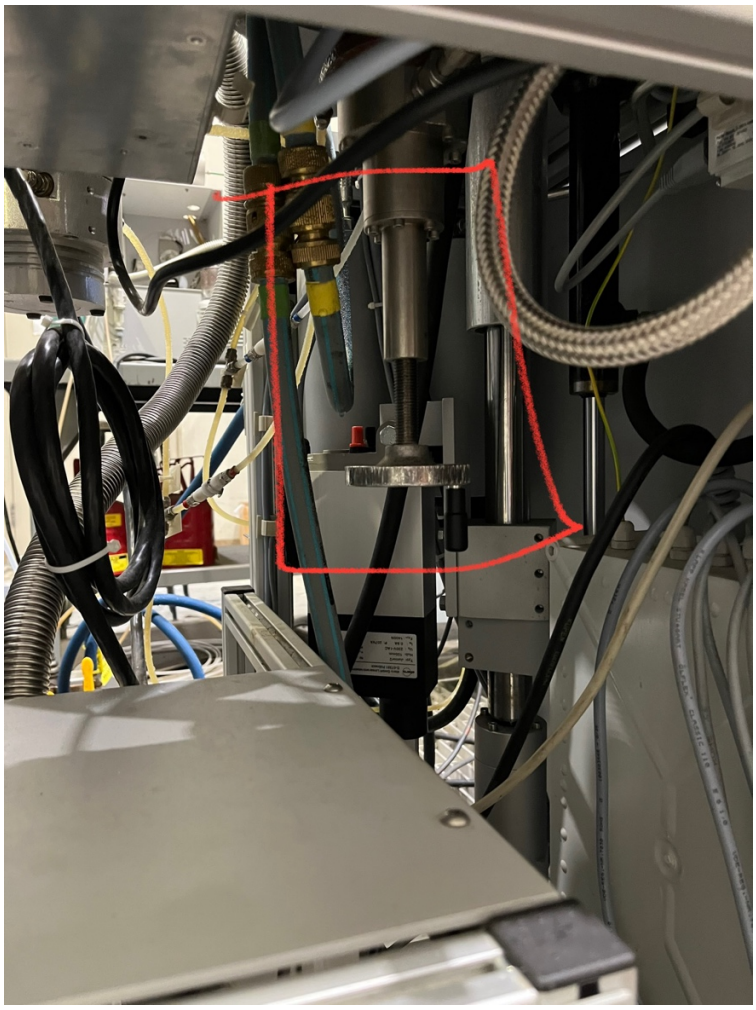


Figure 30: Mold or Crucible Lift Handle



Figure 31: Rotary Vane Pump Switch

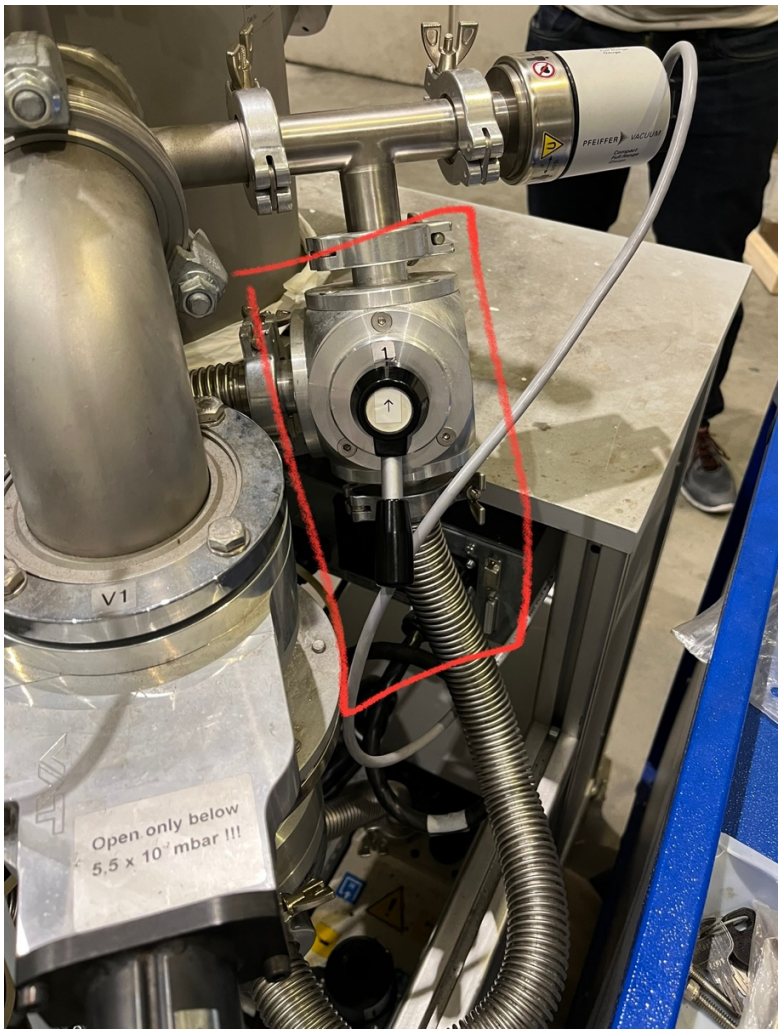


Figure 32: Vacuum Valve

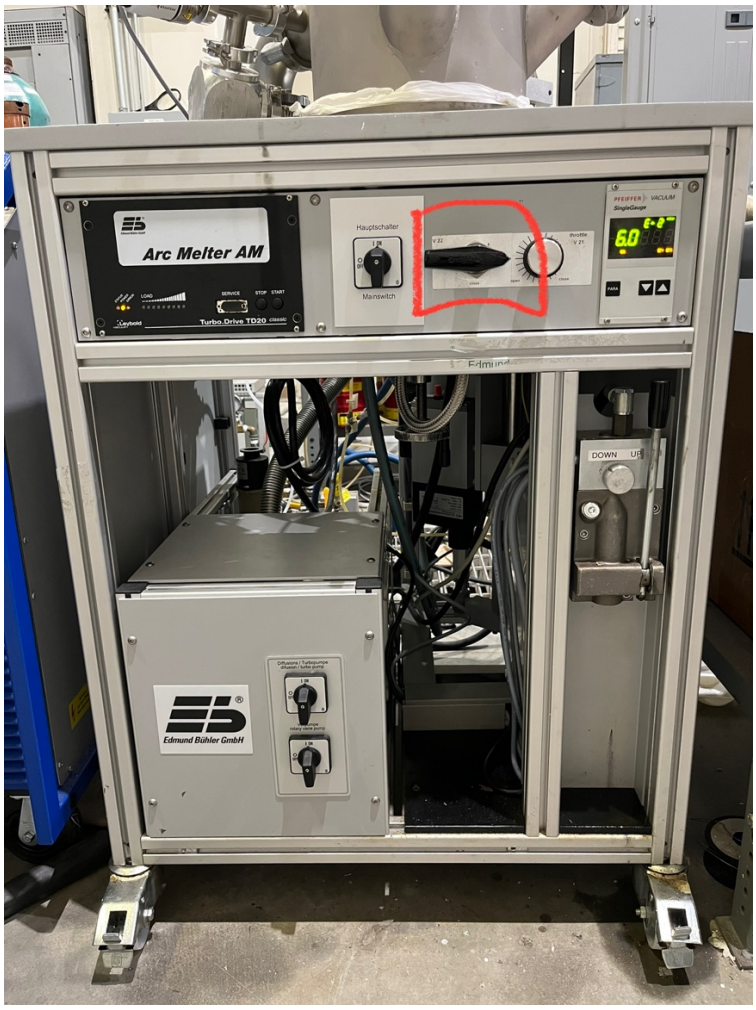


Figure 33: Casting Vacuum Valve

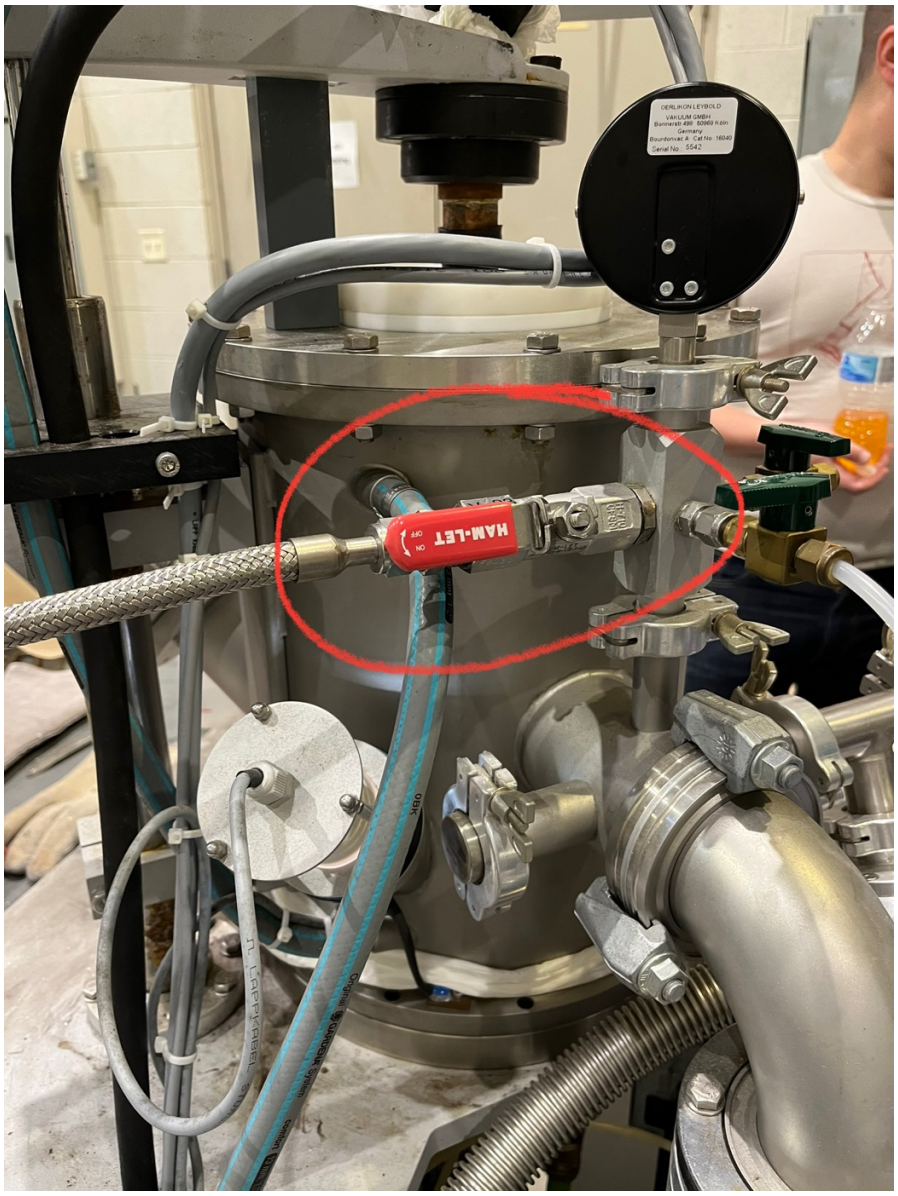


Figure 34: Casting Vacuum Valve 2



Figure 35: Main Switch



Figure 36: Diffusion Pump Switch



Figure 37: “New” Arc-melter Breaker



Figure 38: Water Valves for Filtration

   ii. Then, in orange, out yellow as shown in Figure 39.

c. Turn on gas shown in Figure 40 (if pressure does not change from 0 on tank, replace tank).

15. After pressure is below $5.5x10^{-2}$ Barr, close V2 (handle should be straight up).
16. Open V1 (bolt action) shown in Figure 41 and start turbo drive (TD20) by pressing start button as shown in Figure 42.
17. Wait for $2.0x10^{-5}$ m Barr, then close V22 and V23 (If casting).
18. Close V1 and click the stop button on the turbo drive.
19. **Immediately** following step 18, open V5 to 600 m Barr as shown in Figure 43.
20. Walk to the back of the power generator and turn red knob to on position as shown in Figure 44.
21. Using the control knob on front of the welder shown in Figure 45, turn to the % tab, and push the knob in to select it.
22. Turn the amperage percentage to 80-85% for the first melt.
23. On the arc melting T-bar handle, hit the cancel/reset malfunctions button shown in Figure 46. If both adjacent red lights go out, continue. If not, troubleshoot the issue.
24. Position the tungsten electrode roughly 2-3 mm from the copper base as shown in Figure 47.
25. Close the UV shield on the chamber as shown in Figure 48 and turn on the arc-melter.
26. Melt the Titanium first to check for Oxygen contamination.
27. If there is no contamination, continue to the sample.
28. Melt sample 5 times, flipping each time.
29. To remove the sample, turn off power generator.
30. Open V3 to atmospheric pressure.
31. Close V3.
32. Turn knob to up position for the chamber and use the lever to move the chamber upwards.

"New" Arc-Melter Shutdown

1. Lower arc melting chamber and check to see V3 is closed.
2. Open V2 handle and wait until pressure is $1.5x10^{-1}$ millitorr.
3. Close V2.

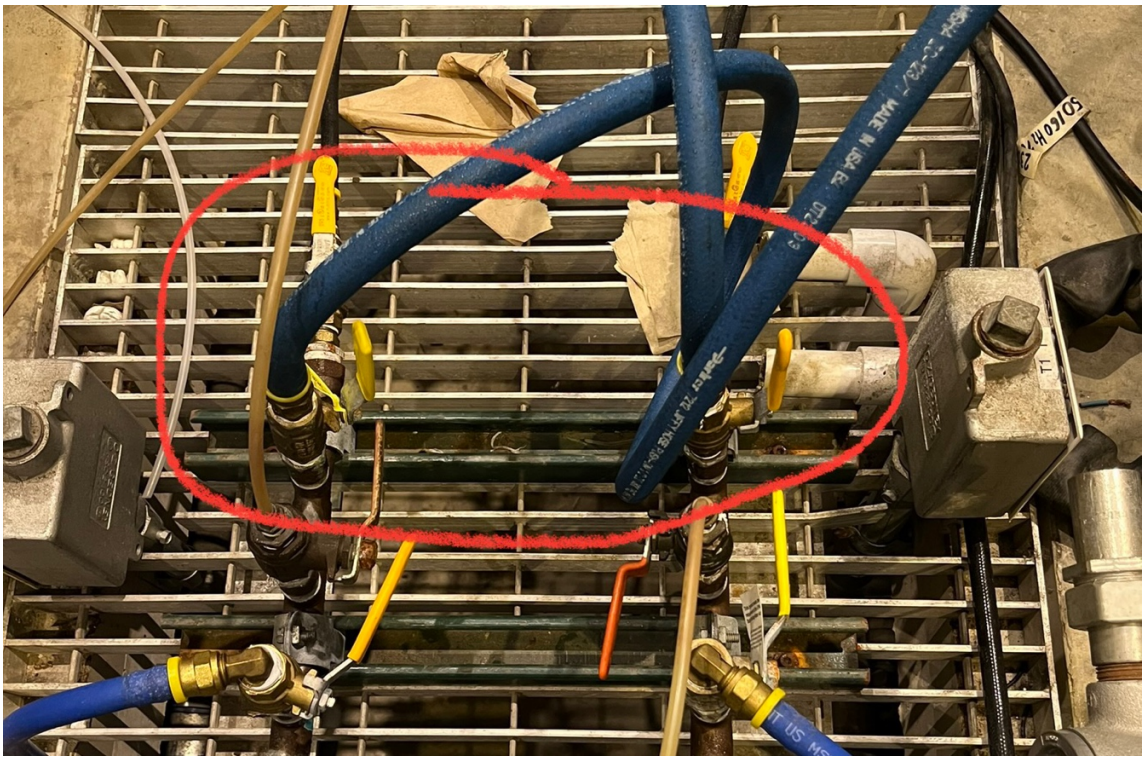


Figure 39: Water Valves



Figure 40: Argon Tank

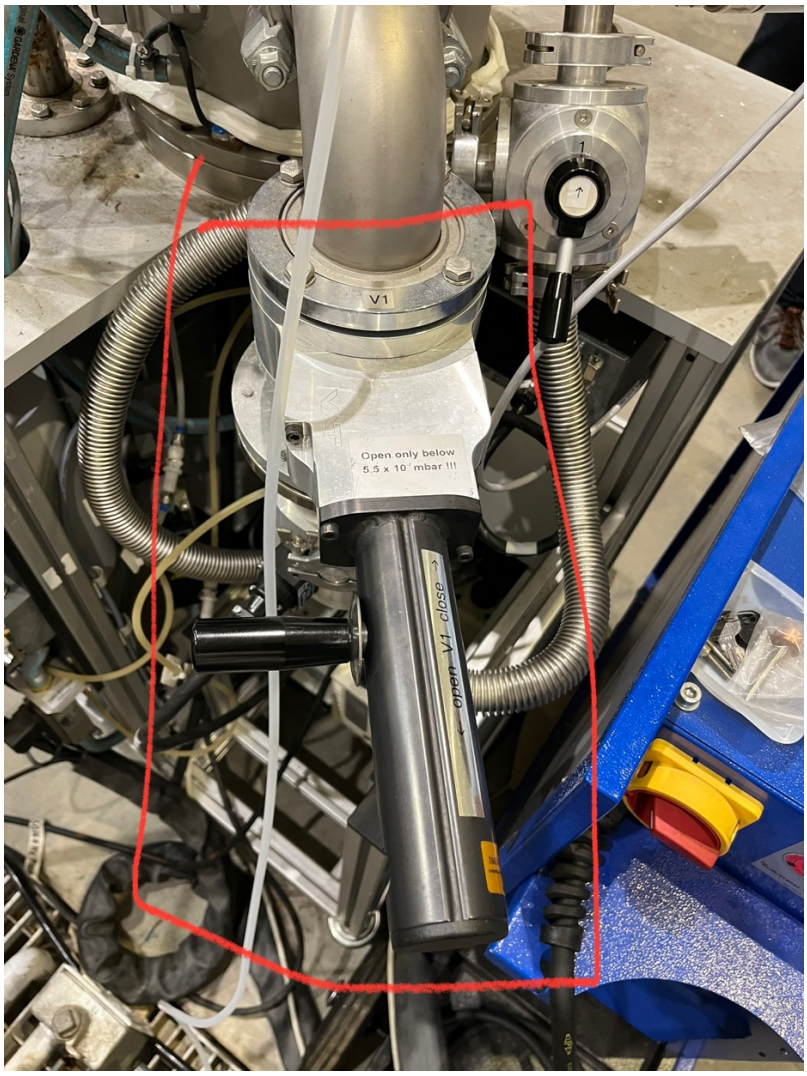


Figure 41: Diffusion Pump Valve



Figure 42: Turbo-Pump Button

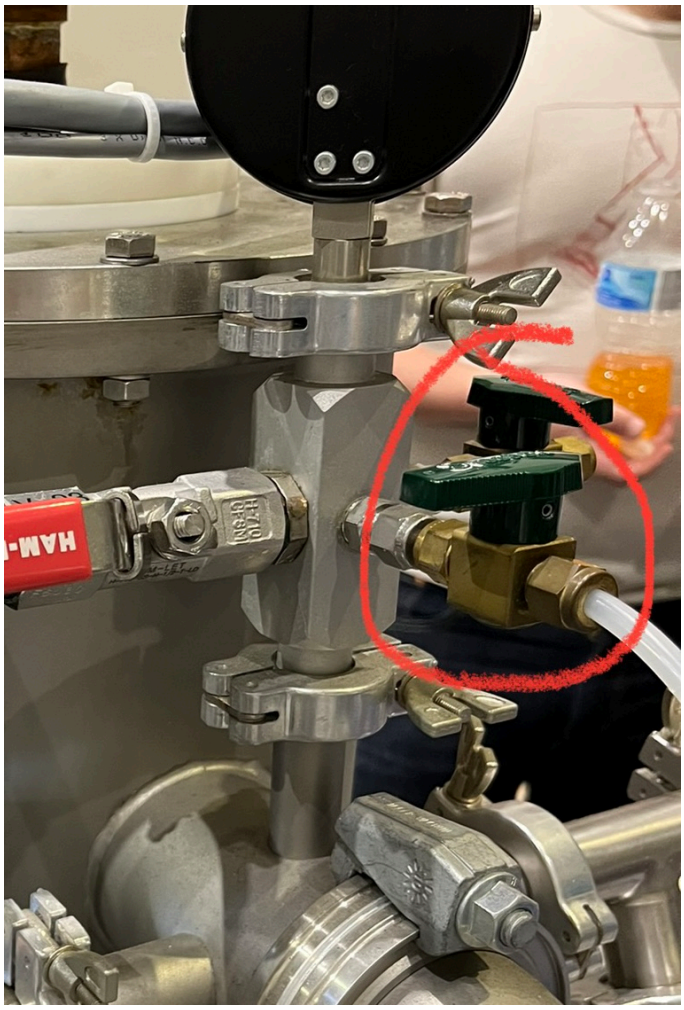


Figure 43: Argon Valve



Figure 44: Auxiliary Power Switch



Figure 45: Generator Knob



Figure 46: Reset Button

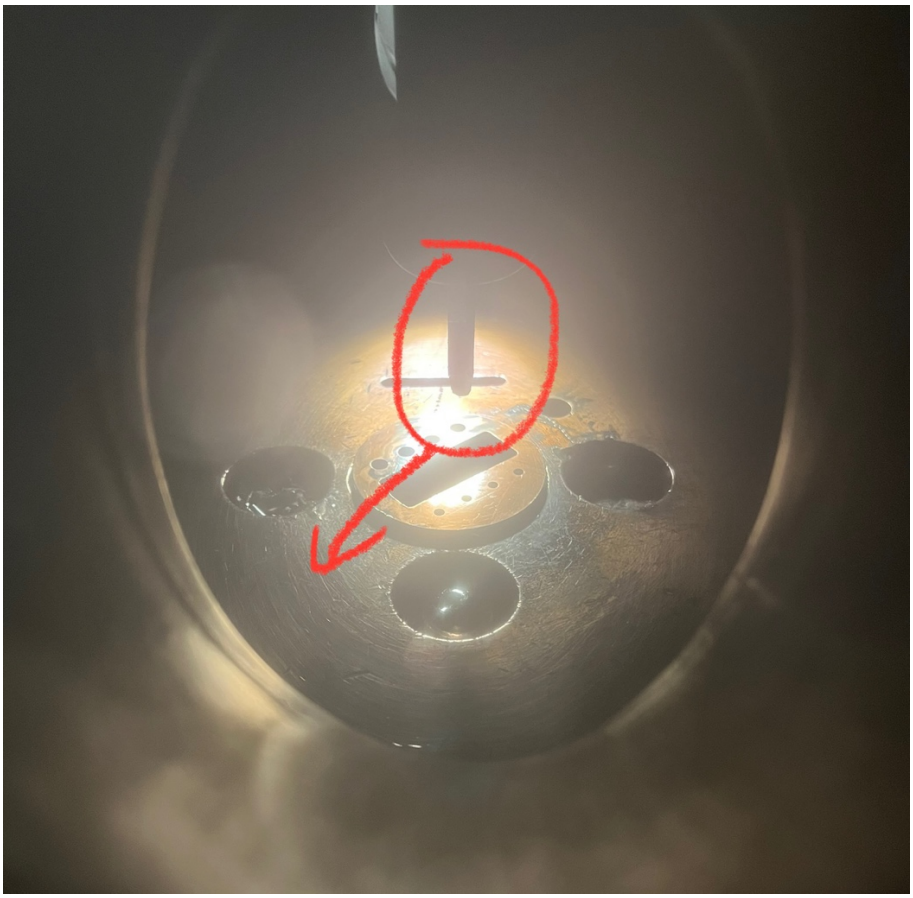


Figure 47: Tungsten Electrode



Figure 48: Arc Shield

4. Check TD20 has no green lights (If yes to green lights, hit stop and wait for all green lights to go away).
5. Turn off Turbo pump/Diffusion and Rotary Vane pump.
6. Turn off the main switch (Hauptschelter).
7. Turn off the main electrical.
8. Turn off water (in the order of out flow to in flow: yellow, orange, green, red).
9. Turn off gas.

Compression Samples

The compression samples for the Material Testing Systems (MTS) at UTK were cast as 4 mm diameter rods that were then cut to length to satisfy the American Society of Testing of Materials (ASTM E9) standard: $1.5d \leq L \leq 2.0d$, where L is length in millimeters and d is diameter in millimeters.

The compression samples used for testing at the Spallation Neutron Source at Oak Ridge National Lab (SNS at ORNL) were cast and then cut to the following dimensions provided in the Figure 49 by SNS at ORNL.

Tension Samples

Tension samples for the MTS systems at UTK were cast as 12 mm width by 3 mm thickness plates with varying lengths. They were cut using electrical discharge machining (EDM) into a "dog-bone" shape with the dimensions shown in Figure 50 from the required dimension for tensile testing at the SNS at ORNL.

Difficulty in Casting and Fabrication

Due to the high melting temperature of many of the refractory components of RHEAs, a successful cast was not always accomplished. By varying the current of the arc-melters, some of the difficulty in casting was overcome, but not all the issues of casting were addressed. The success rate for rod shaped casts was much higher than that of the plate casts, with a successful cast occurring roughly 50% for the rod cast, and a success rate of roughly 20% for the plate cast. The time expended to obtain a successful compression rod on average is 5 hours. The time

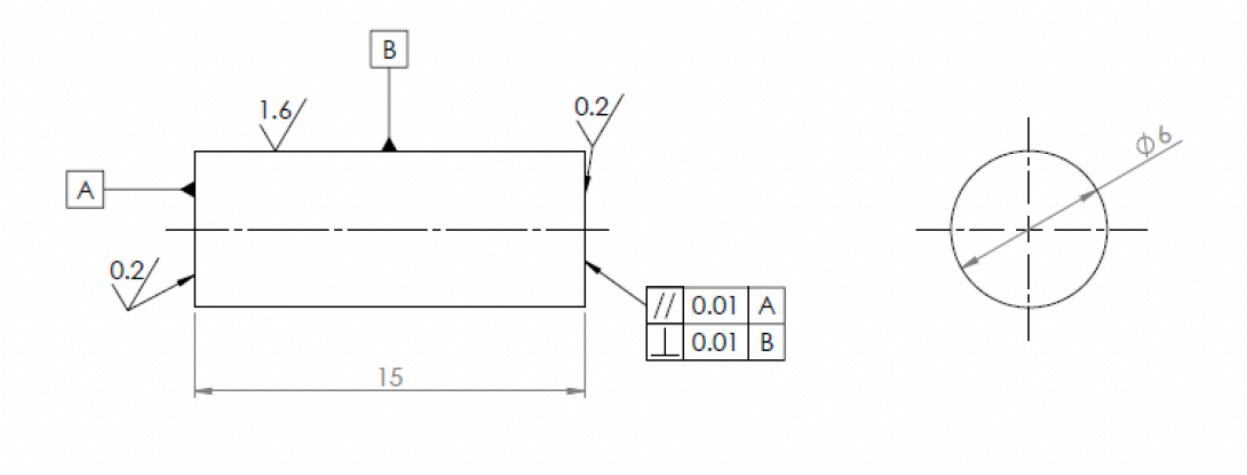


Figure 49: Compression Rod

The dimensions of the compression rod in millimeters fabricated for testing at ORNL.

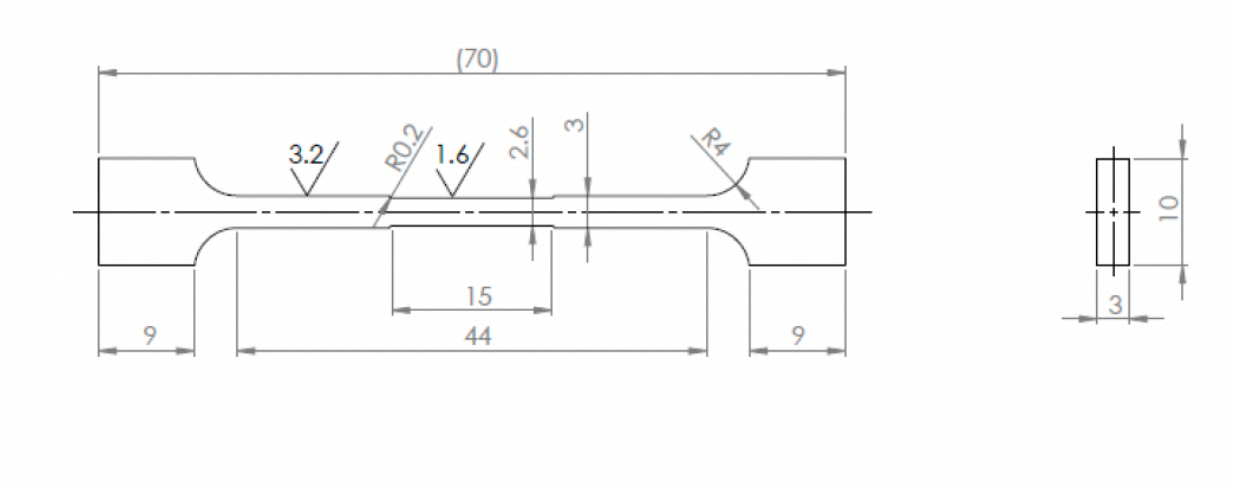


Figure 50: Tension Plate

The dimensions of the tension samples in millimeters used for tensile testing at the SNS at ORNL.

expended to obtain a successful tension plate is 12 hours, before the using EBD to cut the plates into a "dog-bone" shape.

Compression Testing

Each sample was run at a strain rate of $10^{-3}s^{-1}$ at room temperature. The compression samples were run using a Material Testing System 810 from MTS Systems Corporation at UTK. The yield strength and failure strength for each composition is shown in Table 15. The stress strain curves for the compression tests are shown in Figure 51. While performing the tests, it was noted that none of the compositions failed catastrophically like other RHEAs that had been tested in the same manner.

Tension Testing

Each sample was run at a strain rate of $5 \times 10^{-5}s^{-1}$ at room temperature. The tension samples were run at the VULCAN beamline at the Spallation Neutron Source (SNS) at ORNL. Due to difficulty of casting for the size of the cast needed for tension sample, only five out of seven compositions were successfully cast for tension testing. Of the five that were cast, only four provided sufficient tension samples that did not fail prematurely. Because of the cost and time associated with casting these larger samples, the mechanical data was obtained at ORNL and has not been replicated at UTK. The mechanical testing results are shown with the yield strength shown in Table 15 and the stress strain curve shown in **Figure 52**. The neutron diffraction results are discussed in a later chapter.

Results and Discussion

Casting and machining continue to be a limiting factor for studies on RHEAs with just four out of seven successful tension plates made. Three out of the four tension samples do not show increased ductility, but in both tension and compression data, $HfTa_{0.5}TiZr$ showed high levels of plasticity and ductility at room temperature. This composition also has the highest ultimate strength of any of the compositions tested. To find the deformation mechanism(s) for the seven RHEAs, XRDs of pre- and post-compression samples were obtained and are shown in the

Table 15: Properties and Yield of Reported RHEAs

	HfNbTiZr	HfNbTaTiZr	$HfTa_{0.5}TiZr$	$HfNb_{0.5}Ta_{0.5}TiZr$	$HfNbTa_{0.5}TiZr$	$Hf_{0.5}NbTa_{0.5}TiZr$	$NbTa_{0.5}TiZr$
Atomic Size Mismatch (δ) [%]	4.261	4.267	4.216	4.398	4.324	4.251	4.130
Entropy of Mixing	11.526	13.381	11.239	12.967	13.146	12.967	11.239
VEC	4.25	4.4	4.147	4.25	4.329	4.375	4.433
Density [g/cm^3]	9.700	11.826	11.498	11.199	10.955	10.445	9.651
D-Parameter	4.509	3.788	4.106	4.074	4.044	3.922	3.719
Yield Strength Com-pression [75]	738	839	1016	865	771	842	847
Ultimate Strength (Com-pression) [75]	1114	1255	1607	1390	1198	1231	1265
Specific Yield Strength Com-pression [75]	76.1	70.9	88.4	77.2	70.4	80.6	87.8
Yield Strength Tension [75]	-	-	276	719	786	664	-
Ultimate Tensile Strength [75]	-	-	1032	871	958	733	-
Specific Yield Strength Tension [75]	-	-	24.0	64.2	71.7	63.6	-

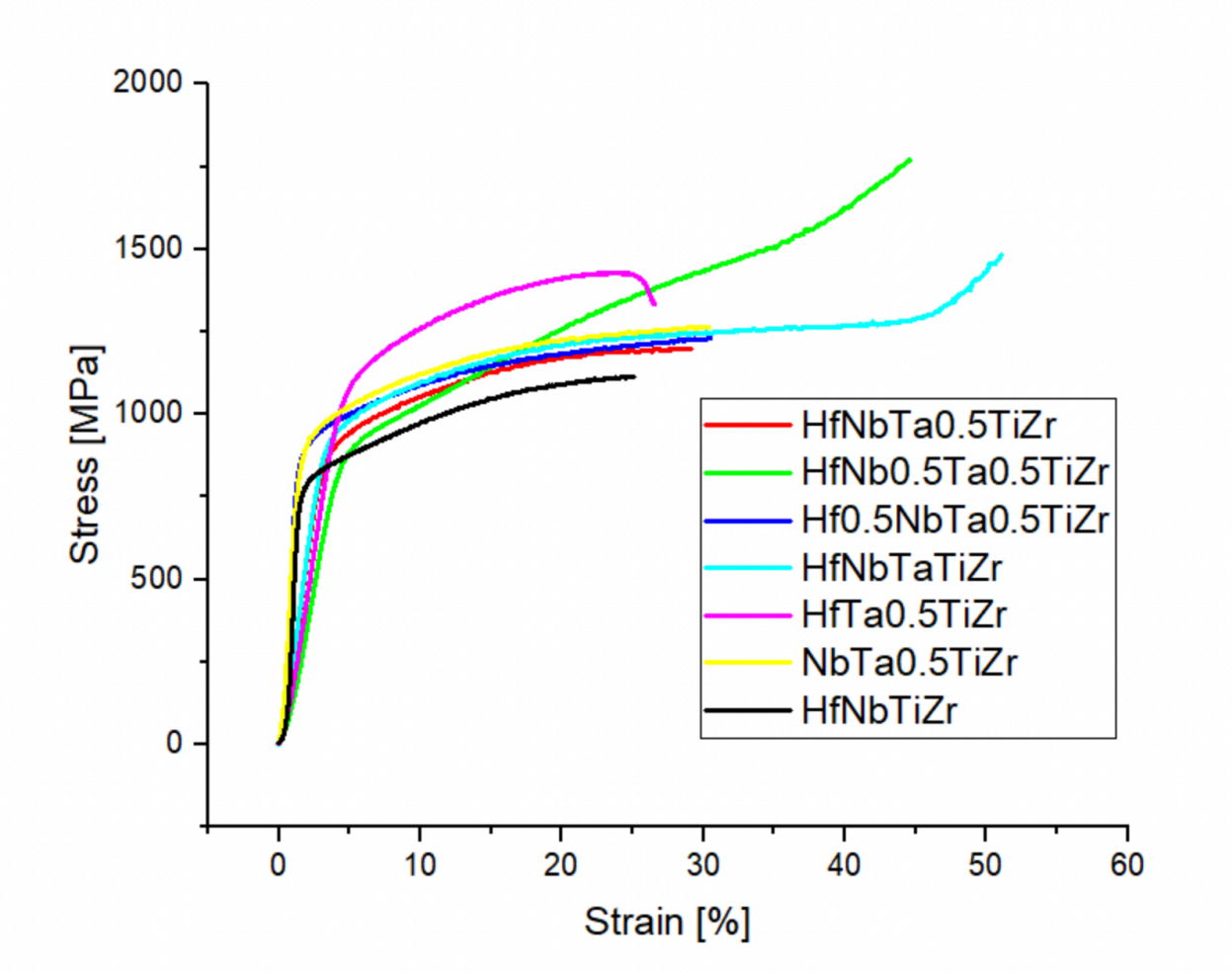


Figure 51: Compression Stress-Strain Curve

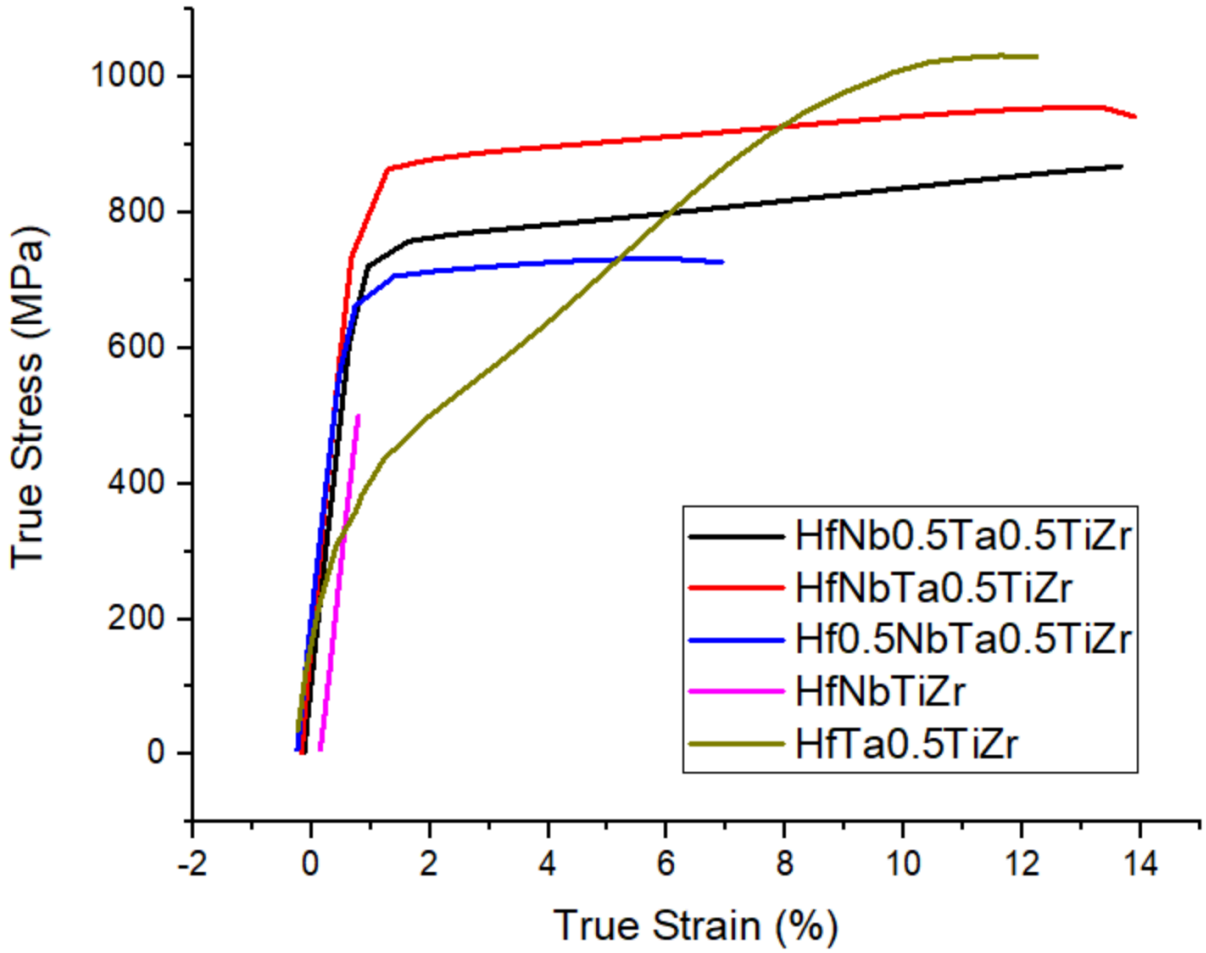


Figure 52: Tension Stress-Strain Curve

following chapter. All the compositions show promising toughness, but in the pursuit of ductile RHEAs, transition induced plasticity (TRIP) is a major focus.

Conclusion

The compositions were designed to have room temperature ductility while retaining the benefits of RHEAs, such as their strength at high temperatures. The increased room temperature ductility will cut costs in fabrication and machining, because of the relative ease compared to other, more brittle RHEAs.

After observing the compression data, the results of the room-temperature mechanical testing were promising. To strengthen the research, proof of deformation mechanisms was needed. Typically, pre- and post-mortem samples are compared, but real-time deformation mechanisms are superior for showing strengthening properties, and a proposal for beamtime at ORNL was constructed where tension data was also obtained.

From our original goal of designing and fabricating at least 4 ductile RHEAs at room temperature, we were able to fabricate 3 successful tension samples that showed great percent elongation, and all 7 composition showed a high percent plasticity with no catastrophic failures observed during compression testing.

CHAPTER FOUR

X-Ray Diffraction Results

Disclosure

The following X-Ray Diffraction (XRD) results were obtained by Dr. Eric Lass and Melanie K. Moczadlo.

Introduction

Following the completion of the compression tests, XRD patterns were obtained for each composition for both pre- and post-mortem samples. With the major goal of this research to find RHEA compositions that show TRIP, the XRD data provides confirmation of phases before compression, and either phase stability or the presence of new phases in post compression.

HfNbTiZr

The HfNbTiZr alloy has been previously studied and reported as a well-organized single-phase BCC. This composition allows for the study of the plastic deformation without concern for deformation mechanisms such as TRIP [28]. Figure 53 shows the XRD from the as-cast sample. Figure 54 presents the XRD from the post compression sample. The sole BCC phase confirms the purely plastic deformation without phase transitions.

HfNbTaTiZr

The HfNbTaTiZr equimolar alloy had been previously studied and is known as a single-phase BCC RHEA. Phase stability in the intermediate temperature region has been previously studied, with annealing temperatures ranging from 500 °C to 1,000 °C. Starting around 700 °C, The alloy was shown to decompose into three major phases: a BCC matrix, a BCC Ta-Nb-rich, and HCP Zr-Hf-rich precipitates [29]. The as-cast samples are shown to be a single-phase BCC in Figure 55, and do not appear to have a phase transformation post-compression as shown in Figure 56.

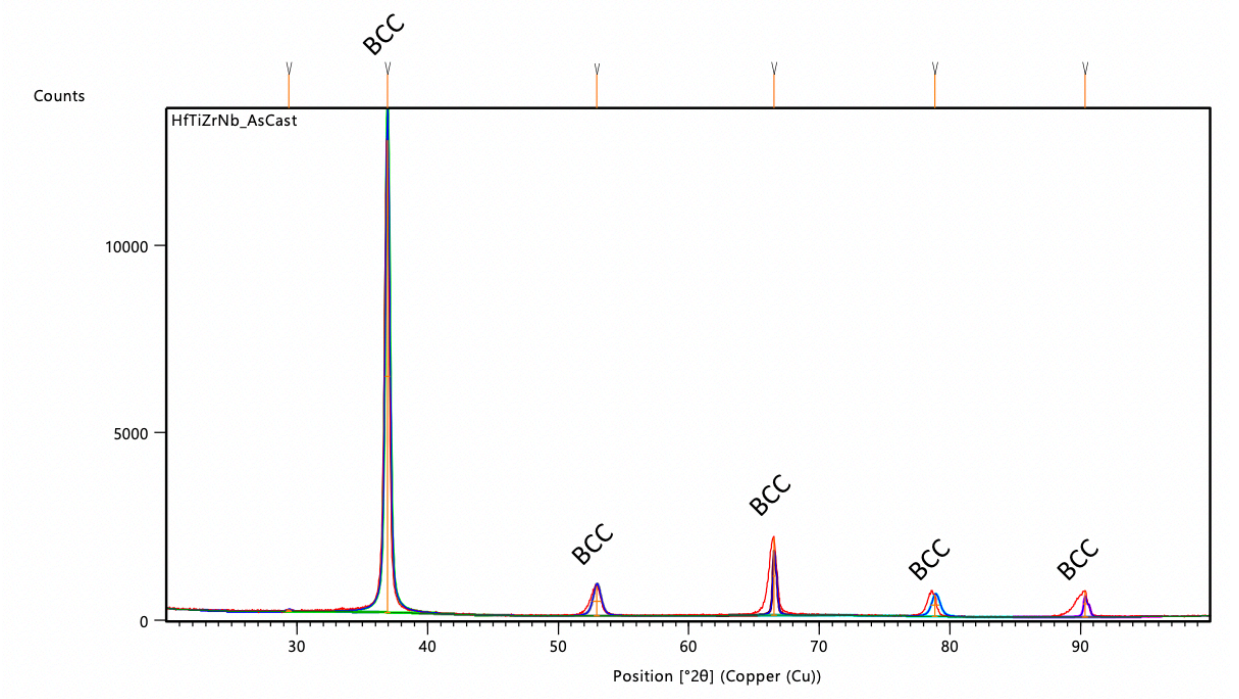


Figure 53: As-Cast HfNbTiZr XRD

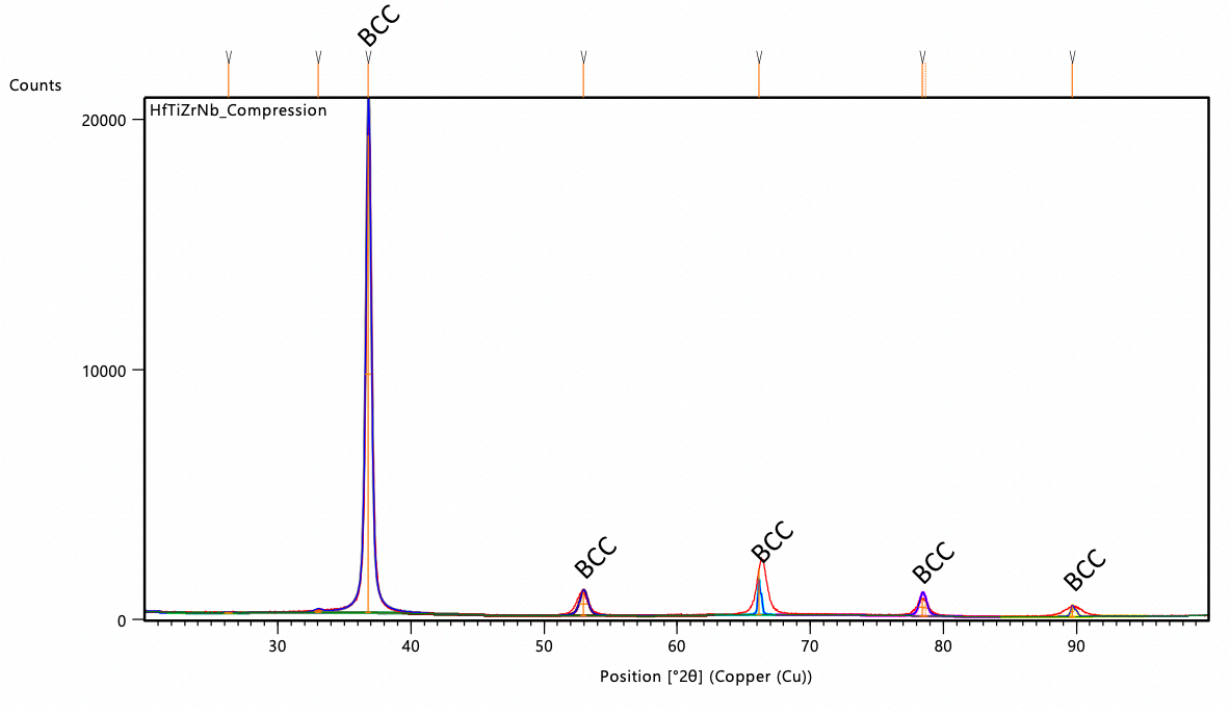


Figure 54: Post-Mortem HfNbTiZr XRD

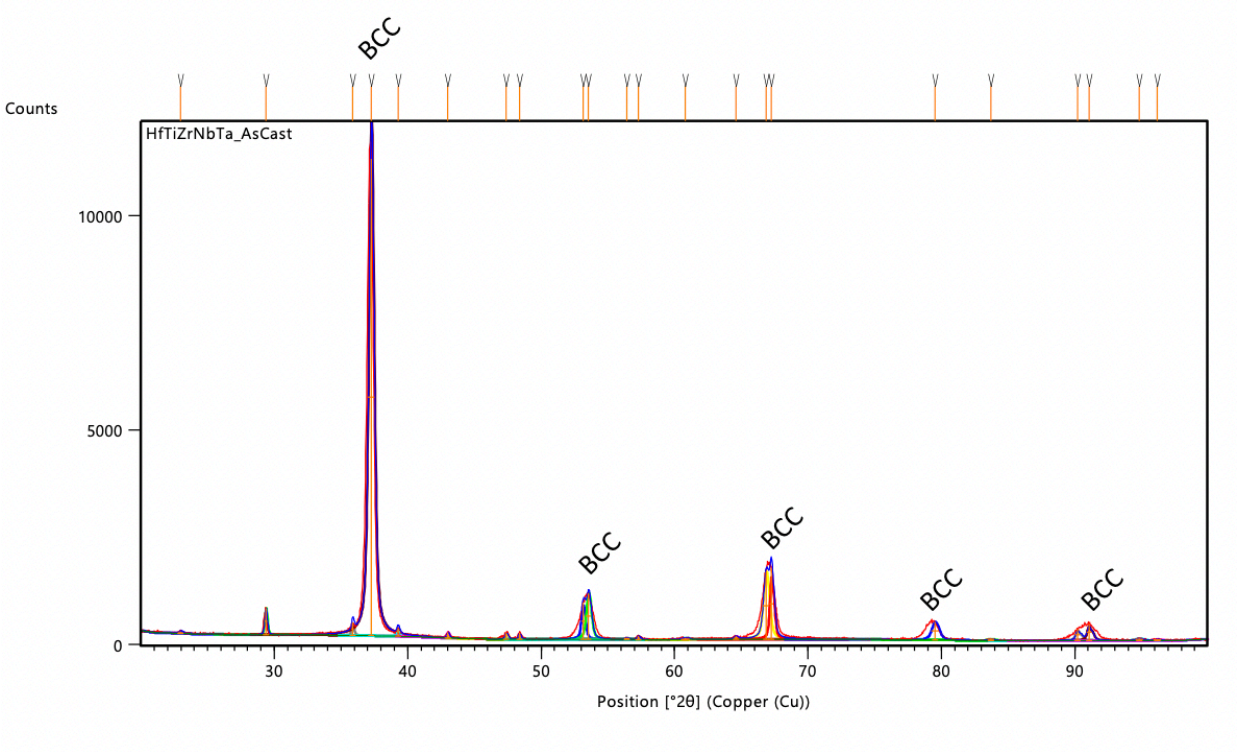


Figure 55: As-Cast HfNbTaTiZr XRD

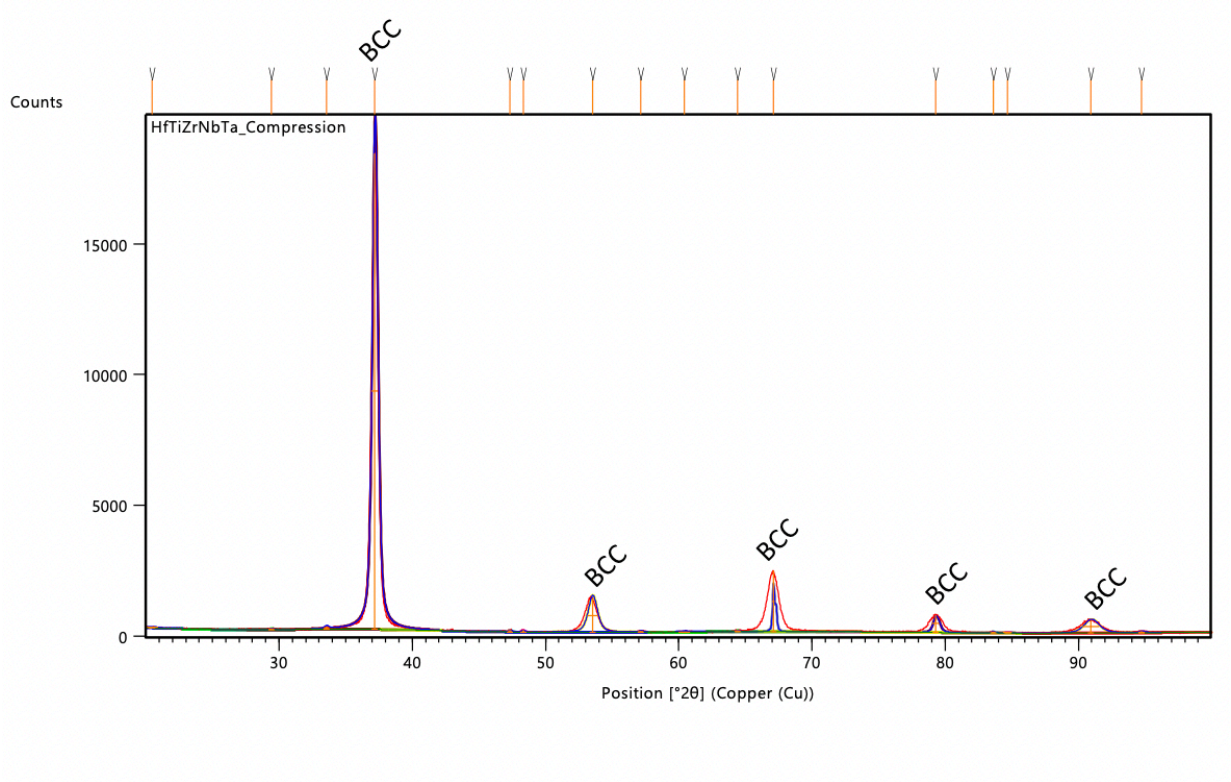


Figure 56: Post-Mortem HfNbTaTiZr XRD

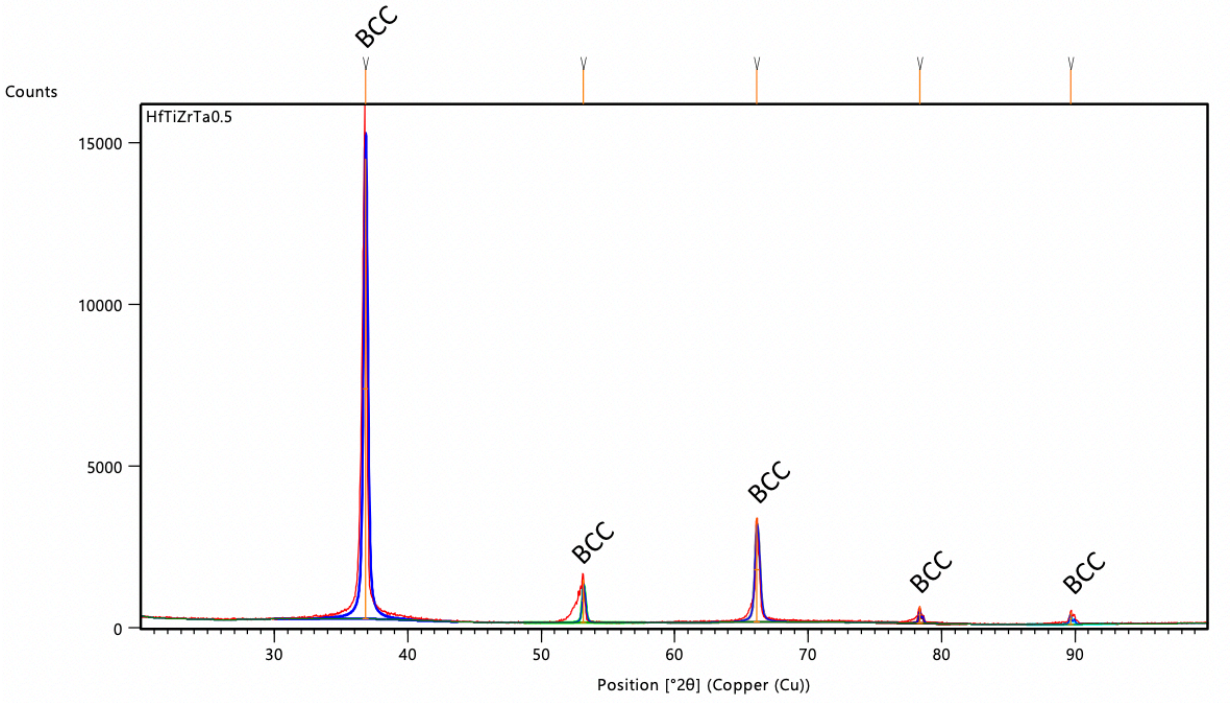


Figure 57: As-Cast $HfTa_{0.5}TiZr$ XRD

$HfTa_{0.5}TiZr$

The as-cast $HfTa_{0.5}TiZr$ is exhibited as a likely single-phase BCC structure in Figure 57. The $HfTa_{0.5}TiZr$ is a theorized TRIP alloy, and the XRD pattern comparison from pre to post-mortem samples show signs of new phases and the possibility of the appearance of an HCP phase in Figure 58. Previous publications report the equimolar HfTaTiZr as a single-phase BCC, but upon lowering the amount of Ta in the alloy, TRIP was introduced [30].

$HfNb_{0.5}Ta_{0.5}TiZr$

The as-cast $HfNb_{0.5}Ta_{0.5}TiZr$ is shown as a likely single-phase BCC structure in Figure 59. The post-compression XRD pattern in Figure 60 for $HfNb_{0.5}Ta_{0.5}TiZr$ is shown to maintain the BCC structure, showcasing the possibility of a ductile BCC structure in the RHEA.

$HfNbTa_{0.5}TiZr$

The as-cast $HfNbTa_{0.5}TiZr$ shows strong single-phase BCC peaks in the XRD pattern in Figure 61. The post-compression XRD pattern in Figure 62 exhibits no new peaks, signaling phase stability and a possible composition for studying ductile BCC RHEAs.

$Hf_{0.5}NbTa_{0.5}TiZr$

The as-cast $Hf_{0.5}NbTa_{0.5}TiZr$ shows single-phase BCC peaks in the XRD pattern in Figure 63 similar to the two previously mentioned alloys. Also like the previous two alloys, the post-compression XRD pattern in Figure 64 shows no new peaks, giving another stable single-phase BCC RHEA.

$NbTa_{0.5}TiZr$

The XRD pattern of the as-cast $NbTa_{0.5}TiZr$ in Figure 65 shows a large BCC structure, but with the other peaks present, this is most likely not a single-phase BCC alloy. The XRD pattern of the post-compression $NbTa_{0.5}TiZr$ in Figure 66 has less noise or fewer insignificant peaks. Further results would be needed for a strong conclusion, but it is possible that the strain caused the BCC structure to stabilize in the alloy.

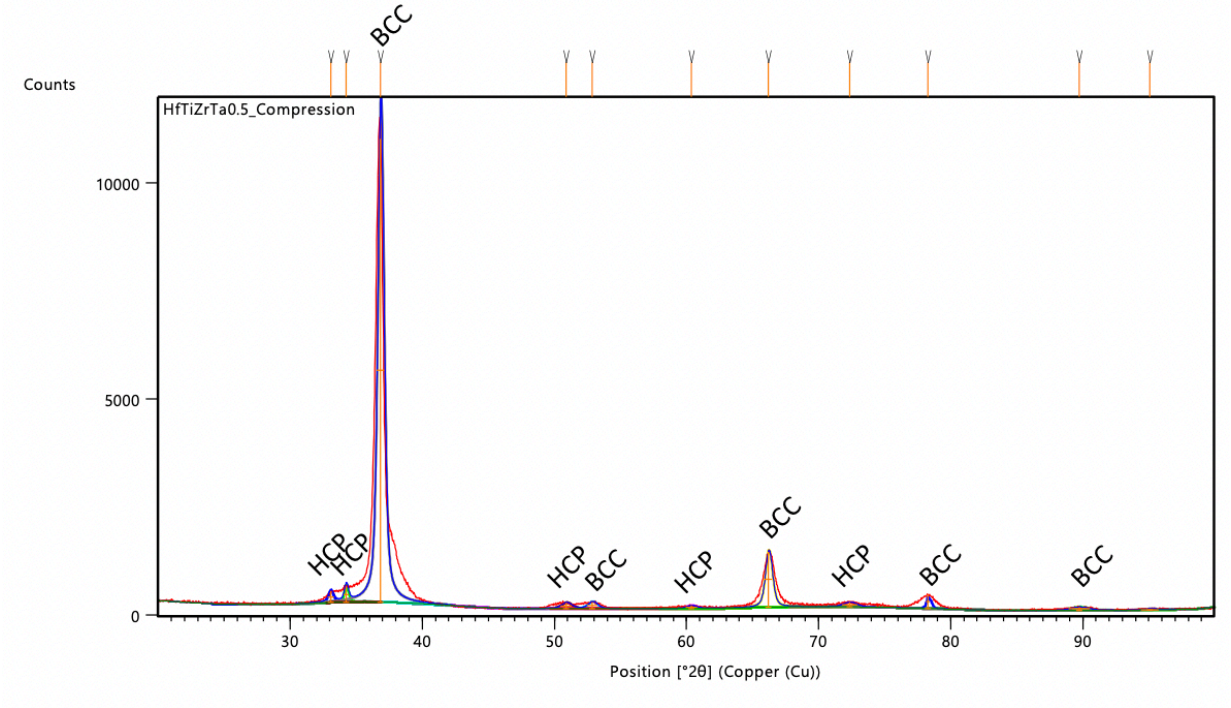


Figure 58: Post-Mortem $HfTa_{0.5}TiZr$ XRD

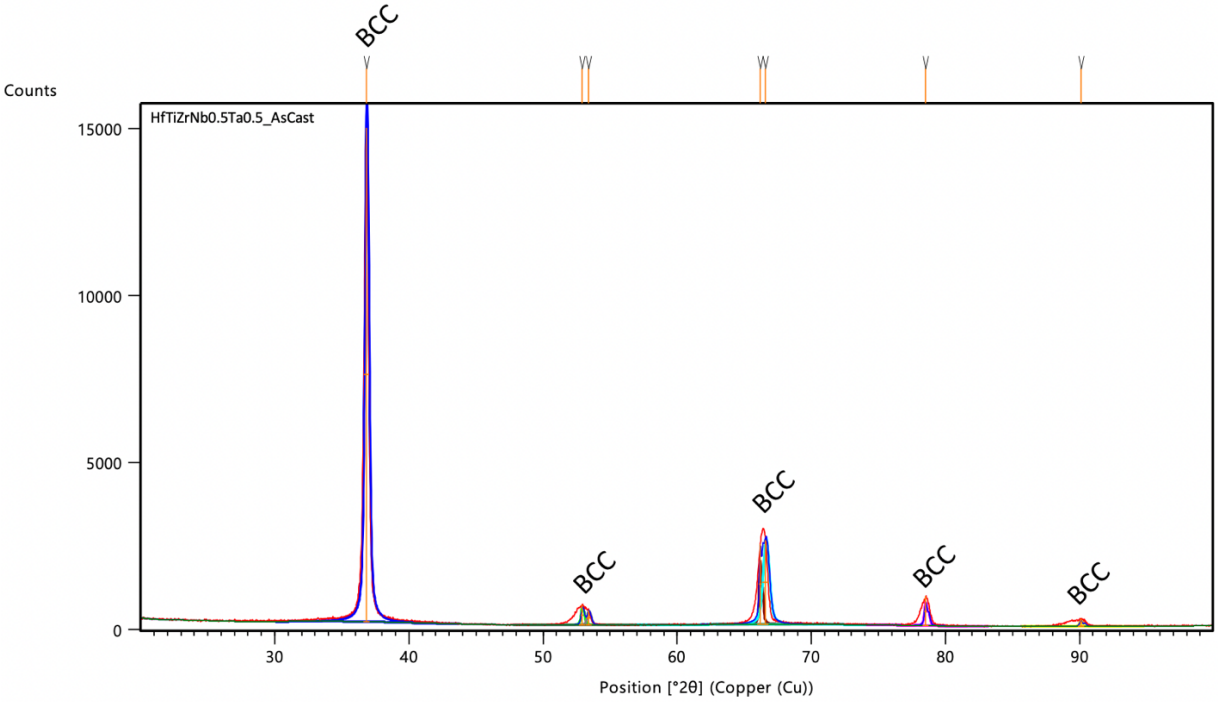


Figure 59: As-Cast $HfNb_{0.5}Ta_{0.5}TiZr$ XRD

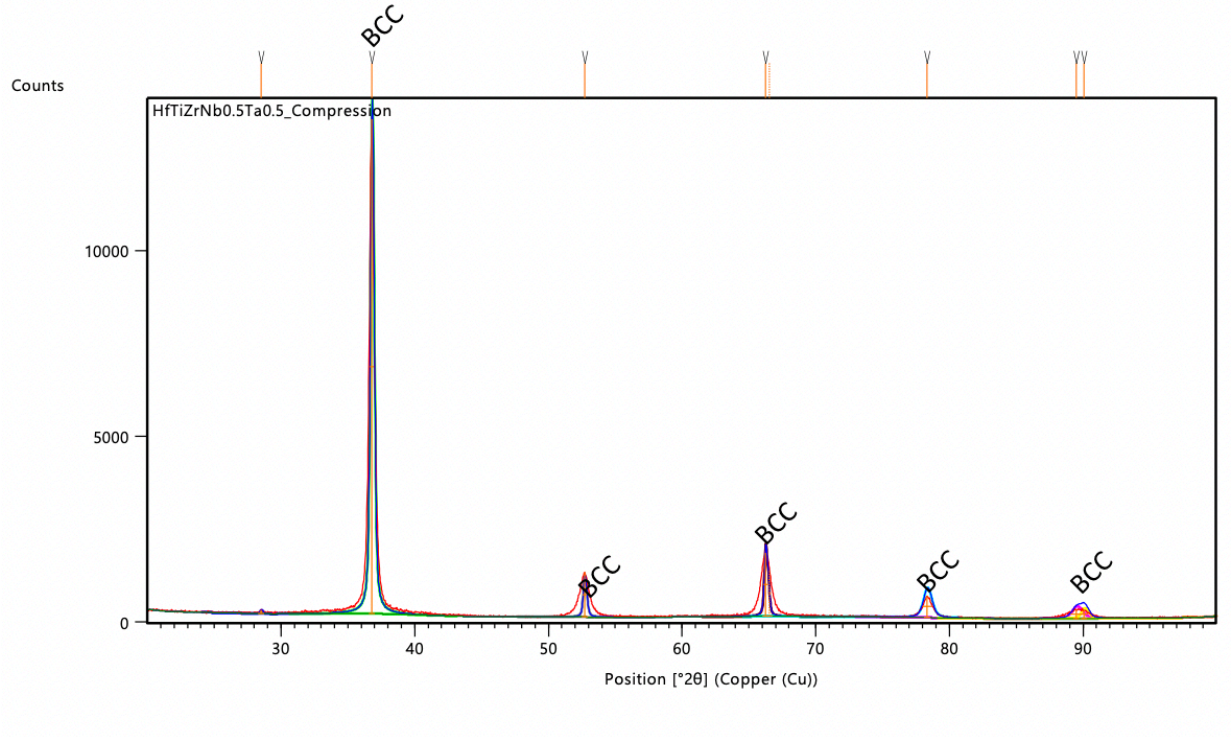


Figure 60: Post-Mortem $HfNb_{0.5}Ta_{0.5}TiZr$ XRD

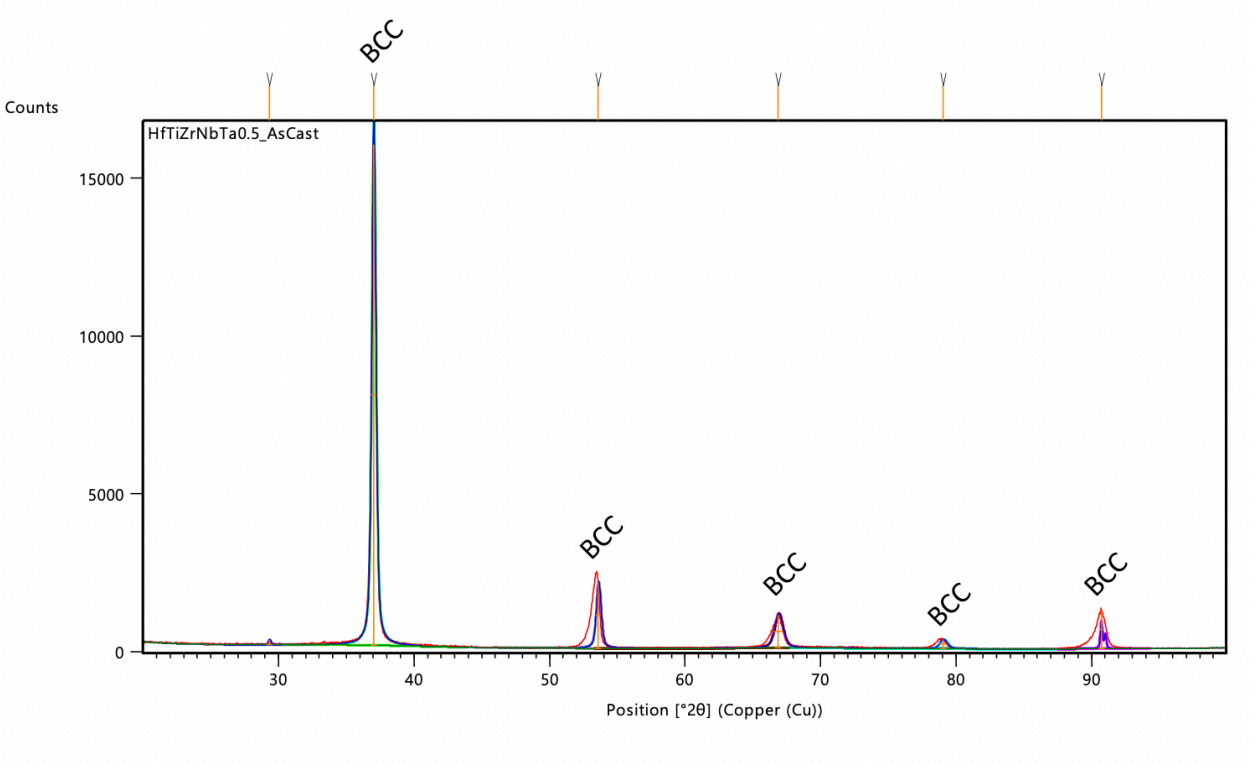


Figure 61: As-Cast $HfNbTa_{0.5}TiZr$ XRD

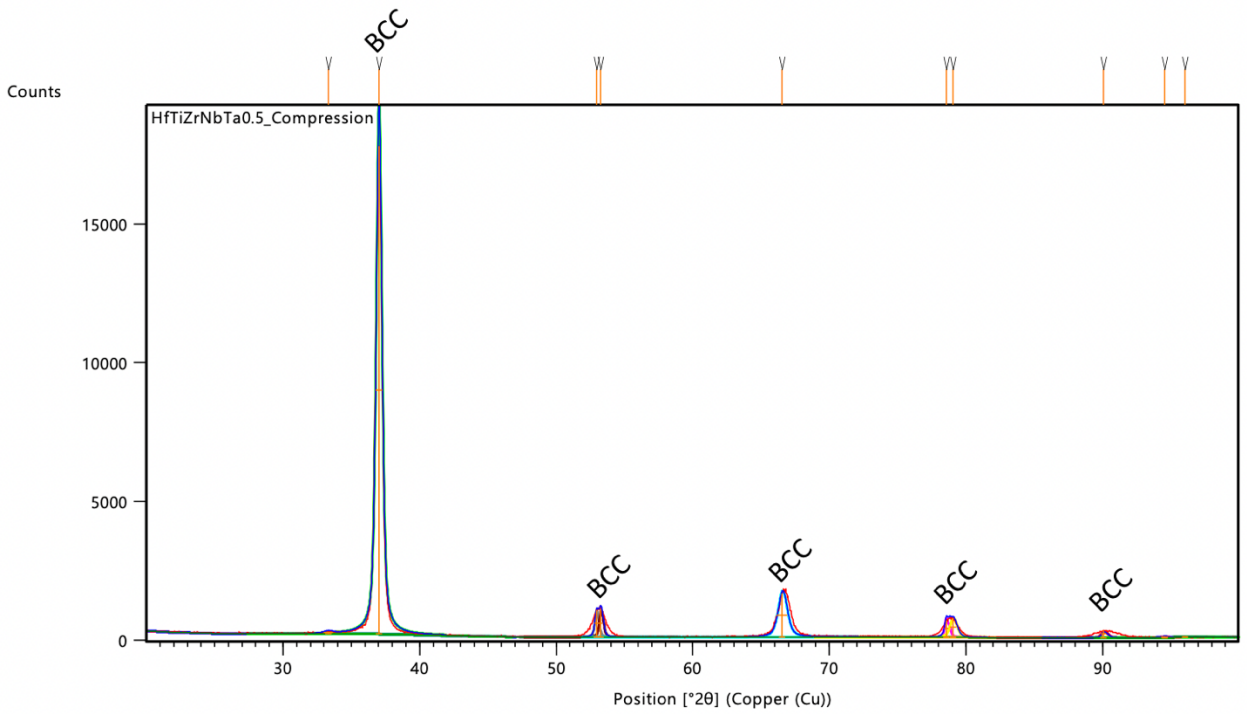


Figure 62: Post-Mortem $HfNbTa_{0.5}TiZr$ XRD

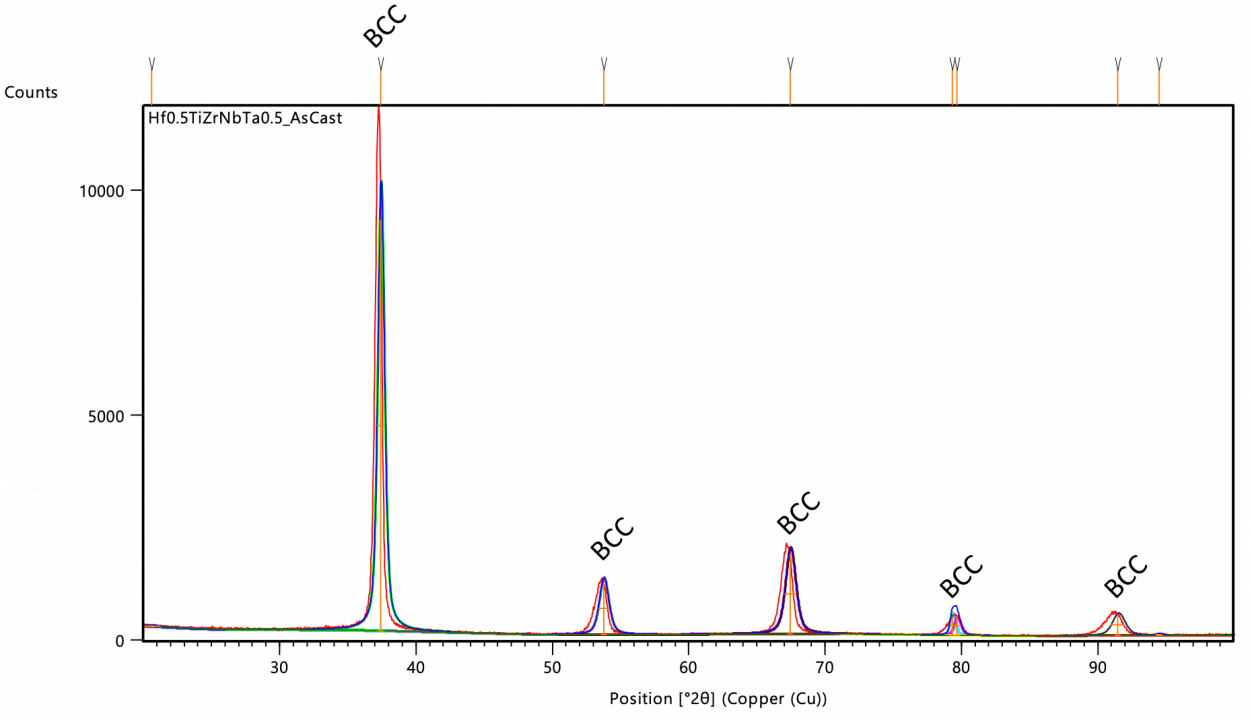


Figure 63: As-Cast $Hf_{0.5}NbTa_{0.5}TiZr$ XRD

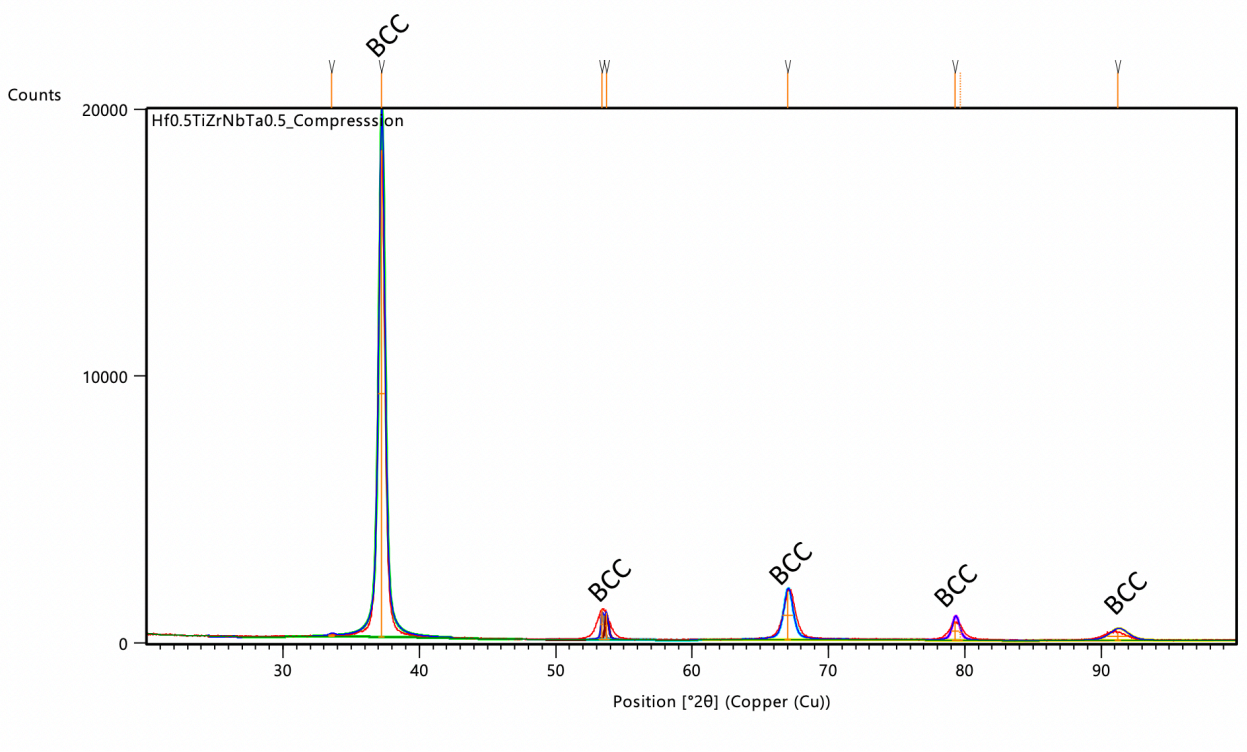


Figure 64: Post-Mortem $Hf_{0.5}NbTa_{0.5}TiZr$ XRD

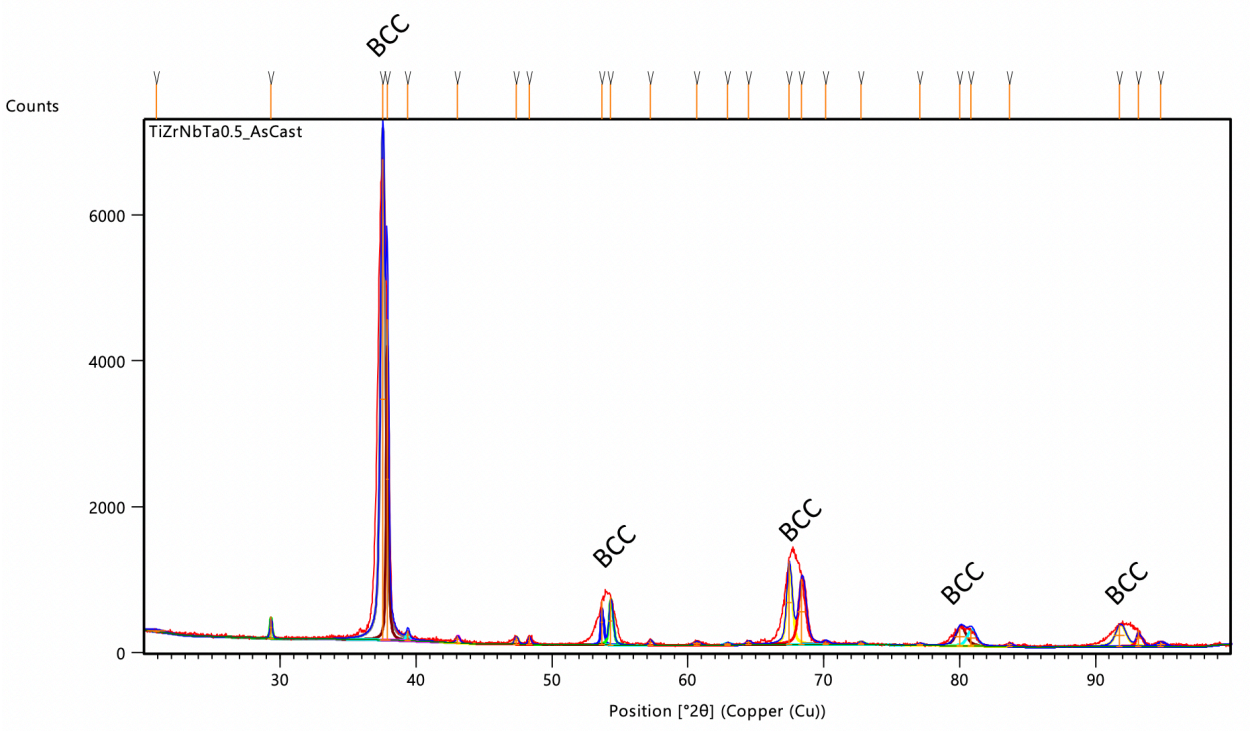


Figure 65: As-Cast $NbTa_{0.5}TiZr$ XRD

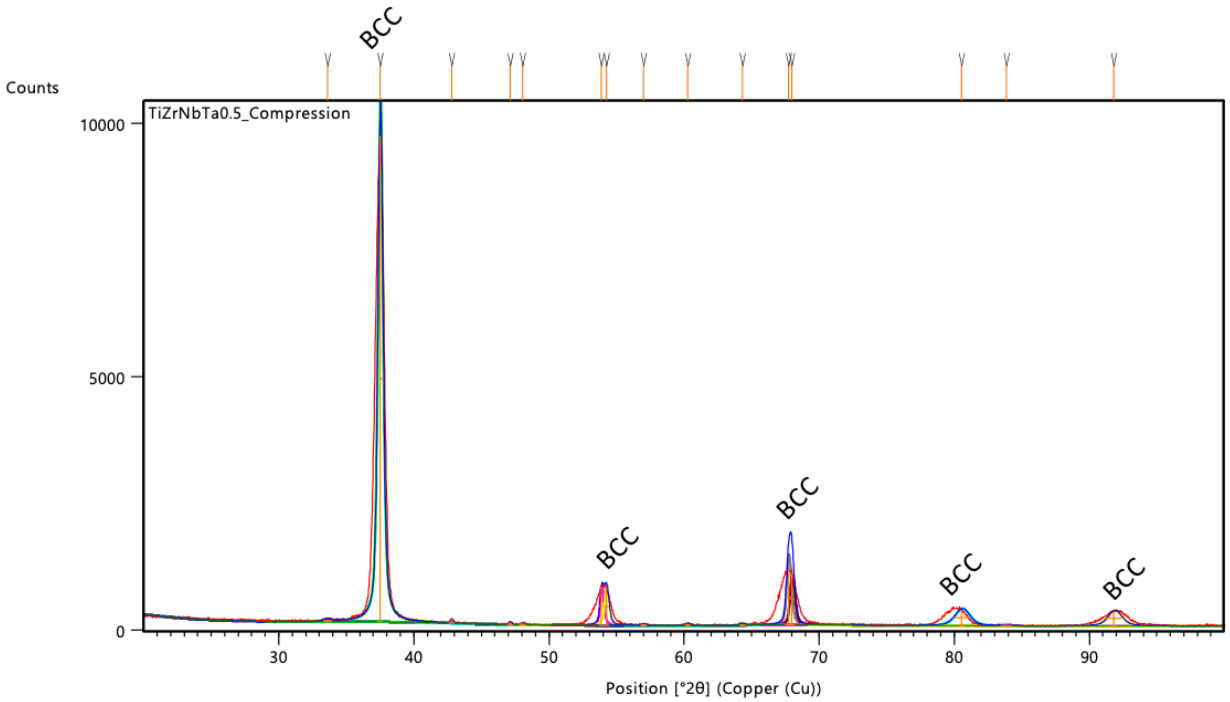


Figure 66: Post-Mortem $NbTa_{0.5}TiZr$ XRD

Conclusion

From the promising results of the compression and tension testing, $HfTa_{0.5}TiZr$ was hopeful to be a TRIP RHEA. This is most likely seen as the appearance of new peaks in the postmortem XRD, but to strengthen the results, *in-situ* neutron diffraction was used to confirm the phase transitions occurring under stress. From the remaining compositions, HfNbTiZr, HfNbTaTiZr, $HfNbTa_{0.5}TiZr$, $HfNb_{0.5}Ta_{0.5}TiZr$, and $Hf_{0.5}NbTa_{0.5}TiZr$ all show a single BCC phase pre and post compression. The $NbTa_{0.5}TiZr$ composition may have a BCC single-phase stabilization post-compression, but the *in-situ* neutron diffraction testing will confirm or deny this hypothesis.

CHAPTER FIVE

Proposal for Neutron Diffraction and Preliminary Results

Novelty of Research

From the results of the mechanical testing of the set of RHEAs, a further study using neutron diffraction would provide the real-time deformation mechanism of the alloys. This feature had not yet been studied, and with the close access to Oak Ridge National Lab (ORNL), the following was proposed for the VULCAN Beamline at the Spallation Neutron Source at ORNL for the 2023 beamtime cycle.

Disclosure

This proposal was accepted, and the beamtime was given for January 6th-9th 2023. The authors for the proposal are John Whitlow, Lia Amalia, Xuesong Fan, Eric Lass, and Peter K. Liaw.

Scientific Importance

High-entropy alloys (HEAs), which contain four or more principal elements, have been well developed in the recent decade showing excellent mechanical properties for future structural applications [31]. In the development of materials for high-temperature applications, refractory high-entropy alloys (RHEAs), which mainly contain refractory elements such as niobium, molybdenum, tantalum, and tungsten, have the potential to be applied at high-temperature services due to their high strengths at elevated temperatures [24, 26]. However, it is difficult to machine and process RHEAs since their ductility is relatively low, especially at room temperature [24, 32]. Some work has been done to enhance the ductility of RHEAs by means of solid solution strengthening via composition tuning and/or grain refinement via powder metallurgy fabrication processes [21-27]. However, in the effort to develop ductile RHEAs, the deformation mechanism in real time has not been extensively studied, meaning that the evidence of ductility can only be found post-mortem. To understand the activated mechanisms during the deformation of ductile RHEAs, real time-time *in-situ* diffraction studies of the micromechanical response are vitally important to accelerate the process of developing highly ductile yet strong RHEAs at room temperature.

Preliminary Work

Figure 67 presents the compressive stress-strain curve of our present work, HfNbTiZr, HfNbTaTiZr, $HfTa_{0.5}TiZr$, $HfNb_{0.5}Ta_{0.5}TiZr$, $HfNbTa_{0.5}TiZr$, $Hf_{0.5}NbTa_{0.5}TiZr$, and $NbTa_{0.5}TiZr$, compared with published data of RHEAs with similar compositions [26]. The compositions in the present work were obtained from CALculation of PHAse Diagrams (CALPHAD) to derive the compositions with high theoretical tensile elongation while maintaining high strengths. Our preliminary compression test data surprisingly revealed that finely tuning the composition of the alloying element and eliminating molybdenum from the system could enhance the plasticity significantly, exceeding 45% strain without failure for most of our compositions. A recently published work on RHEAs with similar compositions, $TiZrHfTa_x$ (x = 0.8, 0.6, 0.5), shows that tantalum tuning may cause enhancement in ductility by forming deformation twins during tensile deformation, as shown in Figure 68 [32]. Another published work on the effect of composition tuning in RHEAs shows that $Ti_{35}Zr_{27.5}Hf_{27.5}Nb_5Ta_5$ has an improved ductility due to transformation-induced plasticity (TRIP) effect [33]. However, real-time *in-situ* deformation studies have not been conducted yet. Our collaborator, Prof. Eric Lass from the University of Tennessee, Knoxville (UTK), has calculated some of the Gibbs free energy of transformation from the body-centered cubic (BCC) to the hexagonal close-packed (HCP) crystal structure, where $HfTa_{0.5}TiZr$ and Hf $Nb_{0.5}Ta_{0.5}TiZr$ have $\Delta G^{BCC\text{-}HCP}$ of -2150 J/mol and -353 J/mol at 0 K, respectively. These values imply that the HCP phase is more stable than the BCC phase at low temperature, which further implies the possibility of the TRIP mechanism being activated during deformation, which would agree with a published work on a similar RHEA system [34]. Therefore, we have reasons to suspect that the higher plasticity of our designed compositions may come from either the effect of twinning formation or the TRIP effect during plastic deformations. In this proposed work, the objectives are (1) studying the effect of alloying element tuning on the deformation mechanisms of HfNbTiZr, HfNbTaTiZr, $HfTa_{0.5}TiZr$, $HfNb_{0.5}Ta_{0.5}TiZr$, $HfNbTa_{0.5}TiZr$, $Hf_{0.5}NbTa_{0.5}TiZr$, and $NbTa_{0.5}TiZr$ RHEAs in real time, (2) investigating the load partitioning between the identified phases during the *in-situ* compression and tensile studies, and (3) coupling with the Crystal Plasticity Finite Element Method (CPFEM) [35] to understand the activated deformation modes.

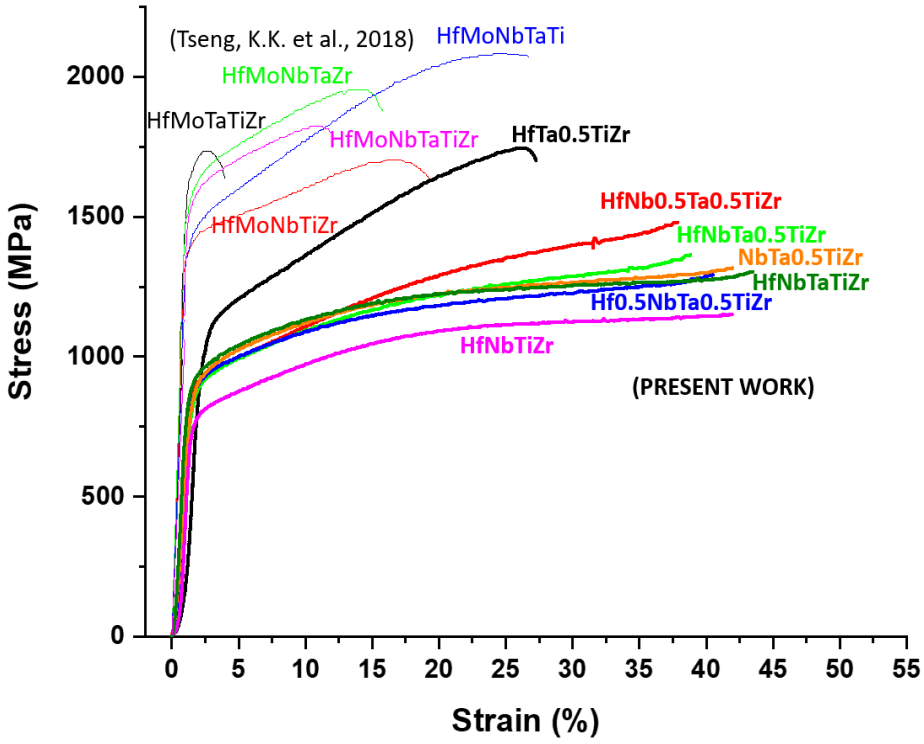


Figure 67: Stress-Strain Diagram

The compressive stress-strain diagram of the present work (shown in bold lines), compared with the published work of Ko-Kai Tseng et al. in 2018 [26].

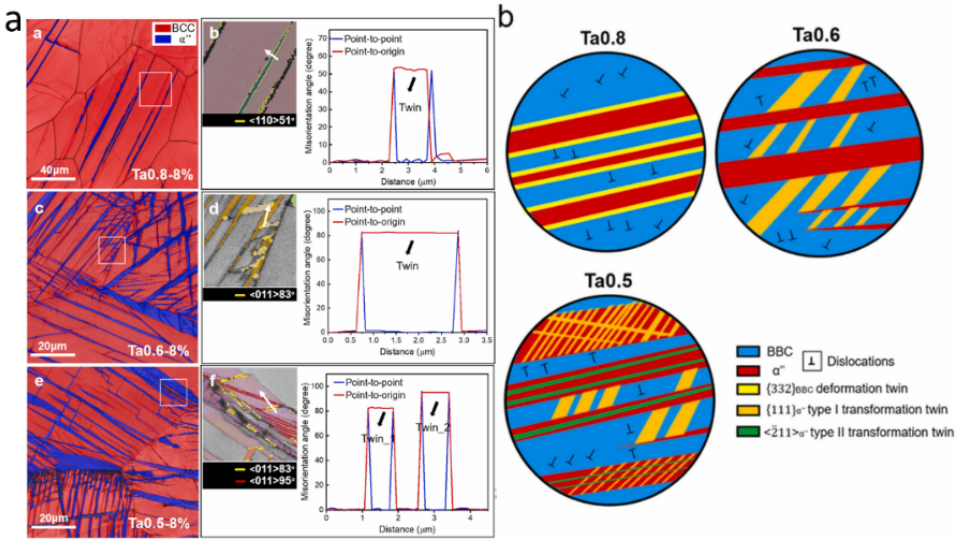


Figure 68: Deformation Mechanisms Illustration

(a) Twinning in body-centered cubic (BCC) structured $TiZrHfTa_x$ (x = 0.8, 0.6, 0.5) and (b) The illustration of deformation mechanisms for TiZrHfTax (x=0.8, 0.6, 0.5), showing deformation twins [32].

In preparation for the proposed research, sample fabrication and microstructural characterizations will be conducted at UTK. Tensile and compressive specimens on the designed RHEA compositions will be prepared by arc-melting a mixture of pure elements in a Ti-gettered argon atmosphere and then casting into copper molds with desired shapes. Scanning electron microscopy (SEM) coupled with electron backscatter diffraction (EBSD) and X-ray diffraction (XRD) will be conducted on both as-cast and deformed specimens to characterize the possible phase transformations and twinning formations in the designed RHEAs.

Choice of Instrument

For this experiment, we proposed to utilize the Engineering Materials Diffractometer (VULCAN) at SNS, which is highly capable for studying micromechanical behavior of multi-phased alloys. The feature that is most useful for this study is the real-time *in-situ* neutron diffraction (ND), which would provide the means of characterizing real-time deformation mechanisms, such as dislocation, twinning, and phase transformations. We will use VULCAN for *in-situ* monotonic tension and compression experiments. As similar studies were successfully conducted in VULCAN[24, 36], we are eager to study the deformation mechanisms of our RHEA compositions (HfNbTiZr, HfNbTaTiZr, $HfTa_{0.5}TiZr$, $HfNb_{0.5}Ta_{0.5}TiZr$, $HfNbTa_{0.5}TiZr$, $Hf_{0.5}NbTa_{0.5}TiZr$, and $NbTa_{0.5}TiZr$).

Experiment Plan

Uniaxial tension and compression tests will be conducted at room temperature. The *in-situ* ND patterns will be collected simultaneously during continuous loading. As mentioned previously, 7 RHEA compositions will be investigated in the proposed work. The detailed experiment procedures are shown below:

(1) Tensile tests will be conducted following the sample geometry provided by VULCAN for 3 mm room-temperature plates with the load limit of 15,600 N for a 2,000 MPa maximum stress.

(2) Compression tests will be conducted for 6 mm-diameter rods with the load limit of 56,550 N for a 2,000 MPa maximum stress.

Estimation of Measurement Time:

Total time = 2 hours (for initial safety and instrument trainings) + [5 hours (for tensile tests) + 4 hours (for compressive tests)] × 7 (RHEA compositions) + 0.5 hour (for experiment setup and possible beam loss) × 14 (experiments) = 72 hours. Since the specimen volume that is being measured by the neutron beam is smaller for tensile plates, the estimated time for tension is longer than that for compression. Therefore, we request 3 days of beam time to complete the proposed experiments.

Data Analysis and Scientific Outcomes

(1) The General Structure Analysis System (GSAS) will be used to analyze and refine the ND data and perform Rietveld refinements to investigate the possible phase transformations.

(2) The VULCAN Data Reduction and Interactive Visualization (VDRIVE) software will be employed for single-peak analyses to investigate the load transfer or partitioning.

(3) CPFEM will be coupled with the analyzed *in-situ* ND data to understand the lattice evolution and deformation mechanisms.

Safety Considerations

No hazardous substance, equipment, or procedure will be brought to or used at the SNS as part of this proposed research.

Introduction to Preliminary Results

Upon the completion of the *in-situ* neutron diffraction at ORNL, the process of analyzing data began. With the help of Lia Amalia, there are some preliminary results that can be reported now. An in-depth analysis will be published later on the results of the neutron diffraction. This publication will include microstructural characterization of the samples, such as SEM, TEM, and EBSD. Unfortunately, the samples were unable to be returned from ORNL, and no post-mortem characterization on the neutron diffraction samples will occur. Tension and Compression samples will be refabricated for microstructural characterization.

Work Hardening

Figure 69 shows the preliminary results of work hardening from the successful tension tests performed at ORNL. From these results, the curve of $HfTa_{0.5}TiZr$ is the most notable due to the increase in work-hardening seen in the middle range of strain. This composition was also published in work done by Huang et al. with varying amounts of Ta [30]. A similar stress-strain curve and work hardening rate was seen for the $HfTa_{0.4}TiZr$, but not for the $HfTa_{0.5}TiZr$ composition in their publication. The casting procedures were the same, as well as the shape in which the samples were cut. The likely cause behind this discrepancy is a difference between the calculated theoretical composition and actual experimental composition.

D-Spacing and Lattice-Strain Measurements

HfNbTiZr

Only the compression data is available for the HfNbTiZr RHEA due to the failure of the cast for the tension samples. Figure 70 shows the compression d-spacing and lattice strain compared to the stress of the sample. The d-spacing shows that there are no new phases present during plastic deformation, and instead presents a constant strain on the BCC-lattice parameters. This result agrees with the report on neutron diffraction of the same composition performed by Huang et al. [30].

HfNbTaTiZr

Similar to the HfNbTiZr RHEA, the HfNbTaTiZr only has the compression data due to poor casting. Figure 71 highlights the same plastic deformation without phase transformation as shown by HfNbTiZr. This was an expected result and is confirmed with no new peaks in the diffraction data.

$HfTa_{0.5}TiZr$

From earlier, $HfTa_{0.5}TiZr$ is expected to be a TRIP alloy. The lattice strain and d-spacing confirms the XRD data shown earlier in Figure 58. As discussed, the lower amount of Ta in the alloy is theorized to increase TRIP in the RHEA. Figure 72 shows the presence of a new phase, signaled by a new peak occurring in the d-spacing chart. The lattice-strain evolution also shows the lattice parameters shifting into an HCP phase from a BCC phase.

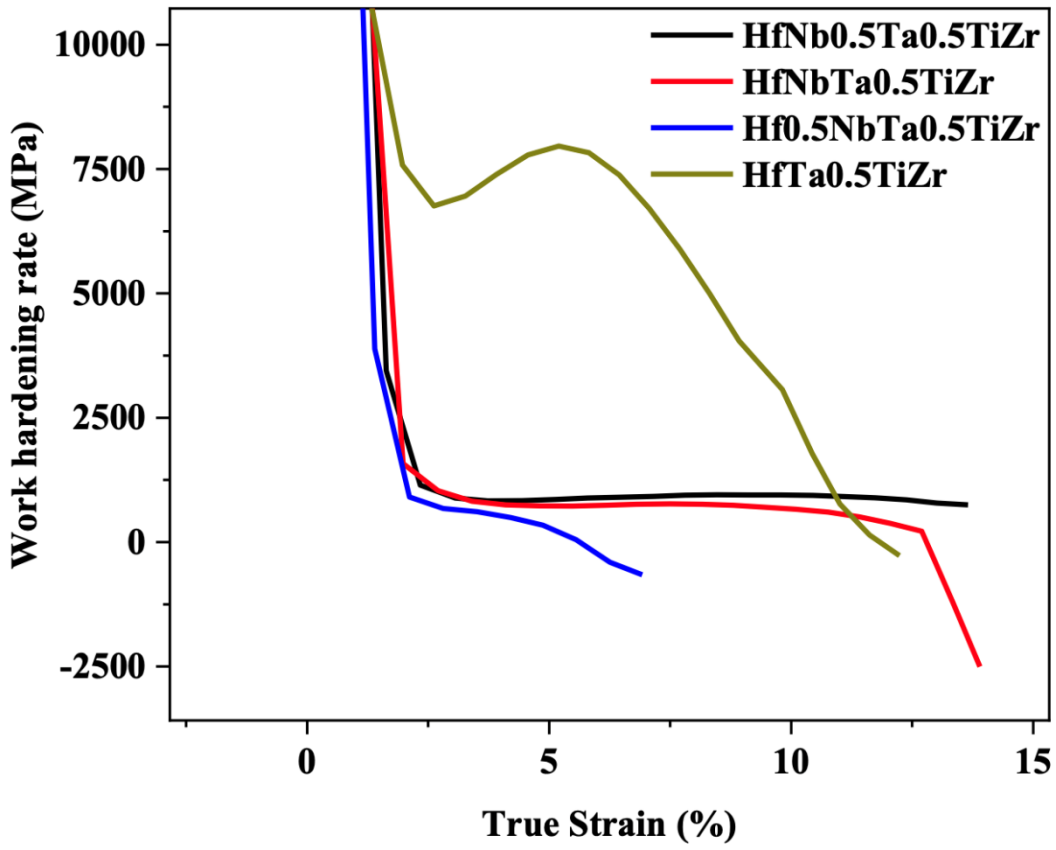


Figure 69: Work Hardening of Successful Tension Tests

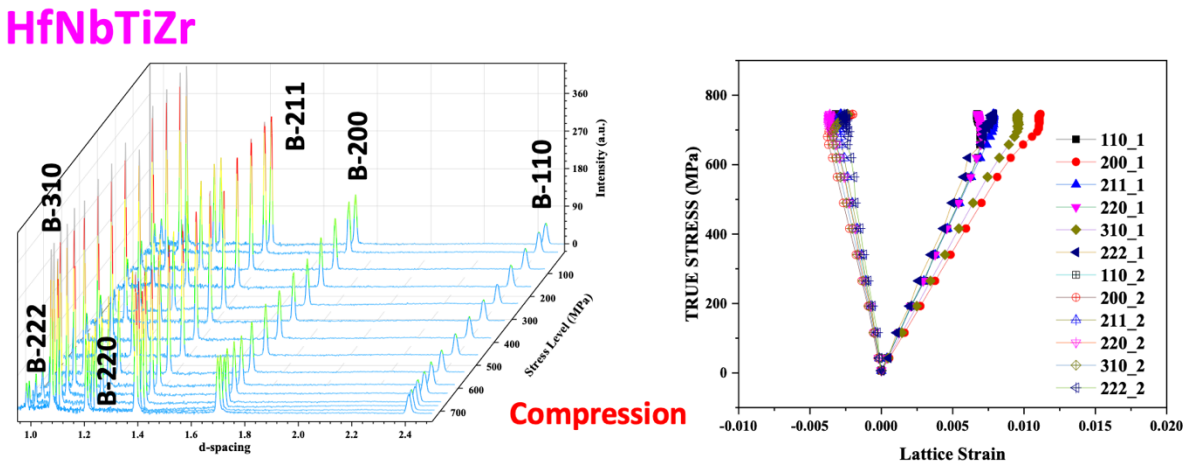
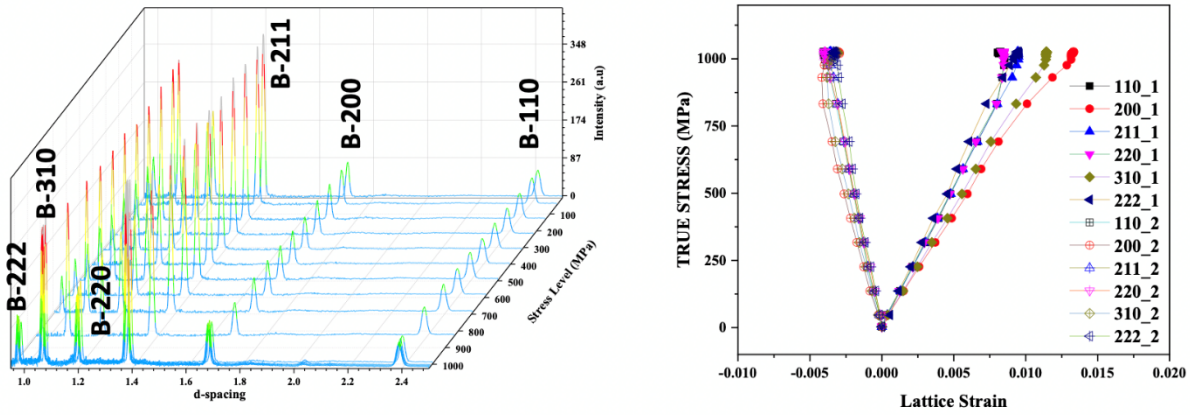


Figure 70: D-Spacing and Lattice Strain of HfNbTiZr

HfNbTaTiZr



Compression

Figure 71: D-Spacing and Lattice Strain for HfNbTaTiZr

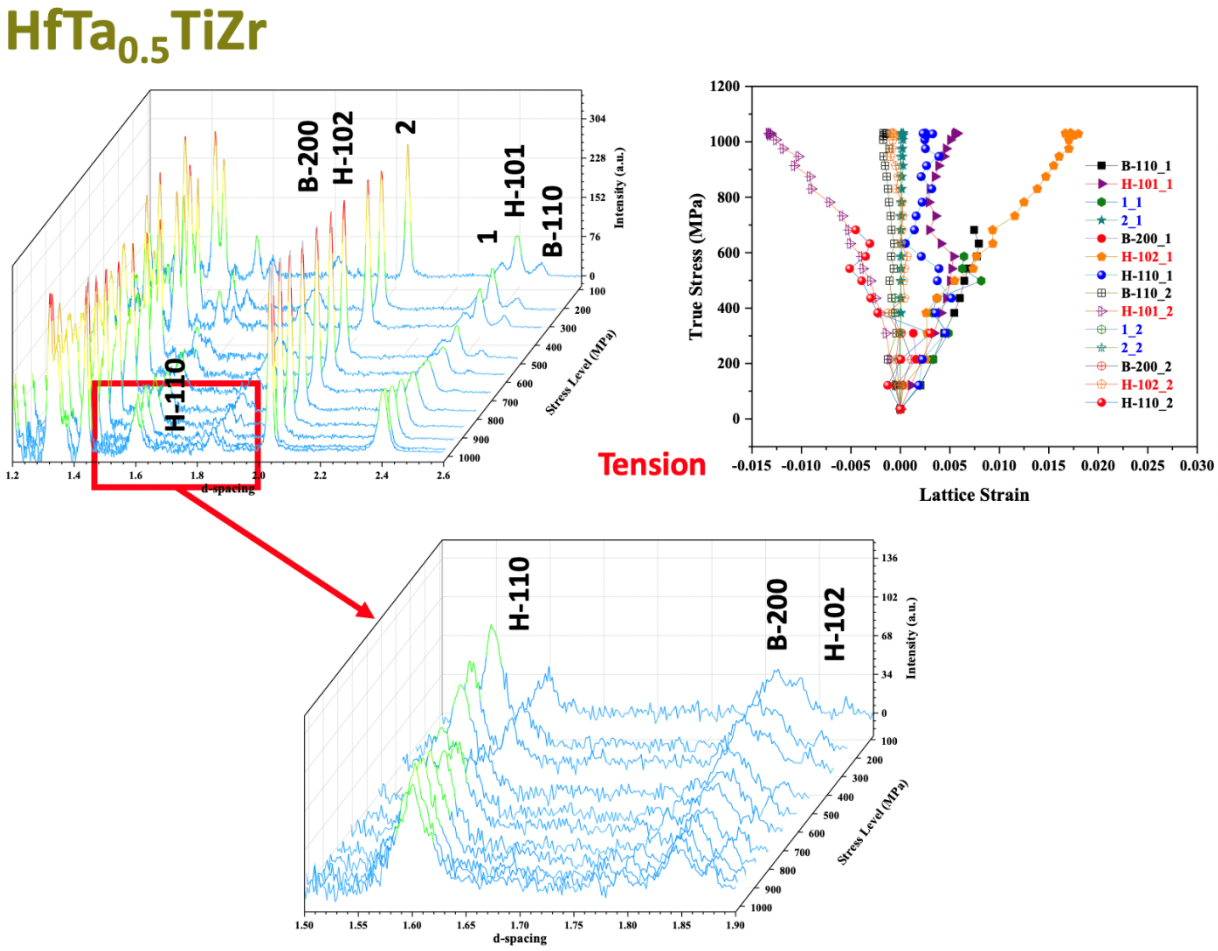


Figure 72: D-Spacing and Lattice Strain of $HfTa_{0.5}TiZr$

$HfNb_{0.5}Ta_{0.5}TiZr$

Figure 73 gives a very clean d-spacing and lattice-strain chart, with no new phases appearing during plastic deformation. In both tension and compression, a single BCC phase is present, and is represented by a somewhat constant lattice deformation with no transition into a new phase.

$HfNbTa_{0.5}TiZr$

The $HfNbTa_{0.5}TiZr$ has similar results to the $HfNb_{0.5}Ta_{0.5}TiZr$ RHEA, with a single BCC phase present throughout the plastic deformation of tension and compression tests. Figure 74 showcases another clean set of BCC peaks with the lattice deformation again pointing to a single-phase BCC alloy.

$Hf_{0.5}NbTa_{0.5}TiZr$

The tension and compression lattice strain and d-spacing portrayed in Figure 75 show another confirmed single-phase BCC RHEA. A small unidentified peak is seen in the d-spacing chart for tension data, but no new phases or presence of a secondary phase are seen in the lattice strain for tension or the charts for compression. This peak does not shift and does not grow with plastic deformation, along with the peak being present before and after plastic deformation suggests that it is another preferred orientation of the single-phase BCC.

$NbTa_{0.5}TiZr$

Figure 76 shows a chart much like the 5 other single-phase BCC RHEAs. The $NbTa_{0.5}TiZr$ alloy does not possess any new phases during or after plastic deformation, confirming that the alloy is a single-phase BCC. Although only compression data is available, because of the tension data from other single-phase alloys, $NbTa_{0.5}TiZr$ is theorized to be a stable single-phase BCC RHEA in compression and tension.

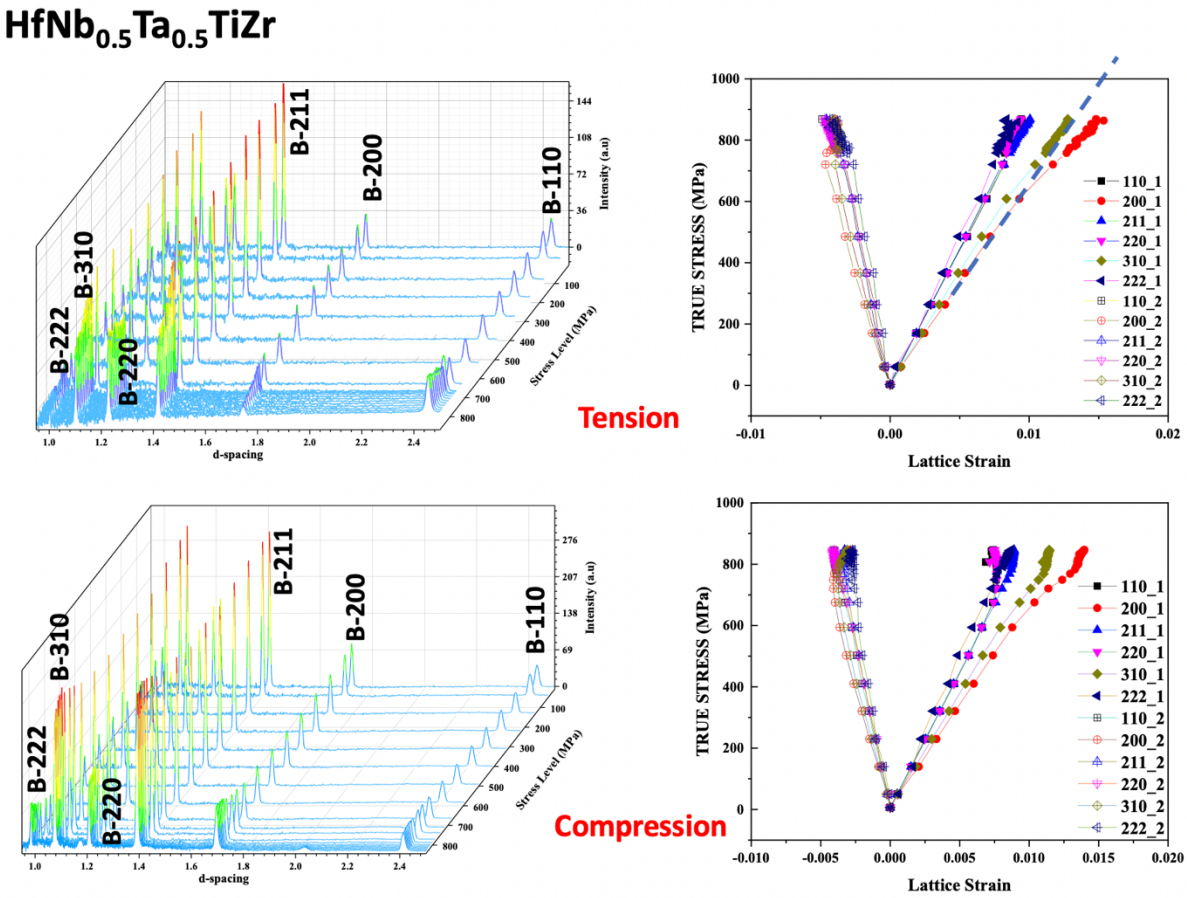


Figure 73: D-Spacing and Lattice Strain of $HfNb_{0.5}Ta_{0.5}TiZr$

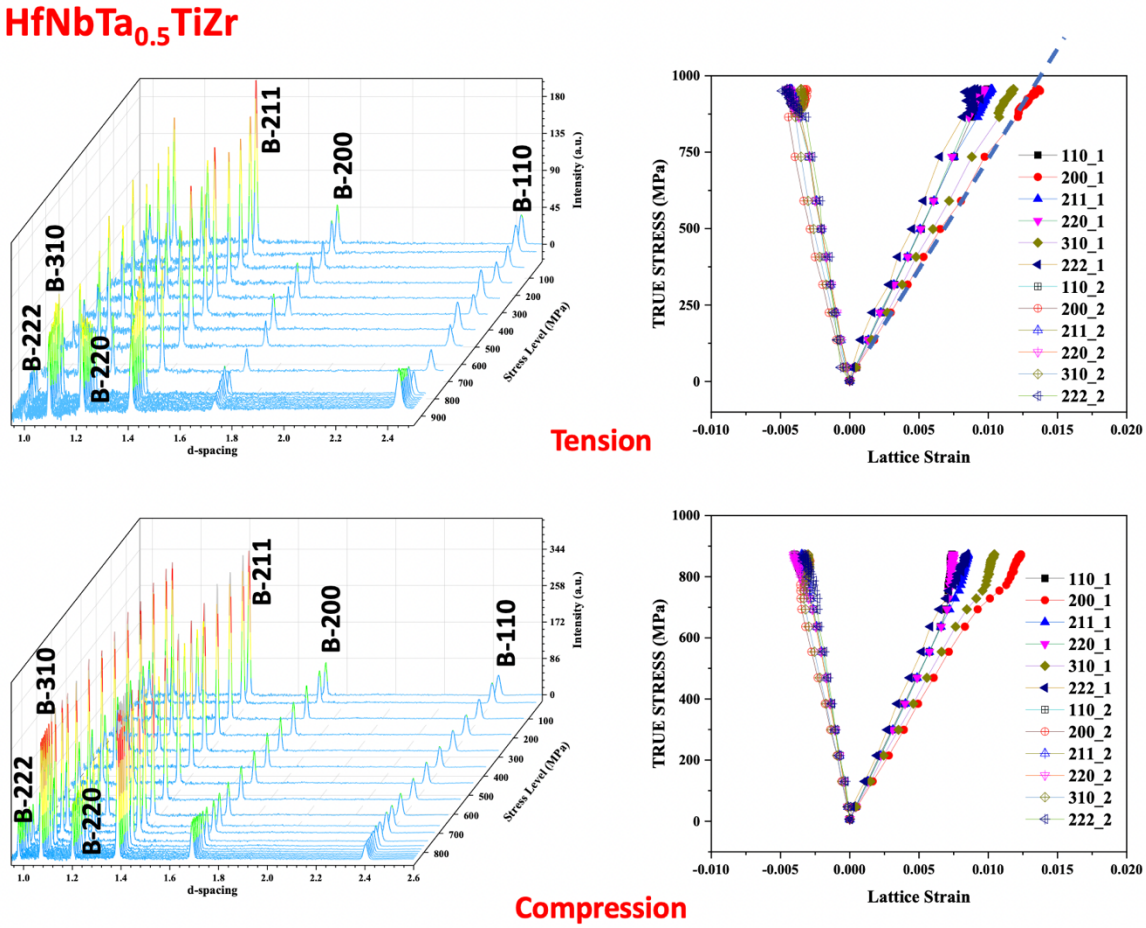


Figure 74: D-Spacing and Lattice Strain of $HfNbTa_{0.5}TiZr$

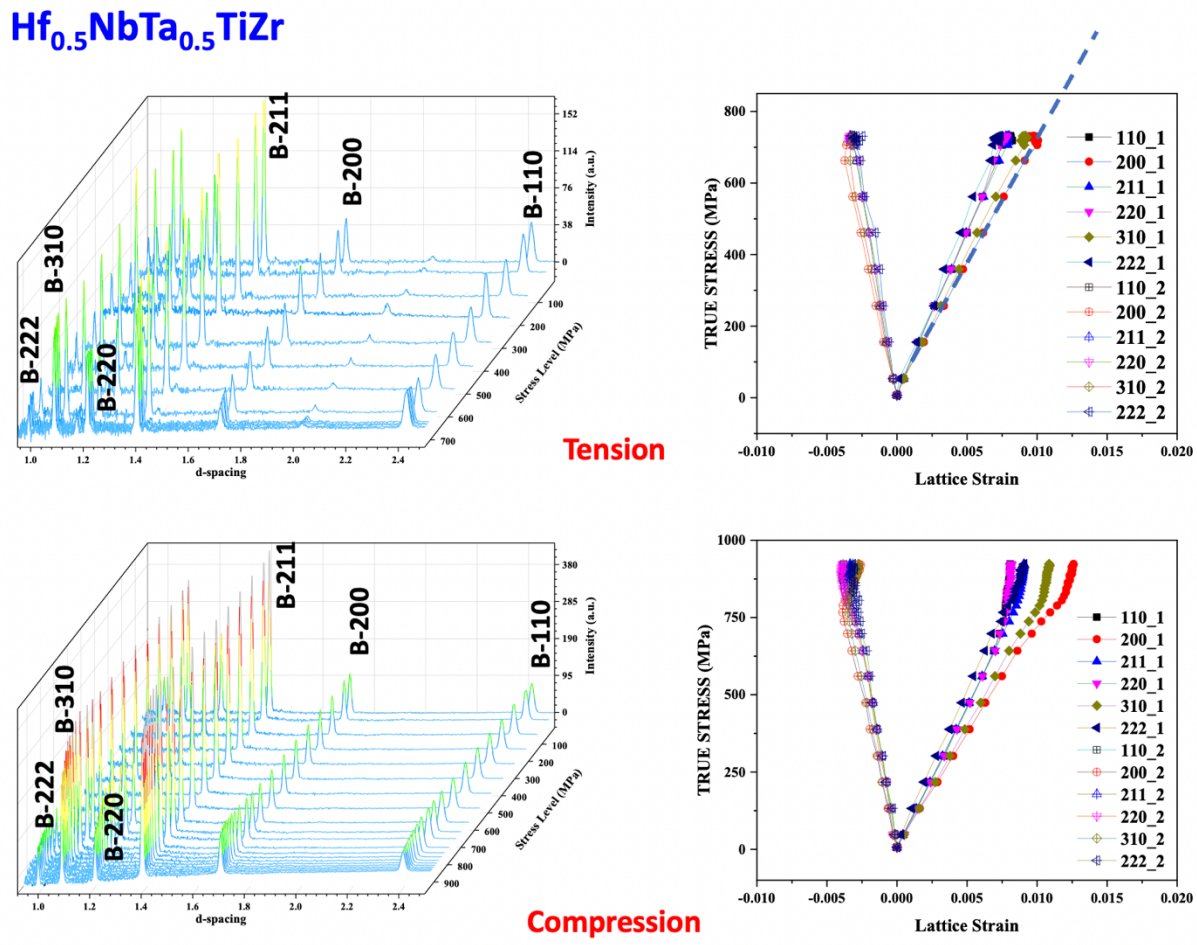


Figure 75: D-Spacing and Lattice Strain of $Hf_{0.5}NbTa_{0.5}TiZr$

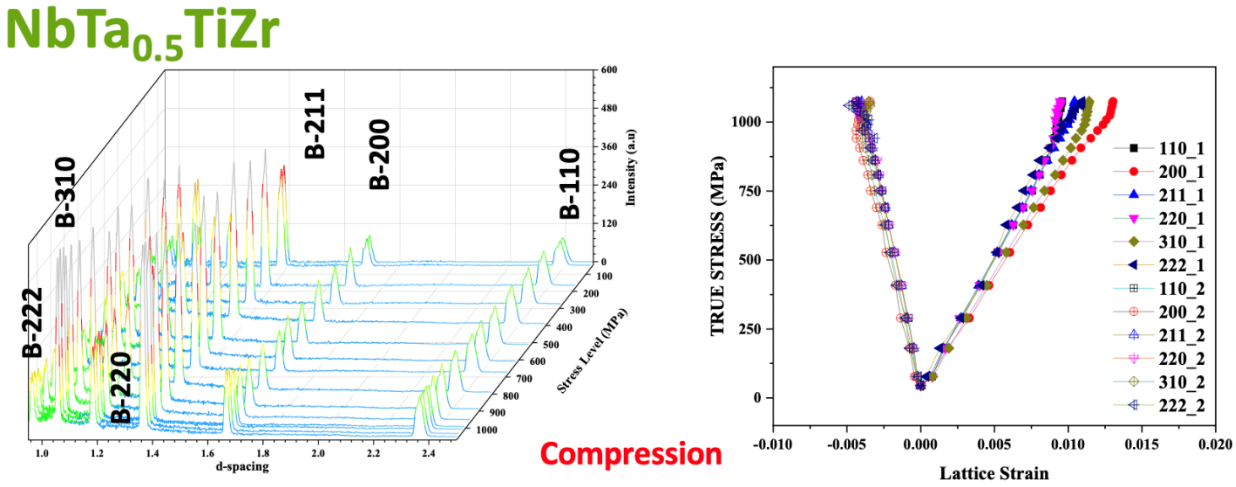


Figure 76: D-Spacing and Lattice Strain of $NbTa_{0.5}TiZr$

Elastic Modulus

The elastic modulus was calculated for 6 single-phase RHEAs, and compared to the measured values obtained at ORNL. These values can be seen in Table 16 for compression tests and in Table 17 for tension tests. Both tables show a strong trend between the measured values and the calculated values of the elastic modulus for different grain orientations. For example, with the HfNbTiZr alloy, the {200} and {310} grain orientations are calculated to be the first to yield in this isostrain condition, and the same can be seen with the measured values. This holds true for each of the compositions for which the elastic modulus was calculated and measured.

Kroner Bulk Modulus and Cauchy Pressure

Kroner Bulk Modulus has been used as the most accurate model to parallel experimental data for RHEAs and their ductility. After obtaining the data from VULCAN, Kroner's self-consistent model was used to calculate the single crystal elastic constants (C11, C12, C44, and S11, S12, S44) [37].

Cauchy Pressure ($C_{12} - C_{44}$) is a polycrystalline elastic modulus that has been shown to predict the elasticity and plasticity of RHEAs. It is often used to describe the type of atomic bonding present in the HEA. A positive value represents an increased degree of metallic bonding and thus, higher ductility, while a negative value represents covalent bonding and more brittle behavior [37].

Table 18 shows the calculated values for the single crystal elastic strain of the single-phase compositions. There is a trend supporting a higher Kroner Bulk Modulus representing a higher plasticity and ductility. The excel file used is planned to be offered as supplemental data to the publication on this set of RHEAs. Table 19 reports the mechanical test values from the VULCAN beamline at ORNL and compression tests from UTK for comparison.

Conclusion

The previously reported TRIP $HfTa_xTiZr$ (where $0 \leq x \geq 1$) continues to show promising results in ductility and strength. Further data analysis will show the deformation mechanisms of the RHEAs, possibly including twinning and other strengthening mechanisms. $HfTa_{0.5}TiZr$ is the only TRIP alloy present in the 7 compositions tested. Even though the other 6 are not TRIP alloys, microstructural characterizations are necessary on the deformation mechanisms.

Table 16: Compression Elastic Modulus Values

E_{hkl}							
Calculated	**hkl**	**HfNbTiZr**	**HfNbTaTiZr**	**$HfNb_{0.5}Ta_{0.5}TiZr$**	**$HfNbTa_{0.5}TiZr$**	**$Hf_{0.5}NbTa_{0.5}TiZr$**	**$NbTa_{0.5}TiZr$**
	110	88.68	103.39	87.85	96.31	92.37	101.79
	200	54.50	64.93	50.69	60.75	60.36	69.67
	211	88.68	103.39	87.85	96.31	92.37	101.79
	220	88.68	103.39	87.85	96.31	92.37	101.79
	310	63.28	74.97	59.80	70.07	68.96	78.60
Measured	**hkl**	**HfNbTiZr**	**HfNbTaTiZr**	**$HfNb_{0.5}Ta_{0.5}TiZr$**	**$HfNbTa_{0.5}TiZr$**	**$Hf_{0.5}NbTa_{0.5}TiZr$**	**$NbTa_{0.5}TiZr$**
	110	91.14	104.15	89.74	97.33	93.06	100.80
	200	69.49	82.47	67.59	76.55	74.72	83.92
	211	89.65	103.67	89.84	96.67	92.26	100.32
	220	90.37	104.45	90.46	96.41	91.50	102.51
	310	75.89	89.18	74.94	83.32	80.26	89.22

Table 17: Tension Elastic Modulus Values

E_{hkl}				
Calculated	**hkl**	**$HfNb_{0.5}Ta_{0.5}TiZr$**	**$HfNbTa_{0.5}TiZr$**	**$Hf_{0.5}NbTa_{0.5}TiZr$**
	110	83.11	96.71	91.16
	200	44.26	58.57	56.91
	211	83.11	96.71	91.16
	220	83.11	96.71	91.16
	310	53.22	68.26	65.81
Measured	**hkl**	**$HfNb_{0.5}Ta_{0.5}TiZr$**	**$HfNbTa_{0.5}TiZr$**	**$Hf_{0.5}NbTa_{0.5}TiZr$**
	110	88.14	97.37	92.92
	200	61.53	75.44	72.62
	211	87.71	97.62	90.91
	220	89.45	99.50	96.76
	310	69.08	83.39	78.23

Table 18: Calculated Single Crystal Elastic Constants

	Calculated							
	C11	C12	C44	S11	S12	S44	Kroner Bulk Modulus	Cauchy pressure (C11-C44)
	GPa			10^{-2} GPa^{-1}			GPa	
	Tension							
$HfNbTa_{0.5}TiZr$	171.661	130.773	45.495	0.171	-0.074	0.220	92.963	126.167
$HfNb_{0.5}Ta_{0.5}TiZr$	151.460	120.802	43.494	0.226	-0.100	0.230	81.545	107.966
$Hf_{0.5}NbTa_{0.5}TiZr$	168.757	129.054	41.731	0.176	-0.076	0.240	87.429	127.025
	Compression							
$NbTa_{0.5}TiZr$	148.784	99.000	45.332	0.144	-0.057	0.221	97.414	103.452
HfNbTaTiZr	179.403	133.915	47.506	0.154	-0.066	0.211	99.128	131.897
$Hf_{0.5}NbTa_{0.5}TiZr$	131.156	88.096	42.579	0.166	-0.067	0.235	88.427	88.578
$HfNb_{0.5}Ta_{0.5}TiZr$	177.383	142.307	42.301	0.197	-0.088	0.236	84.916	135.081
$HfNbTa_{0.5}TiZr$	148.030	105.100	44.878	0.165	-0.068	0.223	92.320	103.152
HfNbTiZr	146.773	108.533	41.653	0.184	-0.078	0.240	85.149	105.120

Table 19: Strength, Ductility, and Plasticity Values

	Measured		
	Yield Strength	**Ultimate Tensile Strength**	**Plasticity/ Ductility**
	MPa	**MPa**	**%**
	Tension		
$HfNbTa_{0.5}TiZr$	874	957	13.89
$HfNb_{0.5}Ta_{0.5}TiZr$	744	871	13.68
$Hf_{0.5}NbTa_{0.5}TiZr$	693	732	6.87
	Compression		
$NbTa_{0.5}TiZr$	986	1264	>35
HfNbTaTiZr	971	1255	>35
$Hf_{0.5}NbTa_{0.5}TiZr$	965	1233	>35
$HfNb_{0.5}Ta_{0.5}TiZr$	934	1397	>35
HfNbTa0.5TiZr	912	1286	>35
HfNbTiZr	830	1125	>35

Future Directions

- To confirm the experimental composition of the samples, a field emission SEM should be used.
- Deformation mechanisms for the single-phase RHEAs and TRIP RHEA will be discovered using TEM.
- Twinning and other strengthening mechanisms are likely to be seen in TEM results similar to those published by Huang et al. [30]
- A comprehensive report on the findings of the *in-situ* neutron diffraction will be published alongside microstructural characterization once completed.

CHAPTER SIX

RHEA Nanoparticles

Disclosure

The following chapter was written by John Whitlow on the joint collaboration with Dr. Hu Anming and David Fieser of the Mechanical Engineering Department at UTK. The provided XRD and SEM images in this section were obtained by David Fieser. The following information will be used for a later publication on HEA nanoparticles.

Introduction

The topic of HEA nanoparticles is a research area providing novel investigations on the creating of nanoparticles that can be tuned for various applications. One of the more common being the use of nanoparticles as a catalyst in the Carbon Monoxide and Carbon Dioxide Reduction Reaction (CORR and CO_2RR). This research is at the forefront of many large industries to limit their environmental impact, especially with many companies seeking to reach a net zero emission policy in the coming decade [38, 39].

The fabrication of HEA nanoparticles creates a similar set of problems seen with the design of bulk HEAs. In many instances of bulk HEAs, a single-phase is preferred, and this is the same for nanoparticles [40]. Therefore, it is best to start the fabrication with a single-phase HEA bulk for the creation of nanoparticles. The nanoparticles are then more likely to be uniform and also single-phase. Common fabrication methods include mechanical alloying, microwave heating, carbothermal shock, wet chemistry, and laser ablation synthesis in liquid which is used for the nanoparticles discussed in this chapter.

Laser ablation uses a pulsed laser to hit the bulk HEA, removing part of the surface of the bulk material, creating nanoparticles. These nanoparticles then suspend in the liquid, which can be various different liquids, most commonly being water and organic solvents such as toluene or n-hexane [41].

From the same set of compositions listed in Chapter Seven, three of the compositions that were shown to be a stable single-phase from the XRD patterns were cast and provided for laser ablation to create nanoparticles of the RHEAs. The goal of the research was to obtain single-phase nanoparticles from a single-phase RHEA.

RHEA Nanoparticle Results

$HfNb_{0.5}Ta_{0.5}TiZr$

Figure 77 presents the comparison of the obtained XRD patterns for the $HfNb_{0.5}Ta_{0.5}TiZr$ bulk alloy and fabricated nanoparticles. The as-cast material is shown again to be a single-phase BCC structure, while the nanoparticles are shown to be a single-phase FCC structure. Figure 78 shows the matching of the XRD obtained for the single-phase FCC $HfNb_{0.5}Ta_{0.5}TiZr$ nanoparticles to a known single-phase FCC ZrO_2.

$HfNbTa_{0.5}TiZr$

Figure 79 shows the comparison of the obtained XRD patterns for the $HfNbTa_{0.5}TiZr$ bulk alloy and fabricated nanoparticles. The as-cast material is shown again to be a single-phase BCC, while the nanoparticles are exhibited to be a single-phase FCC structure. Figure 80 shows the matching of the XRD obtained for the single-phase FCC $HfNbTa_{0.5}TiZr$ nanoparticles to a known single-phase FCC HfO_2.

$Hf_{0.5}NbTa_{0.5}TiZr$

Figure 81 presents the comparison of the obtained XRD patterns for the $Hf_{0.5}NbTa_{0.5}TiZr$ bulk alloy and fabricated nanoparticles. The as-cast material is shown again to be a single-phase BCC structure, while the nanoparticles are shown to be a single-phase FCC structure. Figure 82 presents the matching of the XRD obtained for the single-phase FCC $Hf_{0.5}NbTa_{0.5}TiZr$ nanoparticles to a known single-phase FCC HfO_2. Figure 83 shows a comparison of the nanoparticles of the $Hf_{0.5}NbTa_{0.5}TiZr$ alloy created in water and toluene. The difference in peak positions is due to a change in lattice parameters for the FCC structure.

The $Hf_{0.5}NbTa_{0.5}TiZr$ nanoparticles fabricated in water and toluene are shown the SEM images Figure 84 and Figure 85, respectively. These are very early preliminary images, with the quality of the image of nanoparticle fabricated in water much more clear. Still, a fairly uniform nanoparticle is seen in both figures.

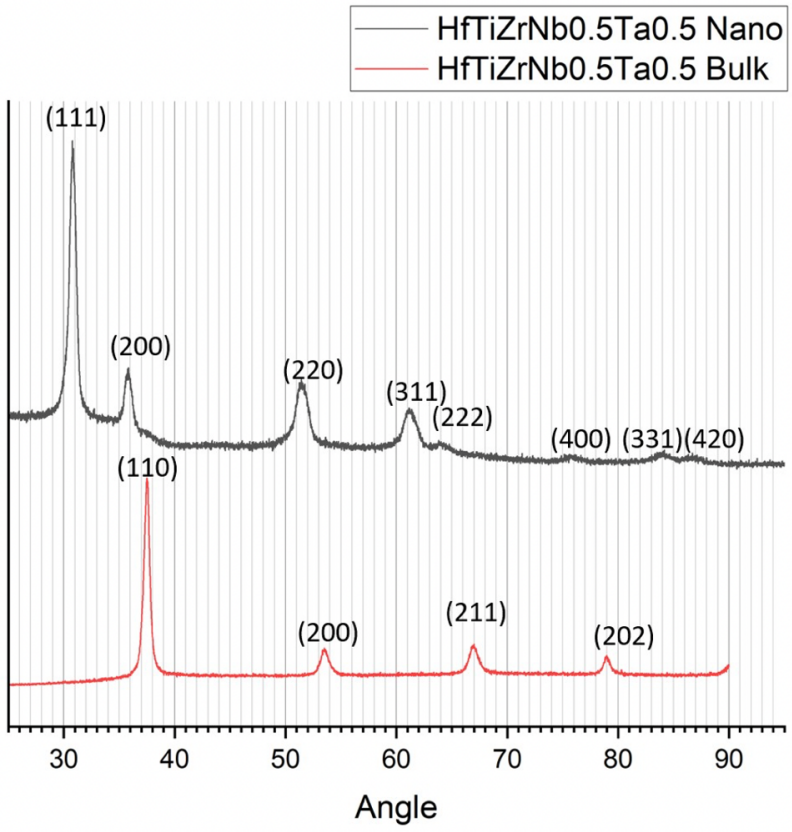


Figure 77: Nanoparticle $HfNb_{0.5}Ta_{0.5}TiZr$ XRD

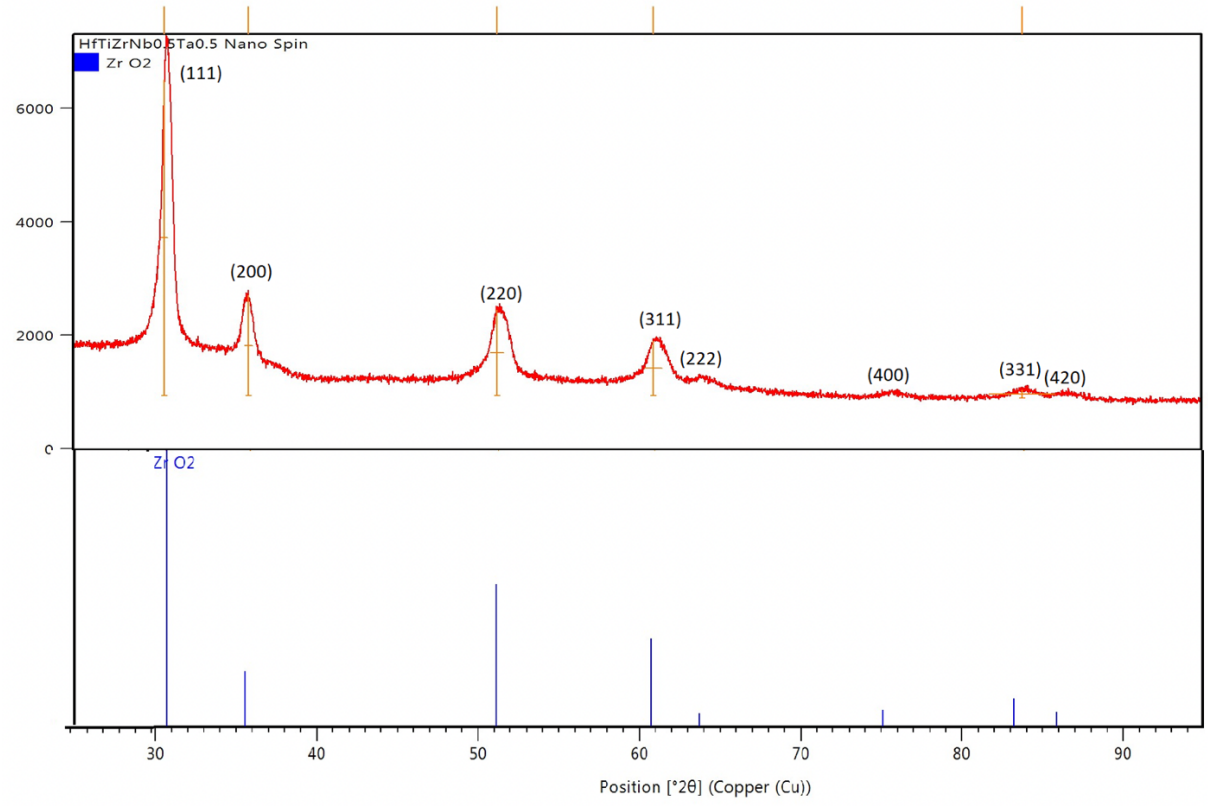


Figure 78: $HfNb_{0.5}Ta_{0.5}TiZr$ Phase Confirmation

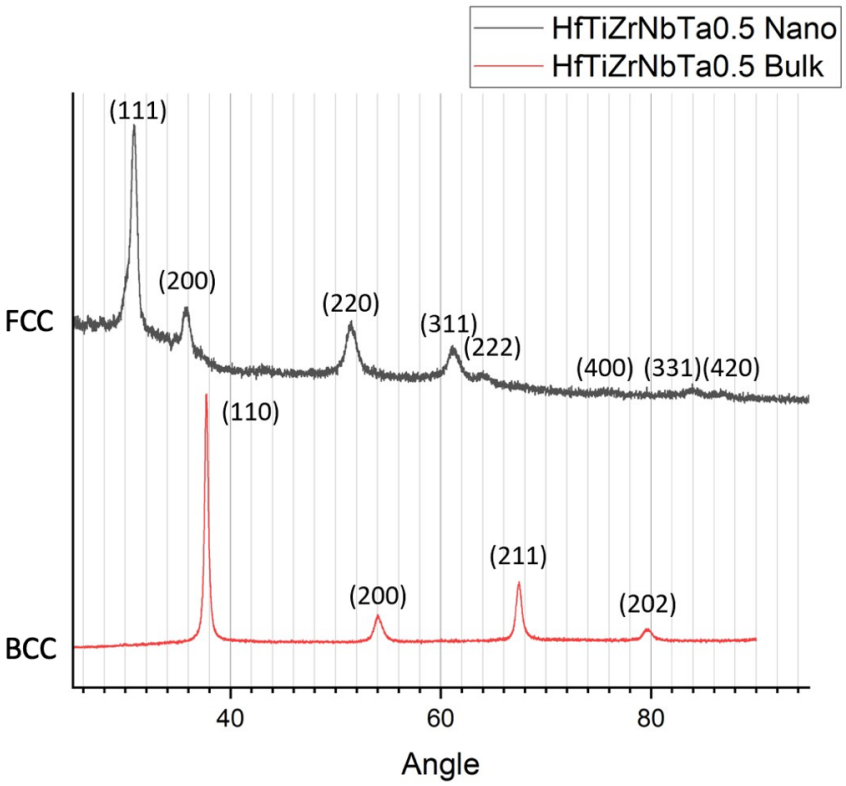


Figure 79: Nanoparticle $HfNbTa_{0.5}TiZr$ XRD

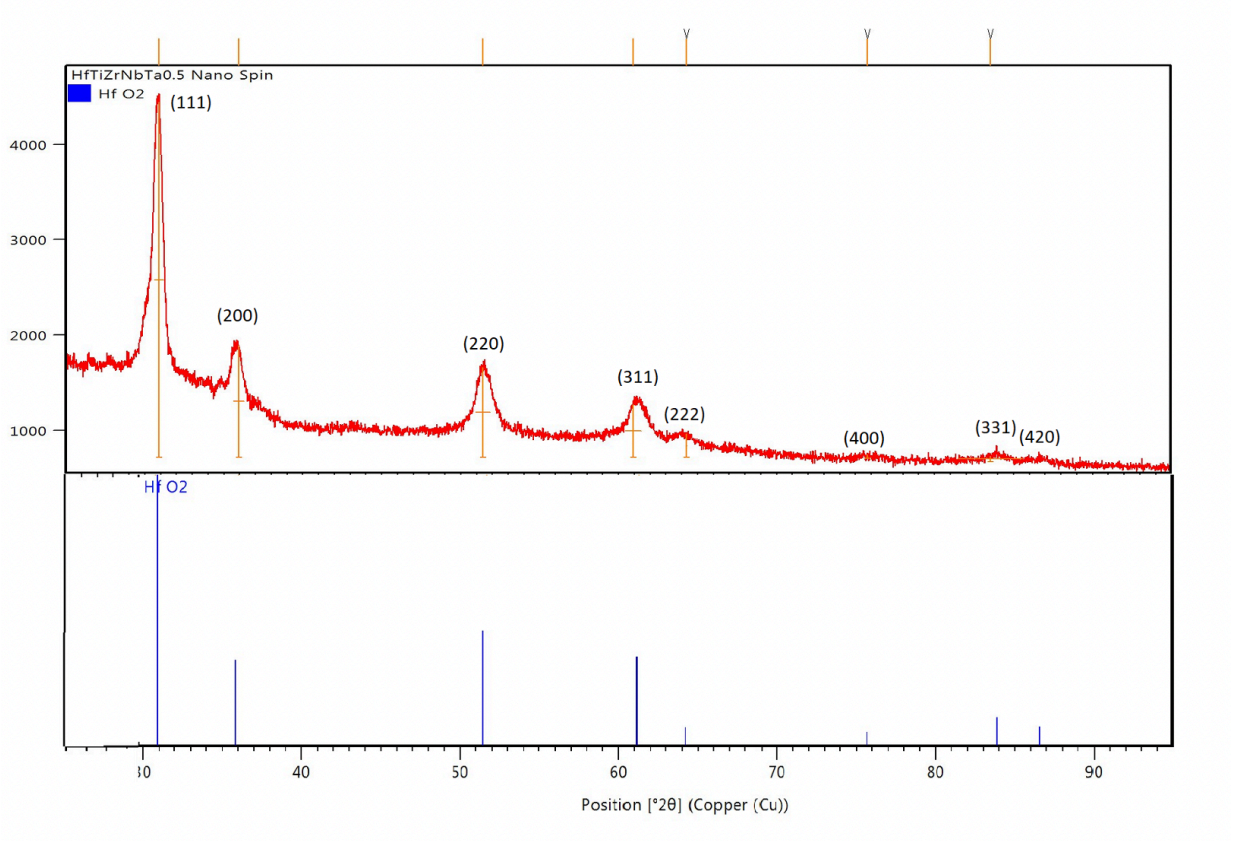


Figure 80: $HfNbTa_{0.5}TiZr$ Phase Confirmation

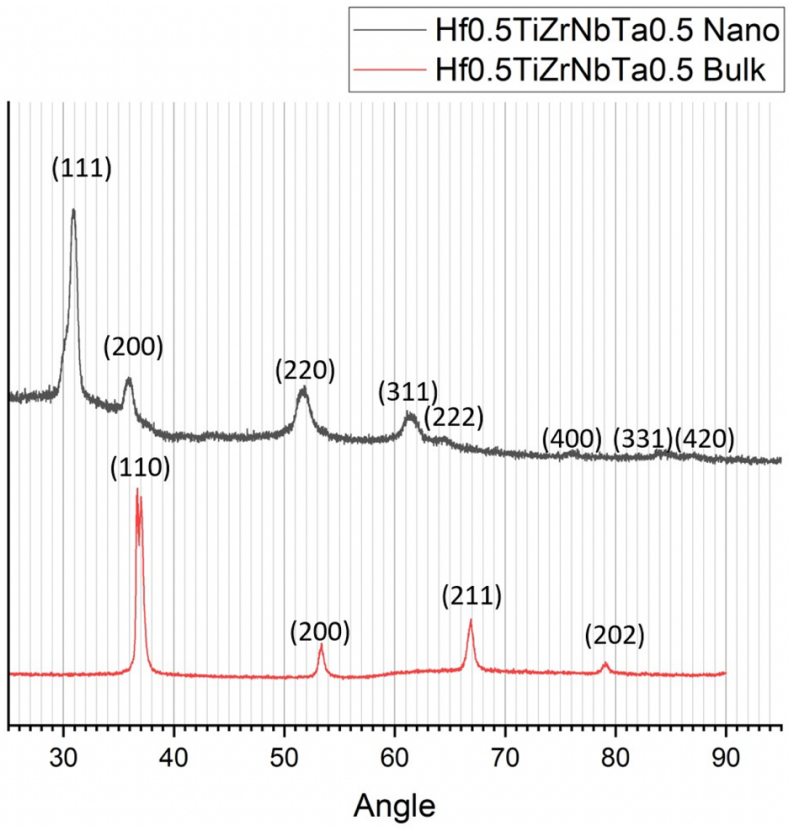


Figure 81: Nanoparticle $Hf_{0.5}NbTa_{0.5}TiZr$ XRD

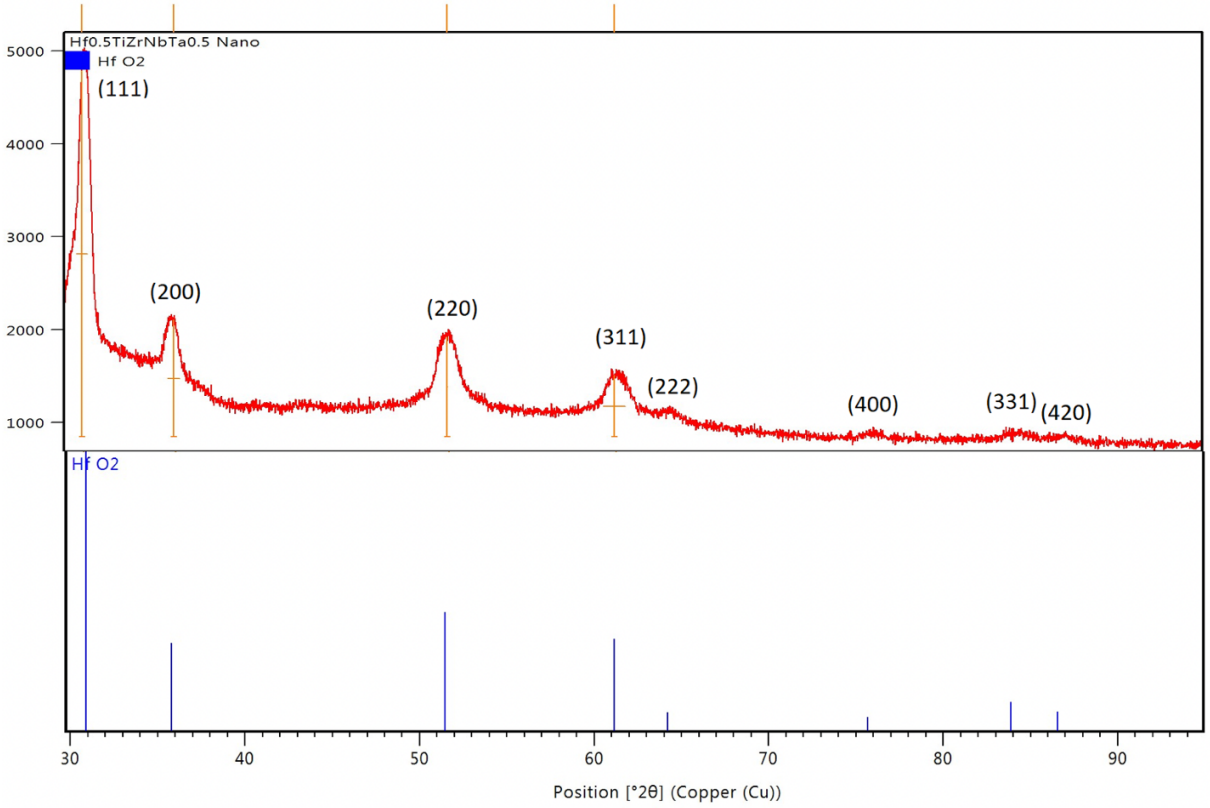


Figure 82: $Hf_{0.5}NbTa_{0.5}TiZr$ Phase Confirmation

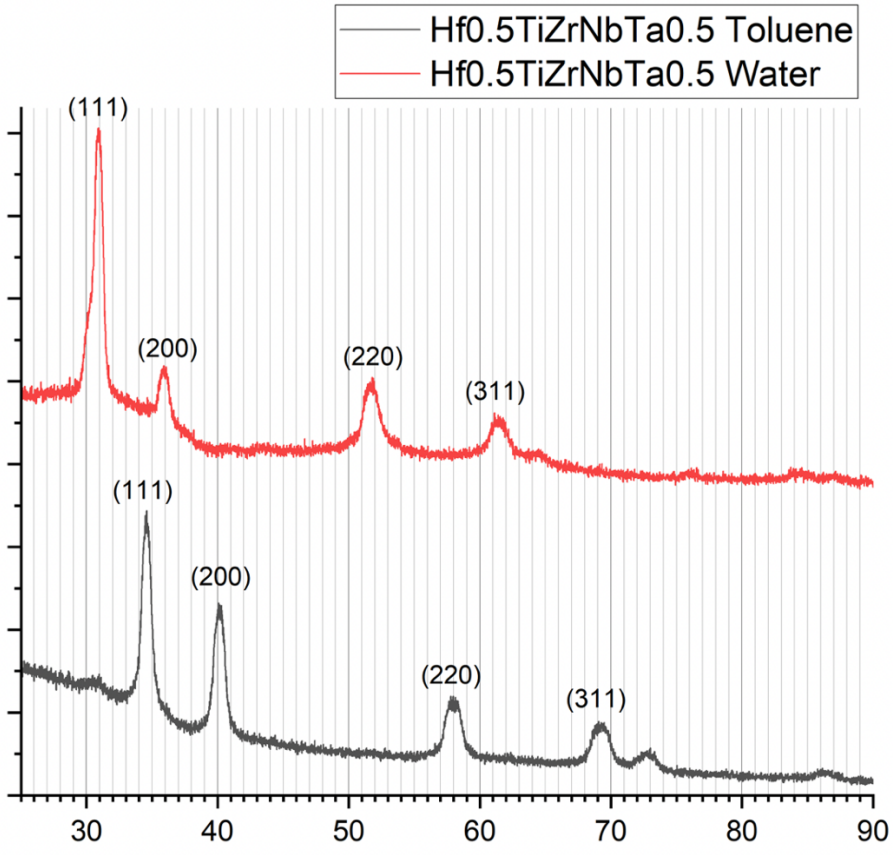


Figure 83: $Hf_{0.5}NbTa_{0.5}TiZr$ Nanoparticles Comparison

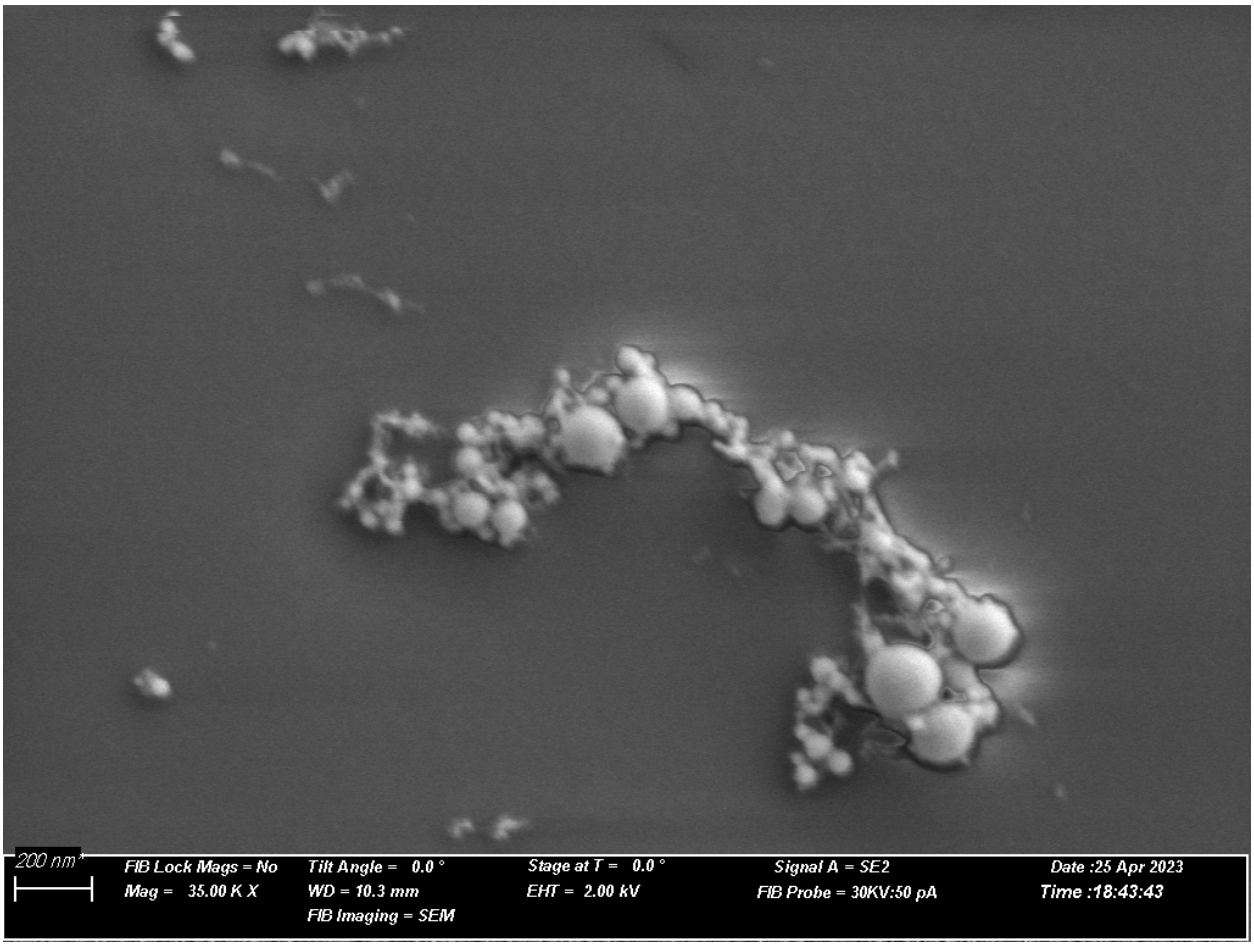


Figure 84: $Hf_{0.5}NbTa_{0.5}TiZr$ Nanoparticle Fabricated in Water

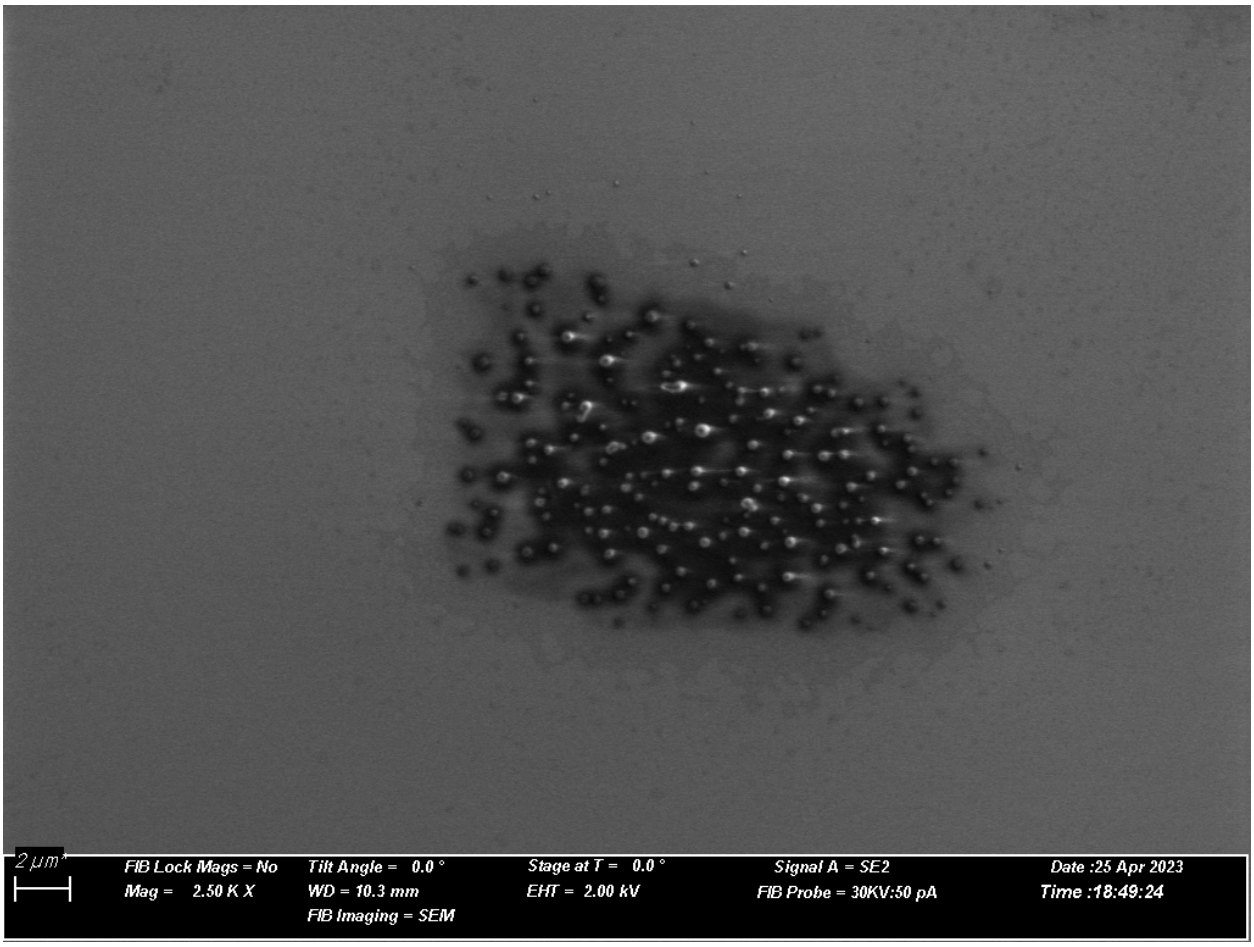


Figure 85: $Hf_{0.5}NbTa_{0.5}TiZr$ Nanoparticle Fabricated in Toluene

Discussion

The creation of RHEA nanoparticles is a new research topic within material science, and the novel research of single-phase nanoparticles with RHEAs could have many applications. The results shown are of 4 perspective single-phase RHEAs that when used to fabricate nanoparticles using laser ablation, shift from a BCC phase in bulk to an FCC phase in nanoparticles. The FCC phase is shown in comparison to known oxides, and because the nanoparticles were created in water, nanoparticles of the $Hf_{0.5}NbTa_{0.5}TiZr$ alloy were also created in the organic solvent toluene. The FCC structure is still seen, but there is the possibility of forming an oxide phase as has been reported in the creation of nanoparticles from the equimolar HfNbTaTiZr alloy [41]. The slight shift in peaks between the nanoparticles is theorized to be caused by a change in lattice parameters. Both the creation of single-phase nanoparticles and the lattice parameter change from different media provide a novel area of research.

Conclusion

In the hopes of finding a novel, single-phase RHEA nanoparticle, a transition from a bulk sample of a single-phase BCC is shown to transition into single-phase FCC nanoparticles when laser ablated in both water and toluene. There are two key areas that require further investigation: Firstly, the transition from a bulk BCC phase to a nanoparticle FCC phase. Secondly, the possible use of HEA nanoparticle catalysts in the CO and CO_2 reduction reaction. It is hypothesized that the transition of a BCC-structured bulk RHEA to FCC-structured nanoparticles is due to the original design of the bulk RHEAs. The compositions were designed to have a high likelihood of TRIP into the HCP phase at room-temperature deformation. With the stable free energy of the FCC phase very close to the HCP phase, it is possible that this is the reason behind the FCC phase being found in the nanoparticles.

CHAPTER SEVEN

Conclusions and Future Directions

Conclusions

RHEA Dataset

- Different correlations were established using a large dataset of RHEAs, providing directions for future studies on the design of RHEAs.
- Groupings can be seen that are similar to the image shown in Figure 86 (taken from E.P. George [42]), comparing common materials.
- There is a slight upward trend seen between the D-parameter and Atomic-Size Mismatch.
- VEC continues to be an accurate way to pre-determine the structure of the alloy.
- Overall, Machine Learning (ML) will continue to be a strong addition to the design of RHEAs with strength and ductility.

RHEA Fabrication, Mechanical Testing, and XRD Results

- The difficulty in the fabrication and casting of refractory-element-containing alloys continues to be a limitation in their application.
- Although the studied compositions have shown promising room-temperature characteristics, the fabrication and sample preparation are far more time consuming and arduous when compared to other more commonly used "super" alloys.
- With the success rates of compression sample casting much higher than tension samples, compression testing continues to be the easiest form of mechanical testing for RHEAs.
- From the XRD patterns of pre- and post-compression samples, $HfTa_{0.5}TiZr$ is likely to be a TRIP alloy.
- The $NbTa_{0.5}TiZr$ was hypothesized to have some form of phase transformation present during the compression testing. The post-compression sample XRD possibly had a presence of new phases but was disproven by neutron diffraction.

RHEA Neutron Diffraction Results

- *In-situ* mechanical testing was performed at the VULCAN beamline of the SNS at ORNL with compression tests conducted on all seven RHEA compositions, and tension tests performed on four out of the seven compositions.
- $HfTa_{0.5}TiZr$ was discovered to be the only TRIP alloy in the set of 7 alloys.

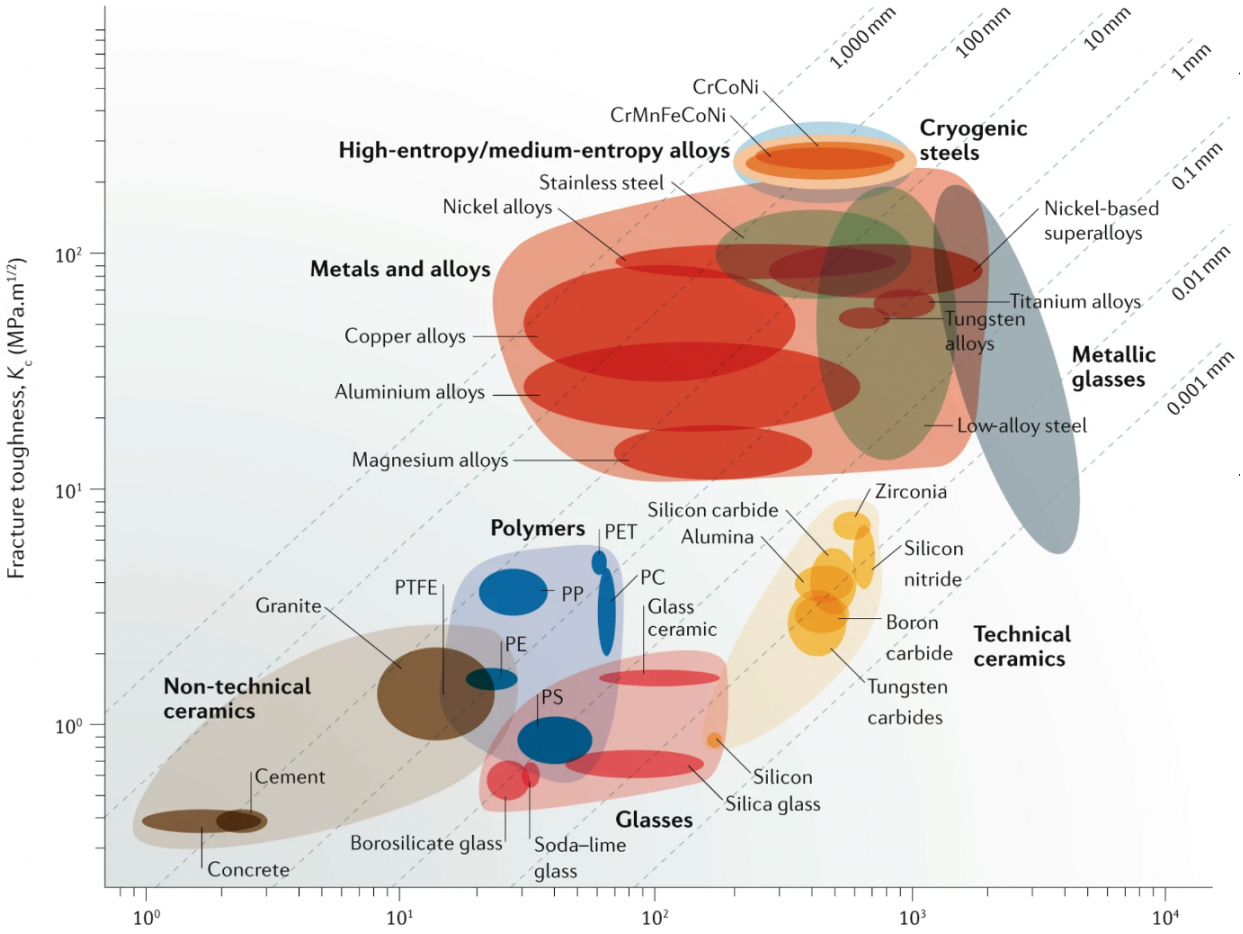


Figure 86: Common Material Comparison

Figure taken from E.P. George [42].

- HfNbTiZr, HfNbTaTiZr, $HfNb_{0.5}Ta_{0.5}TiZr$, $HfNbTa_{0.5}TiZr$, $Hf_{0.5}NbTa_{0.5}TiZr$, and $NbTa_{0.5}TiZr$ were confirmed as single-phase BCC structures.
- TEM and other microstructural characterization techniques will be used to strengthen the findings of the *in-situ* neutron diffraction.

RHEA Nanoparticles

- With the original intent of supplying single-phase HEAs for the fabrication of nanoparticles using femto-laser ablation, a successful single-phase nanoparticle was created.
- The nanoparticles created from the single-phase BCC alloys $HfNb_{0.5}Ta_{0.5}TiZr$, $HfNbTa_{0.5}TiZr$, and $Hf_{0.5}NbTa_{0.5}TiZr$ were all shown to be single-phase FCC structures.

Future Directions

RHEA Dataset

With the continued investment into various ML techniques, continuing to grow the dataset for these techniques will be beneficial for saving time and materials for researching RHEAs. Investing time into programs that predict D-Parameter for any alloy composition will provide an accurate way of designing ductile RHEAs. Combining D-Parameter with The Gibbs Free Energies of phase transformations and metastable phases will produce accurate designs for TRIP or ductile RHEAs. Fine-tuning of the addition of non-refractory elements will most likely provide a "sweet spot" of high-temperature strength and ductility.

RHEA Fabrication and Mechanical Testing

To improve the success rate on fabrication, comprehensive data should be obtained for the environment of casting to create a pool of data that can guide future fabrications. This should include Argon pressure in the tank, weight of the sample, amperage of the arc-melter, amount of time while mixing the sample, temperature of the lab, and humidity of the lab. After completing a thorough analysis of fabrication parameters, mechanical testing, specifically tension tests, should be completed. Although very difficult, tension tests provide strong results for studying the RHEAs ductility and is a priority for fabrication and mechanical testing. Microstructural characterization, such as SEM, TEM, EBSD, and XRD will strengthen the data obtained for stronger publications on the RHEAs. The data obtained from ORNL will be analyzed to confirm or deny TRIP in the

RHEAs, along with the possibility of twinning or other deformation mechanisms. High-temperature mechanical testing will strengthen the results obtained for possible applications for RHEAs and should be used to strengthen the report on the RHEA alloys tested.

RHEA Nanoparticles

The area of fabricating nanoparticles from RHEAs is a novel research area providing new studies, such as the production of single-phase FCC nanoparticles from single-phase BCC alloys. The hypothesis behind the RHEA nanoparticles being FCC can be investigated by fabricating new RHEA nanoparticles from single-phase compositions that are further from having TRIP. These alloys can be designed with a high positive value of the Gibbs Free Energy for the BCC to HCP phase transformation. Once the single-phase presence has been studied, the fabricated nanoparticles can be studied for uses in various catalytic reaction, specifically the CO and CO_2 reduction reaction [38, 39].

REFERENCES

1. Liu, L., Y. Zhang, J. Han, X. Wang, W. Jiang, C.-T. Liu, Z. Zhang, and P.K. Liaw, *Nanoprecipitate-Strengthened High-Entropy Alloys.* Advanced Science, 2021. **8**(23): p. 2100870.
2. Cantor, B., I.T.H. Chang, P. Knight, and A.J.B. Vincent, *Microstructural development in equiatomic multicomponent alloys.* Materials Science and Engineering: A, 2004. **375-377**: p. 213-218.
3. Huang, P.-K., J.-W. Yeh, T.-T. Shun, and S.-K. Chen, *Multi-Principal-Element Alloys with Improved Oxidation and Wear Resistance for Thermal Spray Coating.* Advanced Engineering Materials, 2004. **6**(1-2): p. 74-78.
4. Jien-Wei, Y., *Recent progress in high entropy alloys.* Ann. Chim. Sci. Mat, 2006. **31**(6): p. 633-648.
5. Nutor, R.K., Q. Cao, X. Wang, D. Zhang, Y. Fang, Y. Zhang, and J.-Z. Jiang, *Phase Selection, Lattice Distortions, and Mechanical Properties in High-Entropy Alloys.* Advanced Engineering Materials, 2020. **22**(11): p. 2000466.
6. Liaw, P., J.-W. Yeh, and Y. Zhang, *High-entropy alloys: Fundamentals and applications*. 2016. 1-516.
7. Inoue, A., *Stabilization of metallic supercooled liquid and bulk amorphous alloys.* Acta Materialia, 2000. **48**(1): p. 279-306.
8. Chen, J., X. Zhou, W. Wang, B. Liu, Y. Lv, W. Yang, D. Xu, and Y. Liu, *A review on fundamental of high entropy alloys with promising high–temperature properties.* Journal of Alloys and Compounds, 2018. **760**: p. 15-30.
9. Hu, Y.-J., A. Sundar, S. Ogata, and L. Qi, *Screening of generalized stacking fault energies, surface energies and intrinsic ductile potency of refractory multicomponent alloys.* Acta Materialia, 2021. **210**: p. 116800.
10. Yang, S., J. Lu, F. Xing, L. Zhang, and Y. Zhong, *Revisit the VEC rule in high entropy alloys (HEAs) with high-throughput CALPHAD approach and its applications for material design-A case study with Al–Co–Cr–Fe–Ni system.* Acta Materialia, 2020. **192**: p. 11-19.

11. Guo, S., C. Ng, J. Lu, and C.T. Liu, *Effect of valence electron concentration on stability of fcc or bcc phase in high entropy alloys.* Journal of Applied Physics, 2011. **109**(10): p. 103505.
12. Guo, S. and C.T. Liu, *Phase stability in high entropy alloys: Formation of solid-solution phase or amorphous phase.* Progress in Natural Science: Materials International, 2011. **21**(6): p. 433-446.
13. Chen, S., H.S. Oh, B. Gludovatz, S.J. Kim, E.S. Park, Z. Zhang, R.O. Ritchie, and Q. Yu, *Real-time observations of TRIP-induced ultrahigh strain hardening in a dual-phase CrMnFeCoNi high-entropy alloy.* Nature Communications, 2020. **11**(1): p. 826.
14. Mak, E., B. Yin, and W.A. Curtin, *A ductility criterion for bcc high entropy alloys.* Journal of the Mechanics and Physics of Solids, 2021. **152**: p. 104389.
15. Fang, Q., Y. Chen, J. Li, C. Jiang, B. Liu, Y. Liu, and P.K. Liaw, *Probing the phase transformation and dislocation evolution in dual-phase high-entropy alloys.* International Journal of Plasticity, 2019. **114**: p. 161-173.
16. Bhardwaj, V., Q. Zhou, F. Zhang, W. Han, Y. Du, K. Hua, and H. Wang, *Effect of Al addition on the microstructure, mechanical and wear properties of TiZrNbHf refractory high entropy alloys.* Tribology International, 2021. **160**: p. 107031.
17. Song, H., F. Tian, Q.-M. Hu, L. Vitos, Y. Wang, J. Shen, and N. Chen, *Local lattice distortion in high-entropy alloys.* Physical Review Materials, 2017. **1**(2): p. 023404.
18. Wolsey, W.C., *Chemistry of the Elements (Greenwood, NN; Earshaw, A.)*. 1985, ACS Publications.
19. Senkov, O.N., J.M. Scott, S.V. Senkova, F. Meisenkothen, D.B. Miracle, and C.F. Woodward, *Microstructure and elevated temperature properties of a refractory TaNbHfZrTi alloy.* Journal of Materials Science, 2012. **47**(9): p. 4062-4074.
20. Senkov, O.N. and S.L. Semiatin, *Microstructure and properties of a refractory high-entropy alloy after cold working.* Journal of Alloys and Compounds, 2015. **649**: p. 1110-1123.
21. Fazakas, E., V. Zadorozhnyy, L. Varga, A. Inoue, D. Louzguine-Luzgin, F. Tian, and L. Vitos, *Experimental and theoretical study of Ti20Zr20Hf20Nb20X20 (X= V or Cr)*

refractory high-entropy alloys. International Journal of Refractory Metals and Hard Materials, 2014. **47**: p. 131-138.

22. Guo, W., B. Liu, Y. Liu, T. Li, A. Fu, Q. Fang, and Y. Nie, *Microstructures and mechanical properties of ductile NbTaTiV refractory high entropy alloy prepared by powder metallurgy.* Journal of Alloys and Compounds, 2019. **776**: p. 428-436.
23. Juan, C.-C., K.-K. Tseng, W.-L. Hsu, M.-H. Tsai, C.-W. Tsai, C.-M. Lin, S.-K. Chen, S.-J. Lin, and J.-W. Yeh, *Solution strengthening of ductile refractory HfMoxNbTaTiZr high-entropy alloys.* Materials Letters, 2016. **175**: p. 284-287.
24. Lee, C., G. Song, M.C. Gao, R. Feng, P. Chen, J. Brechtl, Y. Chen, K. An, W. Guo, J.D. Poplawsky, S. Li, A.T. Samaei, W. Chen, A. Hu, H. Choo, and P.K. Liaw, *Lattice distortion in a strong and ductile refractory high-entropy alloy.* Acta Materialia, 2018. **160**: p. 158-172.
25. Qiao, D.-X., H. Jiang, W.-N. Jiao, Y.-P. Lu, Z.-Q. Cao, and T.-J. Li, *A novel series of refractory high-entropy alloys Ti2ZrHf0. 5VNbx with high specific yield strength and good ductility.* Acta Metallurgica Sinica (English Letters), 2019. **32**(8): p. 925-931.
26. Tseng, K.-K., C.-C. Juan, S. Tso, H.-C. Chen, C.-W. Tsai, and J.-W. Yeh, *Effects of Mo, Nb, Ta, Ti, and Zr on mechanical properties of equiatomic Hf-Mo-Nb-Ta-Ti-Zr alloys.* Entropy, 2018. **21**(1): p. 15.
27. Yao, H., J. Qiao, M. Gao, J. Hawk, S. Ma, H. Zhou, and Y. Zhang, *NbTaV-(Ti, W) refractory high-entropy alloys: experiments and modeling.* Materials Science and Engineering: A, 2016. **674**: p. 203-211.
28. Xu, L., Y. Jia, S. Wu, Y. Mu, Y. Jia, and G. Wang, *Low cycle fatigue properties of refractory high-entropy HfNbTiZr alloy.* Intermetallics, 2023. **152**: p. 107751.
29. Chen, S.Y., Y. Tong, K.K. Tseng, J.W. Yeh, J.D. Poplawsky, J.G. Wen, M.C. Gao, G. Kim, W. Chen, Y. Ren, R. Feng, W.D. Li, and P.K. Liaw, *Phase transformations of HfNbTaTiZr high-entropy alloy at intermediate temperatures.* Scripta Materialia, 2019. **158**: p. 50-56.
30. Huang, H., Y. Wu, J. He, H. Wang, X. Liu, K. An, W. Wu, and Z. Lu, *Phase-Transformation Ductilization of Brittle High-Entropy Alloys via Metastability Engineering.* Advanced Materials, 2017. **29**(30): p. 1701678.

31. Ye, Y., Q. Wang, J. Lu, C. Liu, and Y. Yang, *High-entropy alloy: challenges and prospects.* Materials Today, 2016. **19**(6): p. 349-362.
32. Huang, Y., J. Gao, S. Wang, D. Guan, Y. Xu, X. Hu, W.M. Rainforth, Q. Zhu, and I. Todd, *Influence of tantalum composition on mechanical behavior and deformation mechanisms of TiZrHfTax high entropy alloys.* Journal of Alloys and Compounds, 2022. **903**: p. 163796.
33. Lilensten, L., J.-P. Couzinié, J. Bourgon, L. Perrière, G. Dirras, F. Prima, and I. Guillot, *Design and tensile properties of a bcc Ti-rich high-entropy alloy with transformation-induced plasticity.* Materials Research Letters, 2017. **5**(2): p. 110-116.
34. Wang, S., S. Lu, M. Wu, D. Wang, G. Zhu, C. Yang, D. Shu, B. Sun, and L. Vitos, *Decreasing Zr content to improve tensile properties of non-equiatomic TiZrHfNb medium entropy alloys with transformation-induced plasticity.* Materials Science and Engineering: A, 2022. **832**: p. 142476.
35. Roters, F., P. Eisenlohr, L. Hantcherli, D.D. Tjahjanto, T.R. Bieler, and D. Raabe, *Overview of constitutive laws, kinematics, homogenization and multiscale methods in crystal plasticity finite-element modeling: Theory, experiments, applications.* Acta Materialia, 2010. **58**(4): p. 1152-1211.
36. Lee, C., F. Maresca, R. Feng, Y. Chou, T. Ungar, M. Widom, K. An, J.D. Poplawsky, Y.-C. Chou, and P.K. Liaw, *Strength can be controlled by edge dislocations in refractory high-entropy alloys.* Nature communications, 2021. **12**(1): p. 1-8.
37. Lee, C., G. Kim, Y. Chou, B.L. Musicó, M.C. Gao, K. An, G. Song, Y.-C. Chou, V. Keppens, W. Chen, and P.K. Liaw, *Temperature dependence of elastic and plastic deformation behavior of a refractory high-entropy alloy.* Science Advances, 2020. **6**(37): p. eaaz4748.
38. Batchelor, T.A.A., J.K. Pedersen, S.H. Winther, I.E. Castelli, K.W. Jacobsen, and J. Rossmeisl, *High-Entropy Alloys as a Discovery Platform for Electrocatalysis.* Joule, 2019. **3**(3): p. 834-845.
39. Pedersen, J.K., T.A.A. Batchelor, A. Bagger, and J. Rossmeisl, *High-Entropy Alloys as Catalysts for the CO2 and CO Reduction Reactions.* ACS Catalysis, 2020. **10**(3): p. 2169-2176.

40. Kumar Katiyar, N., K. Biswas, J.-W. Yeh, S. Sharma, and C. Sekhar Tiwary, *A perspective on the catalysis using the high entropy alloys.* Nano Energy, 2021. **88**: p. 106261.

41. Jahangiri, H., Y. Morova, A. Asghari Alamdari, Z. Eroğlu, A. Sennaroğlu, S. Guo, O. Metin, and A. Motallebzadeh, *Femtosecond laser-mediated preparation of HfNbTaTiZr refractory high-entropy alloy nanoparticles for photothermal therapy applications: Influence of solvent and fluence.* Intermetallics, 2023. **156**: p. 107834.

42. George, E.P., D. Raabe, and R.O. Ritchie, *High-entropy alloys.* Nature Reviews Materials, 2019. **4**(8): p. 515-534.

43. Chen, S.Y., X. Yang, K.A. Dahmen, P.K. Liaw, and Y. Zhang, *Microstructures and Crackling Noise of AlxNbTiMoV High Entropy Alloys.* Entropy, 2014. **16**(2): p. 870-884.

44. Yang, X., Y. Zhang, and P.K. Liaw, *Microstructure and Compressive Properties of NbTiVTaAlx High Entropy Alloys.* Procedia Engineering, 2012. **36**: p. 292-298.

45. Qiao, D.X., H. Jiang, X.X. Chang, Y.P. Lu, and T.J. Li, *Microstructure and Mechanical Properties of VTaTiMoAlx Refractory High Entropy Alloys.* Materials Science Forum, 2017. **898**: p. 638-642.

46. Lin, C.-M., C.-C. Juan, C.-H. Chang, C.-W. Tsai, and J.-W. Yeh, *Effect of Al addition on mechanical properties and microstructure of refractory AlxHfNbTaTiZr alloys.* Journal of Alloys and Compounds, 2015. **624**: p. 100-107.

47. Senkov, O.N., C. Woodward, and D.B. Miracle, *Microstructure and Properties of Aluminum-Containing Refractory High-Entropy Alloys.* JOM, 2014. **66**(10): p. 2030-2042.

48. Senkov, O.N., S.V. Senkova, and C. Woodward, *Effect of aluminum on the microstructure and properties of two refractory high-entropy alloys.* Acta Materialia, 2014. **68**: p. 214-228.

49. Stepanov, N.D., N.Y. Yurchenko, E.S. Panina, M.A. Tikhonovsky, and S.V. Zherebtsov, *Precipitation-strengthened refractory Al0.5CrNbTi2V0.5 high entropy alloy.* Materials Letters, 2017. **188**: p. 162-164.

50. Stepanov, N., N. Yurchenko, D.V. Skibin, M. Tikhonovsky, and G. Salishchev, *Structure and mechanical properties of the AlCrxNbTiV (x = 0, 0.5, 1, 1.5) high entropy alloys.* Journal of Alloys and Compounds, 2015. **652**: p. 266-280.

51. Chen, H., A. Kauffmann, B. Gorr, D. Schliephake, C. Seemüller, J.N. Wagner, H.J. Christ, and M. Heilmaier, *Microstructure and mechanical properties at elevated temperatures of a new Al-containing refractory high-entropy alloy Nb-Mo-Cr-Ti-Al.* Journal of Alloys and Compounds, 2016. **661**: p. 206-215.

52. Senkov, O.N., D. Isheim, D.N. Seidman, and A.L. Pilchak, *Development of a Refractory High Entropy Superalloy.* Entropy, 2016. **18**(3): p. 102.

53. Chen, H., A. Kauffmann, S. Laube, I.C. Choi, R. Schwaiger, Y. Huang, K. Lichtenberg, F. Müller, B. Gorr, H.J. Christ, and M. Heilmaier, *Contribution of Lattice Distortion to Solid Solution Strengthening in a Series of Refractory High Entropy Alloys.* Metallurgical and Materials Transactions A, 2018. **49**(3): p. 772-781.

54. Coury, F.G., M. Kaufman, and A.J. Clarke, *Solid-solution strengthening in refractory high entropy alloys.* Acta Materialia, 2019. **175**: p. 66-81.

55. Yurchenko, N., N. Stepanov, S. Zherebtsov, M.A. Tikhonovsky, and G. Salishchev, *Structure and mechanical properties of B2 ordered refractory AlNbTiVZrx (x = 0–1.5) high-entropy alloys.* Materials Science and Engineering A-structural Materials Properties Microstructure and Processing, 2017. **704**: p. 82-90.

56. Guo, N.N., L. Wang, L.S. Luo, X.Z. Li, R.R. Chen, Y.Q. Su, J.J. Guo, and H.Z. Fu, *Microstructure and mechanical properties of in-situ MC-carbide particulates-reinforced refractory high-entropy Mo0.5NbHf0.5ZrTi matrix alloy composite.* Intermetallics, 2016. **69**: p. 74-77.

57. Zhang, M., X. Zhou, and J. Li, *Microstructure and Mechanical Properties of a Refractory CoCrMoNbTi High-Entropy Alloy.* Journal of Materials Engineering and Performance, 2017. **26**(8): p. 3657-3665.

58. Fazakas, É., V. Zadorozhnyy, L.K. Varga, A. Inoue, D.V. Louzguine-Luzgin, F. Tian, and L. Vitos, *Experimental and theoretical study of Ti20Zr20Hf20Nb20X20 (X=V or Cr) refractory high-entropy alloys.* International Journal of Refractory Metals and Hard Materials, 2014. **47**: p. 131-138.

59. Senkov, O.N. and C.F. Woodward, *Microstructure and properties of a refractory NbCrMo0.5Ta0.5TiZr alloy.* Materials Science and Engineering: A, 2011. **529**: p. 311-320.

60. Senkov, O.N., S.V. Senkova, D.B. Miracle, and C. Woodward, *Mechanical properties of low-density, refractory multi-principal element alloys of the Cr–Nb–Ti–V–Zr system.* Materials Science and Engineering: A, 2013. **565**: p. 51-62.

61. Waseem, O.A., J. Lee, H.M. Lee, and H.J. Ryu, *The effect of Ti on the sintering and mechanical properties of refractory high-entropy alloy TixWTaVCr fabricated via spark plasma sintering for fusion plasma-facing materials.* Materials Chemistry and Physics, 2018. **210**: p. 87-94.

62. Guo, N.N., L. Wang, L.S. Luo, X.Z. Li, R.R. Chen, Y.Q. Su, J.J. Guo, and H.Z. Fu, *Microstructure and mechanical properties of refractory high entropy (Mo0.5NbHf0.5ZrTi)BCC/M5Si3 in-situ compound.* Journal of Alloys and Compounds, 2016. **660**: p. 197-203.

63. Wang, M., Z. Ma, Z. Xu, and X. Cheng, *Microstructures and mechanical properties of HfNbTaTiZrW and HfNbTaTiZrMoW refractory high-entropy alloys.* Journal of Alloys and Compounds, 2019. **803**: p. 778-785.

64. Juan, C.-C., M.-H. Tsai, C.-W. Tsai, C.-M. Lin, W.-R. Wang, C.-C. Yang, S.-K. Chen, S.-J. Lin, and J.-W. Yeh, *Enhanced mechanical properties of HfMoTaTiZr and HfMoNbTaTiZr refractory high-entropy alloys.* Intermetallics, 2015. **62**: p. 76-83.

65. Guo, N.N., L. Wang, L.S. Luo, X.Z. Li, Y.Q. Su, J.J. Guo, and H.Z. Fu, *Microstructure and mechanical properties of refractory MoNbHfZrTi high-entropy alloy.* Materials & Design, 2015. **81**: p. 87-94.

66. Nie, X.W., M.D. Cai, and S. Cai, *Microstructure and mechanical properties of a novel refractory high entropy alloy HfMoScTaZr.* International Journal of Refractory Metals and Hard Materials, 2021. **98**: p. 105568.

67. Zhang, Y., Y. Liu, Y. Li, X. Chen, and H. Zhang, *Microstructure and mechanical properties of a refractory HfNbTiVSi0.5 high-entropy alloy composite.* Materials Letters, 2016. **174**: p. 82-85.

68. Zhang, Y., Y. Liu, Y.X. Li, X. Chen, and H.W. Zhang, *Microstructure and Mechanical Properties of a New Refractory HfNbSi0.5TiVZr High Entropy Alloy.* Materials Science Forum, 2016. **849**: p. 76-84.

69. Wu, Y.D., Y.H. Cai, X.H. Chen, T. Wang, J.J. Si, L. Wang, Y.D. Wang, and X.D. Hui, *Phase composition and solid solution strengthening effect in TiZrNbMoV high-entropy alloys.* Materials & Design, 2015. **83**: p. 651-660.

70. Han, Z.D., H.W. Luan, X. Liu, N. Chen, X.Y. Li, Y. Shao, and K.F. Yao, *Microstructures and mechanical properties of TixNbMoTaW refractory high-entropy alloys.* Materials Science and Engineering: A, 2018. **712**: p. 380-385.

71. Han, Z.D., N. Chen, S.F. Zhao, L.W. Fan, G.N. Yang, Y. Shao, and K.F. Yao, *Effect of Ti additions on mechanical properties of NbMoTaW and VNbMoTaW refractory high entropy alloys.* Intermetallics, 2017. **84**: p. 153-157.

72. Wang, S.-P. and J. Xu, *TiZrNbTaMo high-entropy alloy designed for orthopedic implants: As-cast microstructure and mechanical properties.* Materials Science and Engineering: C, 2017. **73**: p. 80-89.

73. Li, T., W. Jiao, J. Miao, Y. Lu, E. Guo, T. Wang, T. Li, and P.K. Liaw, *A novel ZrNbMoTaW refractory high-entropy alloy with in-situ forming heterogeneous structure.* Materials Science and Engineering: A, 2021. **827**: p. 142061.

74. Lee, C., Y. Chou, G. Kim, M.C. Gao, K. An, J. Brechtl, C. Zhang, W. Chen, J.D. Poplawsky, G. Song, Y. Ren, Y.-C. Chou, and P.K. Liaw, *Lattice-Distortion-Enhanced Yield Strength in a Refractory High-Entropy Alloy.* Advanced Materials, 2020. **32**(49): p. 2004029.

75. Hou, P., S. Mooraj, V.K. Champagne, M.J. Siopis, P.K. Liaw, S. Gerasimidis, and W. Chen, *Effect of Build Height on Temperature Evolution and Thermally Induced Residual Stresses in Plasma Arc Additively Manufactured Stainless Steel.* Metallurgical and Materials Transactions A, 2022. **53**(2): p. 627-639.

VITA

John H. Whitlow was born in Lagrange, Georgia in 2000 to Drs. John and Donna Whitlow. He graduated from Lagrange Academy in 2018 and then attended Georgia College & State University where he graduated in May 2022 with a Bachelor of Science in Chemistry and minor in Mathematics. He began his studies in Material Science and Engineering at the Graduate School at the University of Tennessee, Knoxville in June 2022. On July 30, 2022, he married Kayleigh Ryles. He received his Master of Science in Material Science and Engineering from the Tickle College of Engineering at the University of Tennessee Knoxville in August 2023.